VARIABILITY IN THE SHAPE MEMORY AND MECHANICAL RESPONSE OF ADDITIVELY MANUFACTURED NITI

A Dissertation

by

BRIAN EELAN FRANCO

Submitted to the Office of Graduate and Professional Studies of
Texas A&M University
in partial fulfillment of the requirements for the degree of

DOCTOR OF PHILOSOPHY

Chair of Committee,	Ibrahim Karaman
Committee Members,	Alaa Elwany
	Raymundo Arroyave
	Ankit Srivastava
Head of Department,	Ibrahim Karaman

May 2019

Major Subject: Materials Science and Engineering

ABSTRACT

Variability in the Shape Memory and Mechanical Response of Additively Manufactured NiTi

(May 2019)

Brian E. Franco, B.S., Texas A&M University

M.S., Texas A&M University

Chair of Advisory Committee: Dr. Ibrahim Karaman

Despite the tremendous growth in adoption and research interest in additive manufacturing, there remain several unsolved issues regarding the properties and defects associated with the process. In selective laser melting, variability and poor repeatability has been known to be a critical defect that requires costly and time consuming postprocessing to correct. Despite this fact, there has been very little research into this topic. Variability issues are especially critical with regards to NiTi alloys, which are especially sensitive to changes in microstructure and composition.

In the current work we investigate various aspects of variability in the transformation temperatures under stress free conditions as well as the mechanical properties of NiTi alloys manufactured using selective laser melting. The main objectives were to observe and quantify variability in the transformation temperatures and mechanical properties, to investigate the relationship between process parameters and variability, and to investigate the microstructural and compositional mechanisms that control the variability.

Experimental evidence was provided that verified the presence of localized variability on the micron scale as well as poor repeatability in NiTi parts. The variability in transformation temperatures and mechanical properties was found to exceed the values found in conventionally processed alloys found in the literature. Out of the various process parameters investigated such

as laser power and speed, the hatch distance was found the be the most effective parameter for controlling the variability. Use of a narrow hatch distance of 35μm resulted in parts with highly homogenous and repeatable transformations, while larger hatch distances of 120μm resulted in parts with inhomogenous and poorly-repeatable transformations. It was also found that the critical hatch distance between variability and repeatability was between 50-60μm.

The mechanisms responsible for variability in the transformation temperatures were found to be precipitate volume fraction and interparticle distance as well as dislocation density. In parts with high variability it was observed that local differences in precipitate volume fraction, size, and area fraction occurred, as well as differences in dislocation density.

Finally, it was shown using uniaxial tensile testing that specimens that had exhibited high variability in transformation temperatures also had higher variability in elastic modulus and yield strength.

DEDICATION

This work is dedicated to my brother, Benjamin Franco. I hope you are proud of me.

ACKNOWLEDGEMENTS

There are many people that I must thank here, because without their help I would not be where I am today. First, I must thank my advisor Professor Ibrahim Karaman. Many years ago, during my time as an undergraduate, Dr. Karaman hired me to work in his lab. I am extremely grateful that he led me on this path; and I must also thank him for keeping me on it during those times when I doubted myself.

I would like to thank my committee members, Dr. Elwany, Dr. Arroyave, and Dr. Srivastiava for their guidance, advice, knowledge, and patience with me over the years.

To Professor Chumlyakov, I would like to thank you for the many conversations we had regarding the most challenging aspects of shape memory and metals research. The knowledge that you have freely shared with me has been a cornerstone of my studies.

To all of those who have helped me along the way; Hande Ozcan, Dr. Ji Ma, Dr. Can Atli, Dr. Nick Bruno, Dr. Nick Barta, Dr. Taymaz Jozaghi, Joel Sam, Robert Barber, Ben Loveall, William Trehern, Michael Elverud and a great deal more that I cannot list here. I am extremely grateful for everything you have done for me.

To the other students of the additive manufacturing student group, none of my work would have been possible without your hard work, your incredible research, and your support: Kubra Karayagiz, Luke Johnson, Mohammed Mahmoudi, Gustavo Tapia, and Bing Zhang.

I would like to also thank Tizian Arold for the hard work he did on mechanical testing experiments, and to Ben Loveall who helped me with many aspects of my research.

CONTRIBUTORS AND FUNDING SOURCES

This work was supported by a dissertation committee consisting of Professor Ibrahim Karaman (advisor) and Professor Alaa Elwany of the Department of Industrial and Systems Engineering and Professors Raymundo Arroyave and Ankit Srivastava of the Department of Materials Science.

A large portion of the mechanical testing experiments were performed by Tizian Arold, who also helped with the analysis. The atom probe tomography experiments were performed by Dr. Chad Hornbuckle from ARL. TEM experiments were done with the help of Professor Ruben Santamarta. WDS experiments were done with the help of Dr. Andrew Mott.

All other work conducted for the dissertation was completed by the student independently.

This work was made possible by the NASA Space Technology Research Grants Program, Early Stage Innovations, through grant NNX15AD71G, as well as the use of the Texas A&M Microscopy and Imaging Center equipment and facilities. The FE-SEM acquisition was supported in part by the National Science Foundation under Grant No. DBI-0116835.

NOMENCLATURE

AM	Additive Manufacturing
BSE	Backscattered Electron
DSC	Differential Scanning Calorimetry
DED	Directed Energy Deposition
EBM	Electron Beam Melting
EDM	Electrical Discharge Machining
EDS	Electron Dispersive Spectroscopy
FEA	Finite Element Analysis
FIB	Focused Ion Beam
PBF	Powder Bed Fusion
SE	Secondary Electron
SEM	Scanning Electron Microscopy
TEM	Transmission Electron Microscopy
TWSME	Two-Way Shape Memory Effect
WDS	Wavelength Dispersive Spectroscopy

TABLE OF CONTENTS

Page

LIST OF FIGURES

Page

LIST OF TABLES

Page

CHAPTER I

INTRODUCTION

1.1 Additive Manufacturing and NiTi

Additive manufacturing (AM) refers to a family of manufacturing techniques where fully net-shape parts are produced, layer-by-layer, from a feedstock. AM's origin can be traced back as far as the 1960s, when the Battelle institute attempted to consolidate solid parts from a photo-sensitive liquid polymer using lasers [1]. The earliest research focused on these stereolithography methods; however, since that time the application of AM methods has been extended to not only polymers, but metals and ceramics as well. Currently, a wide variety of techniques for consolidating metals exists not just in academic settings but in the industrial realm as well. These can be classified by the form of the feedstock; powder bed fusion (PBF), directed energy deposition (DED), binder jetting, wire fusion, and sheet fusion [2-4].

Currently, out of the current metal AM techniques, the PBF method known as selective laser melting (SLM) has shown strong potential for industrial usage, and there are several examples of successful implementation, such as the fuel nozzle for the GE leap engine [5] and the combustion chamber for the SpaceX SuperDraco engine [6]. Currently, SLM machines occupy a majority of the market share over other types, namely DED, electron beam melting (EBM), and wire fusion [7]. It has been previously shown that SLM can be used to successfully produce parts and test coupons from a wide array of commercial alloys, such as 316 stainless steel [8], M2 high speed steel [9], 17-4PH steel [10], Ni alloy 625 [11, 12], Ni alloy 718 [13, 14], and TiAl6V4 [15, 16], as well as pure Cu [17] and Cu alloys [18, 19], and aluminum alloys [20-22]. Currently, there is a fairly extensive body of work relating to NiTi manufactured by the

SLM process; these focused on optimization of process parameters for application [23-26], understanding the process parameter-shape memory effect relationship [27-33], the effect of process parameters on grain texture and anisotropy [34-37], mechanical and thermomechanical behavior [27, 29, 32, 37-40], and post-printing thermal treatments [38, 41]. However; there is a critical aspect of SLM-built NiTi that has not yet been addressed. It is known that one drawback of AM is an inherent variability in microstructure, composition, and properties [4, 5, 10, 11, 42]. This is of special concern for NiTi, due to the sensitivity of the shape memory behavior on the composition [43], precipitate volume fraction and interparticle distance [44, 45], stresses [46], dislocation density [47], grain size [48], and texture [49]. The evolution and end state of all of these characteristics are dependent on the local thermal conditions, which vary depending on machine model, material properties, powder characteristics, process parameters, atmosphere type and flow characteristics, progression of the part build, geometry, as well as stochastic factors such as powder packing, beam-plume interactions, material ejecta events, and pore formation.

It is therefore the focus of the current work to understand the variability and repeatability of the shape memory behavior and mechanical behavior of SLM-built NiTi. This represents a novel contribution to the science and engineering of additive manufacturing, since to best knowledge there has been no previous work on this topic. Additionally, understanding variability is of concern for future research in the field, since it could have an impact on experimental procedures and statistical requirements for reporting of results. Finally, addressing the variability issue in AM NiTi is a critical step for commercialization and implementation due to the strict standards and property requirements that are inherent to shape memory applications.

1.2 Motivation

Although the worldwide manufacturing market is dominated by traditional processes, it can be said that AM is growing from a niche technology, and can be expected to occupy a significant portion of the market. In the first decade alone, AM product sales and services reached $1 billion in value [50], and grew to over $5.1 billion in 2016 [51]. Since 2014, the industry has grown by over 24% annually [7], and if current trends continue, is expected to be valued at over $16 billion by 2025, and $57 billion by 2030 [52].

The growth of AM can be attributed to two categories of advantages; the first being engineering considerations that broaden the design space, and the second being economic considerations that influence profitability. Some of the engineering considerations are well known; for example, the capability to construct complex parts that would be time-consuming to build with subtractive methods, or the ability to create complex internal spaces. Two such geometries would be porous lattice scaffolds, and structures with internal passages (Figure 1).

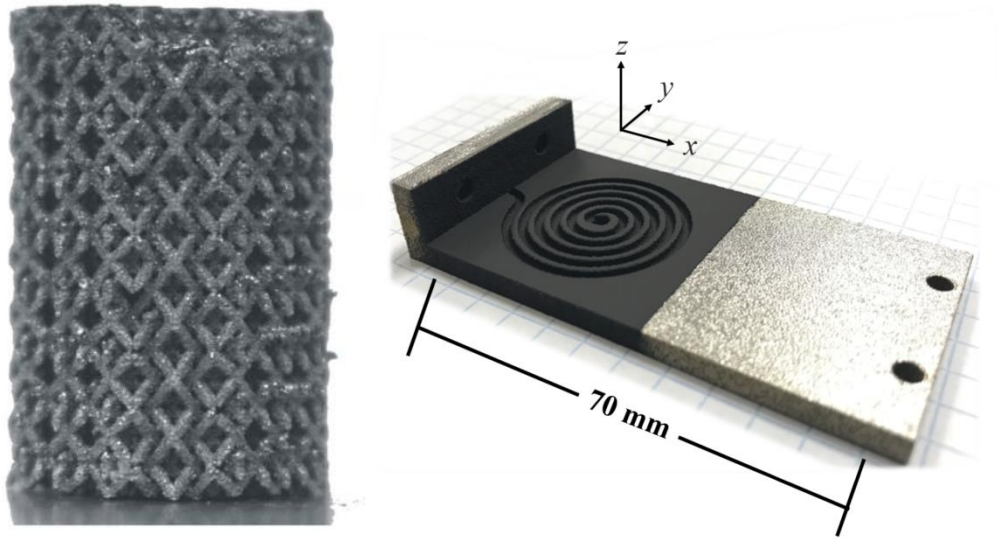

Figure 1: Left: SLM-built NiTi lattice scaffold [53], Right: SLM-built NiTi actuator with in-built fluid path for rapid cooling [54]

Both of these geometries have been explored for use with SLM-built NiTi. NiTi scaffolds have applications in the biomedical industry as orthopedic implants. NiTi has good biocompatibility, and the low effective elastic modulus of superelastic NiTi helps to prevent the stress shielding issue, which lowers bone strength over time. Additionally, the scaffold geometry allows for bone ingrowth and osseointegration [55, 56]. NiTi structures with internal passages have applications in aerospace; one issue with SMAs is the requirement of heating and cooling the device in order to trigger actuation. The actuation cycle time is then limited by heat transfer considerations. Hardtl et. al explored the use of SLM in building a NiTi actuator with fluid passages filled with a liquid metal; this resulted in a device with enhanced heat transfer and lower actuation cycle time [54].

A second engineering consideration that has seen increasing interest with the advent of AM is the idea of using the localized nature of the SLM process as well as the high degree of control over the process parameters to design additional functionality into a solid device. Two such examples are location dependent tailored properties and 4D printing. Location dependent properties are achieved by simply changing the process parameters in different regions of the same part, which alters the thermal histories and therefore the microstructure and properties. This has been demonstrated in 316L steel to produce specimens with location dependent hardness [57] and in NiTi where specimens had location dependent transformation temperatures [58, 59]. 4D printing refers to 3D printed objects that change property or shape over time (where the fourth ‘D’ is time). Such devices are intended to be highly customizable and responsive to environmental conditions, or to be easy to store and transport (by having a small volume ‘storage’ shape and a transformed full volume ‘usage’ shape) [60]. Ma et al. demonstrated a NiTi device that showed both location dependent properties and 4D printing behavior (Figure 2).

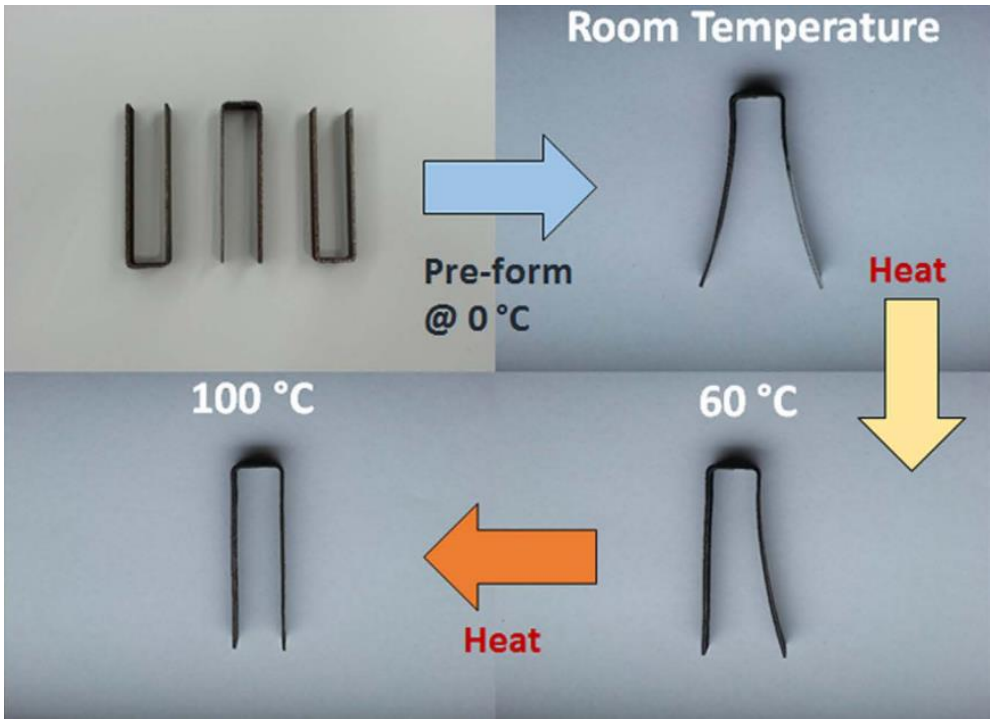

Figure 2: Location dependent 4D printed NiTi device. The two arms of the fork are printed with different process parameters. The left arm transforms at 60°C, while the right arm transforms at 100°C [59].

The device was in the shape of a tuning fork with two arms. Each arm was printed using different process parameters, which resulted in each arm transforming at a different temperature [59].

While these unique engineering advantages do increase the appeal of the process, it is ultimately economic concerns that will govern whether or not SLM will see widespread adoption. In fact, several works have indicated that under certain conditions AM processes are in fact economically preferable to conventional techniques. In one such article, it was argued that AM processes could be economically advantageous when considered from a lean manufacturing perspective [61]. Lean manufacturing is a management philosophy where costs are reduced by

producing only to the point of customer demand and by identifying and reducing waste [62]. AM's facilitation of lean manufacturing principles can be summarized by the following [61]:

- Distributed production: AM hardware is conducive to having multiple, well distributed production centers that are closer to customers, therefore reducing transportation costs and order lead times
- Production on demand: Storage of inventory comes with a considerable cost, which can be eliminated by producing parts on customer demand.
- Supply chain simplification: Traditional manufacturing often involves multiple steps in the supply chain from material distribution to customer; the AM supply chain is greatly simplified (material distribution to AM processing to customer) which reduces cost and limits exposure to supply chain disruption.

While this analysis is material agnostic, it is definitely applicable to the case of NiTi.

Another economic analysis determined the conditions where AM becomes profitable over conventional methods by considering the relative costs between conventional machining and AM, taking into account the specific costs of AM and machining, the cost of the raw material, the volume of material needed to produce a part, the volume of material removed, and the volume of the final part. Their analysis indicated that when the cost of raw material is high, the buy-to-fly ratio (ratio of initial raw material volume to final part volume) is high, the part complexity is high, and when machining is difficult or slow, AM becomes increasingly cost-effective [63]. NiTi meets several of these categories. NiTi has a high raw material cost, similar to that of engineering Ti alloys, and an order of magnitude higher than that of conventional steels or aluminum alloys. Part complexity and the buy-to-fly ratio are both subject to the specific application; however, considering the current body of work on orthopedic implants, as well as

aerospace solid-state actuators, these would likely be significant factors. Finally, it is known that machining of NiTi can be difficult in comparison to most conventional alloys, mostly due to the varying and complex material properties (caused by the shape memory transformation), low apparent elastic modulus (in superelastic alloys), high hardness, high tool adhesion, and poor machining thermal characteristics [64]. With these considerations in mind, it can be said that SLM process is a strong potential processing route for commercial production of NiTi devices.

As previously noted, the current literature has addressed many of the engineering aspects of this topic that are necessary for implementation. There is currently a substantial body of knowledge on process-property relationships, on the optimization of shape memory behavior by process control and by post-hoc heat treatments, on process control for biomedical applications, and aerospace applications. However, there is still an opportunity to address a critical and little understood aspect of this field; that is, the variability of the shape memory behavior and the mechanical response. Even though variability has been noted as a major drawback of AM there has been very little research into this topic regardless of material or specific process. In practical application for conventional materials, this issue can be avoided by standard post processing techniques such as hot isostatic pressing and post-hoc solution treatment. In the context of SLM-built NiTi, however, it is desirable to avoid post processing to reduce cost, and because it eliminates the possibility of tailored, process-controlled properties, localized properties, and 4D printing. Controlling and understanding the variability is also important when considering the application markets where NiTi is prevalent; the aerospace and biomedical fields. Both of these fields have strictly established materials certification requirements, and the tolerances for material properties are small. For point of reference, a study of variance in conventionally

produced NiTi found that the standard deviation for transformation temperatures in a single spool of wire was less than 1°C [65].

In the current work, we propose to address several open questions on the variability in SLM-built NiTi. Currently, it is unknown if these materials exhibit variations in properties in excess of those observed in conventionally processed products. This would inform future work as to sample size and statistical reporting, as well as determine if steps must be taken to reduce variability for applications. Furthermore, it is critical to understand how the variability in shape memory behavior changes with respect to the process parameters space; this data would allow for the realization of strategies to decrease the variability without post-processing. We performed a suite of microstructural characterization experiments in order to understand the process-property-microstructure relationships causing variability. Finally, we performed a mechanical testing study in order to determine if variation in shape memory behavior correlated to variation in mechanical properties.

1.3 Objectives

The objectives of the current work are summarized as follows:

- Observe and quantify the magnitude of variability in shape memory behavior of SLM-built NiTi under stress-free conditions.
- Establish the process parameter-variability relationships in order to determine which specific process parameters influence variability the most, and to help identify best-practices for building repeatable and homogenous parts.
- Perform microstructural characterization to determine which microstructural changes are responsible for causing variability.

- Perform mechanical testing experiments to observe correlation between variability in shape memory behavior and mechanical properties.

CHAPTER II

LITERATURE REVIEW

This chapter provides a review of the current literature which will be relevant for discussion of experimental results in later sections. The first section will be a brief discussion on the SLM process; the technical details of the equipment, the process parameters, the interaction between beam and the powder bed, and the defects that occur during the process. The second section will briefly review NiTi; the shape memory effect (SME), the metallurgy and phase diagram, and the relationship between microstructure and the SME. The final section will review the body of work on NiTi built using SLM.

2.1 A Review of SLM

SLM is an AM technique that is part of the subclass known as PBF. PBF is distinct from other AM techniques due to the use of a powdered feedstock that is spread thinly, layer by layer, to gradually construct parts. The other AM technique in the PBF subclass, EBM, is distinct from SLM due to the energy source used to melt the powder bed. EBM uses an electron beam, while SLM uses a laser. Figure 3 shows a diagram of the layout for a typical SLM machine. Parts are usually constructed in an enclosed chamber. To limit the amount of oxygen and moisture in the enclosure, either a system of venting atmosphere/backfilling with a shielding gas is used, or the chamber is evacuated using a pumping system and then backfilled with shielding gas. Use of argon is most common, however, nitrogen and hydrogen mixes are also used. The laser and optical system are typically contained outside of the build chamber; the beam originates from a laser module, passes through a focusing lens, is directionally controlled by a scanner (such as a

galvanometer), and then passes through a laser-transparent window in the enclosure towards the component.

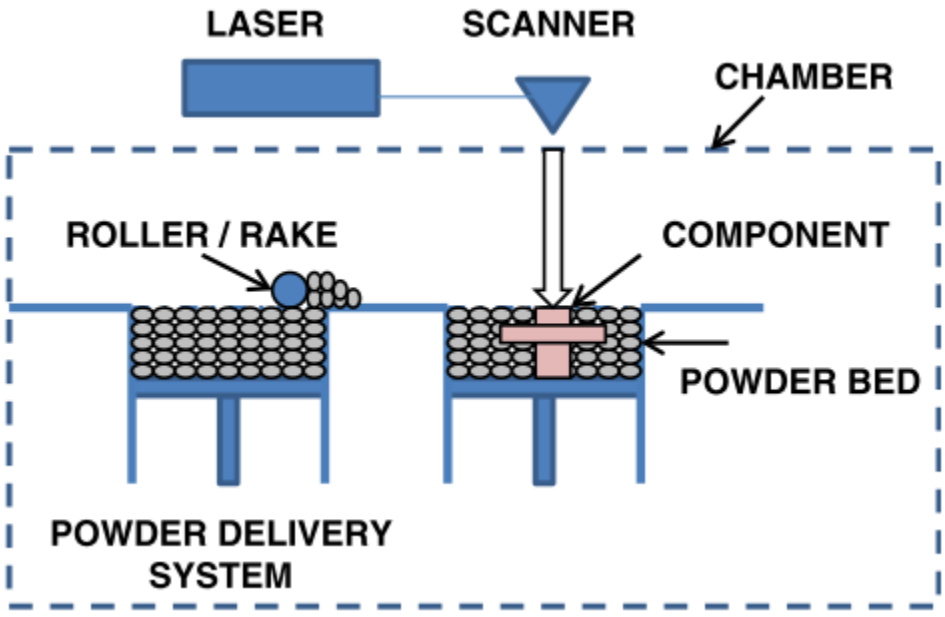

Figure 3: Schematic diagram of a typical SLM machine layout[4].

The powder handling system is generally comprised of a powder storage system, a powder spreading system, and a build platform. The powder storage is typically a hopper or piston which contains the stock of fresh powder is used to build the part. Powder is collected from this store by a spreading system, which collects a sufficient quantity to spread a thin layer onto the build platform. The laser system then selectively consolidates the spread layer, after which point the build platform lowers, making enough space to add an additional layer of fresh powder. This cycle continues until the entire part has been completed. In order to ease removal of the build part, a substrate (machined from a similar material as the powder) is used. When the build is completed, the finished part (which is fused to the substrate) is removed from the

surrounding powder bed, and is then separated from the substrate using conventional machining methods.

2.1.1 Processing Parameters

Before the start of the build specialized software is used to compile the sets of machine instructions that guide the process. A 3D model of the part is the input to a design software which performs several tasks. The first is to 'slice' the model horizontally; each horizontal slice represents a physical layer of powder in the eventual build. A pathway for the beam spot is then planned for each layer. Finally, processing parameters are codified to the build; for example, the laser power, or the speed of travel of the beam spot. These are then all translated into machine instructions. Figure 4 shows an example of the process that results from these machine instructions. The figure shows two successive layers of a simple cuboid shape being built. The bottom layer represents the material which has been consolidated by the previous pass. The top layer shows the active layer in the process of being consolidated. Surrounding the consolidated part is the fresh powder bed.

Part of the reason for the complex nature of the SLM process is the large number of process parameters that must be controlled in order to obtain parts with suitable quality. For example, the process parameters that guide the laser and optical system are laser power, laser velocity, and laser focus. The laser power is a variable that allows the emitted power to be increased or decreased. Laser speed affects the movement of the scanning device, which sets the speed of the laser spot as it moves across the surface of the build layer. The laser focus setting determines the spot size of the laser on the surface of the build. Other parameters control the application of fresh powder on the build platform. Foremost of these is the layer thickness;

however, there are also secondary parameters that control the speed and motion of the spreading apparatus, which will depend on the specific machine model. Some models have

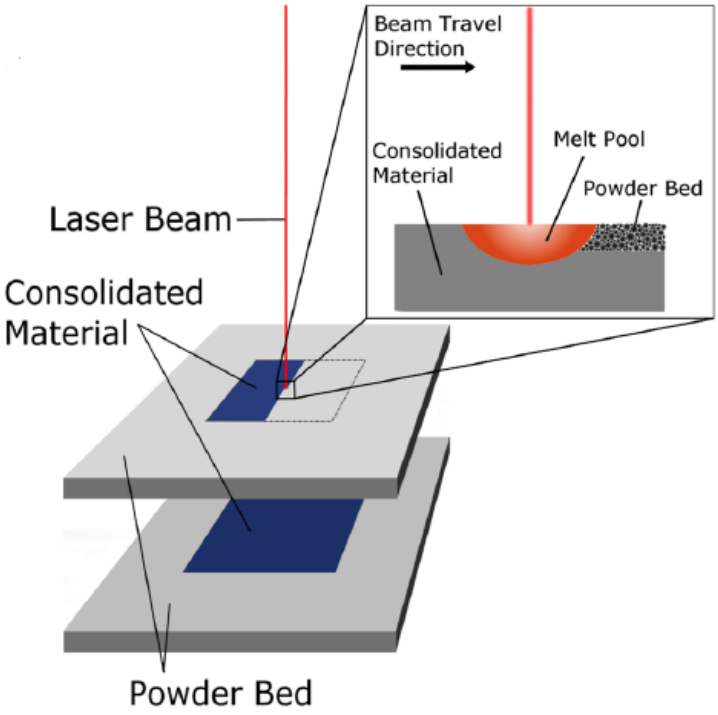

Figure 4: Schematic of the layer-by-layer process of a SLM PBF system [58].

compaction functionality, which is used to increase powder packing density; these come with additional controllable process parameters. The path of the beam is determined by the scan strategy; a schematic of the alternating cross hatch strategy is shown in Figure 5. This strategy is typically seen in research environments; alternate strategies are often employed in industrial settings. Such strategies are designed to minimize the vector length of straight-line beam travel by breaking up the layers into smaller sub-cells. This technique has been shown to decrease residual stresses [66]. The process parameter associated with use of the cross-hatch scan strategy is the hatch distance, which determines the amount of space between adjacent beam vectors.

Optimization of this parameter is critical, since increasing the hatch distance leads to faster build times, but also an increase in the amount of defects and a reduction in surface quality [67].

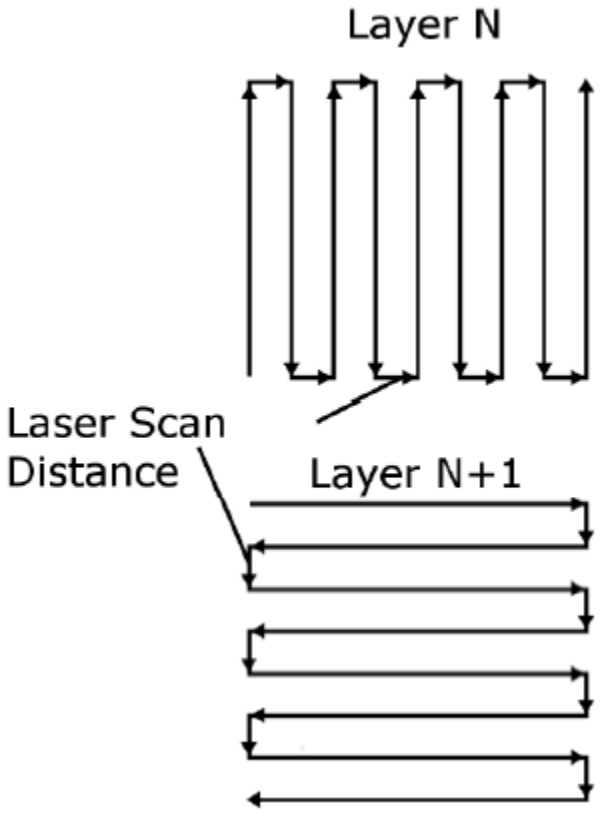

Figure 5: Schematic of the alternating cross hatch scan strategy. Each layer is constructed by rastering the beam back and forth across the layer. On each subsequent layer, the pattern is rotated 90°. The distance between each raster is the laser scan distance, also known as hatch distance [58].

2.1.2 The Melt Pool and Thermal History

The laser power and laser velocity are critical parameters which govern the size, thermal behavior, and quality of the melt pool. The melt pool characteristics determine the thermal history of the material, which controls the resulting microstructure. The energy input from the beam to the surface of the powder bed is typically modelled using a gaussian distribution;

experiments have shown that with proper calibration, such a distribution can closely approximate the true case [68]. Figure 6 shows a comparison of the cross section of a Ti-6Al-4V melt pool simulated using finite element analysis (FEA) (Figure 6a) and the cross section of a specimen built using SLM (b).

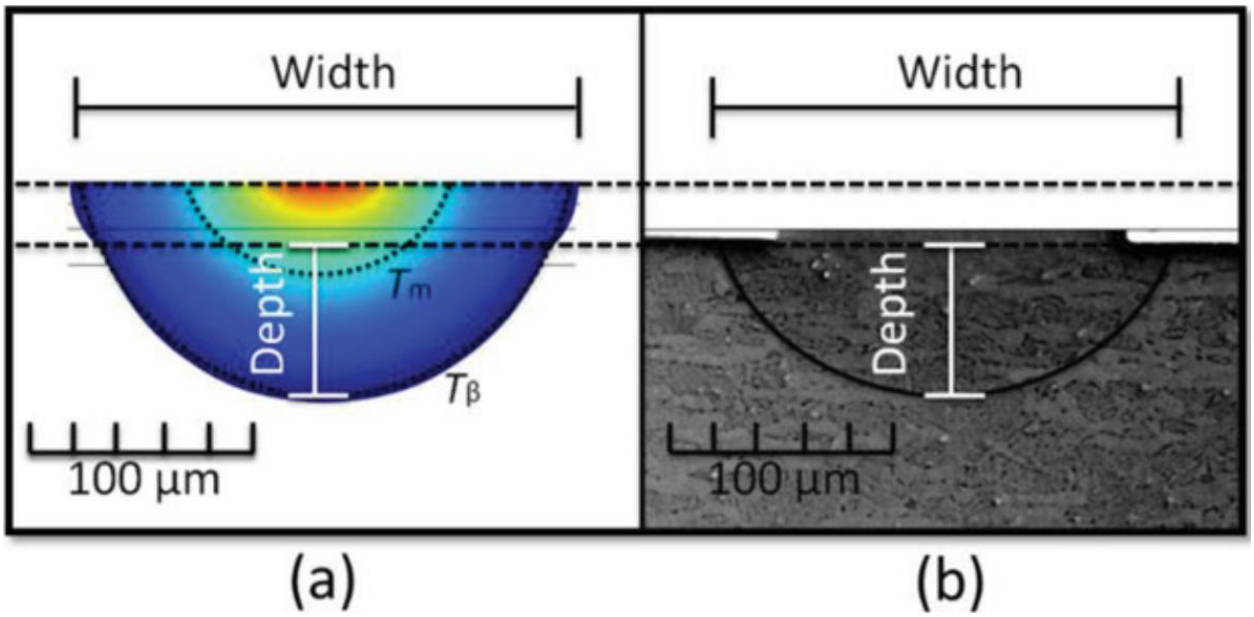

Figure 6: Comparison of FEA thermal simulation of the cross section of a Ti-6Al-4V melt pool (a) to experiment (b) [69]

It can be seen that due to the distributed nature of the beam energy as well as heat transfer from the beam center towards the cooler powder bed a characteristic temperature gradient appears. At the center of the melt pool the energy input is often sufficient to cause evaporation, creating a vapor plume [70, 71]. Exterior to the melt pool region is the heat affected zone, which reaches temperatures sufficient to cause microstructural evolution, such as grain growth, precipitation, and dislocation motion.

The shape, size, and quality of the melt pool and melt track can be controlled by the laser power and velocity. Studies of melt pool geometry using experiments of single laser tracks on a

substrate with a single layer of powder showed that increasing the laser power increased the depth and width of the melt pool. Increasing the laser velocity had the reverse effect. Additionally, the melt tracks exhibited distortion and balling phenomena at high and low laser velocities, which can be seen in Figure 7 [72].

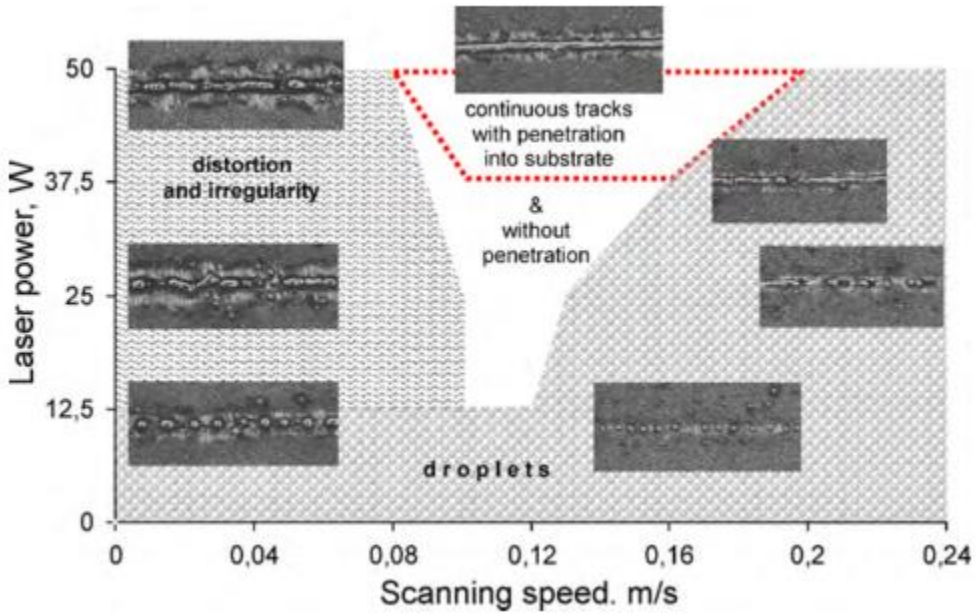

Figure 7: SEM images showing the quality of 316L steel single tracks. When the velocity was too high or too low, the tracks showed distortions or balling phenomena [72].

2.1.3 Defects

Distortion and balling should be avoided to ensure good surface quality and low porosity by selecting appropriate values for the laser power and velocity; furthermore, the layer thickness and the hatch distance must also be considered. Since these parameters affect the depth of the melt pool, care must be taken to ensure that the depth is sufficient to penetrate the top powder layer (set by the layer thickness parameter) into the previously melted layers. Additionally, the hatch distance and the width of the melt pool should be considered together. Depending on the width of the melt pool, the hatch distance must be sufficiently small in order to ensure sufficient

overlap between adjacent hatches, otherwise pockets of unmelted powder form between them as shown in Figure 8 [73].

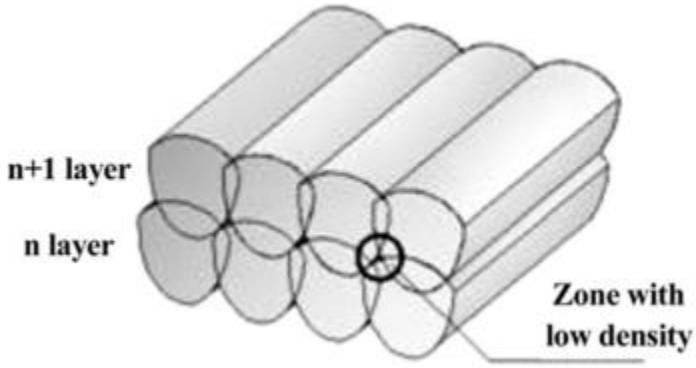

Figure 8: Schematic view of several adjacent melt tracks in two subsequent layers, showing the overlap between tracks and the region where unmelted pockets can form if process parameters are not carefully selected [73].

Material properties also have an influence on the thermal behavior during the SLM process. The heat transfer due to the interaction of the beam with the powder is affected by the thermal conductivity, the latent heat associated with melting and vaporization, and the heat capacity [68]. It is also affected by the effected density of the powder; this effective density depends both on the size distribution of the powder as well as the packing in the powder bed [21]. The fraction of total laser energy which is not reflected is the absorbtivity; in metals this factor is a material property which is dependent on the wavelength; additionally, in powder form the absorbtivity is reduced due to scattering [74].

Various defects result as an unavoidable side-effect of the SLM process. With proper selection of the process parameters and post-processing treatments the effect of these defects can be minimized. One such defect is residual stress. Residual stresses occur in other powder AM processes as well; however, they are greater in SLM parts than in EBM or DED [75]. These

residual stresses occur due to inhomogenous generation of plastic deformation during the cooling of the top molten layer. There are two proposed mechanisms for this. The first is shown in Figure 9. In this mechanism the steep thermal gradient results in lower yield points and greater thermal expansion in the upper, hotter portion of the heated material. This results in plastic deformation in the upper region. During cooling, the contraction of this plastically deformed region is constrained by the material below it, resulting in an oriented, planar tensile stress which is orthogonal to the beam direction [76]. The second mechanism attributes residual stress to the cooling to the thermal contraction of the top molten layer, which is constrained by the material below it, again resulting in an oriented tensile stress [76, 77].

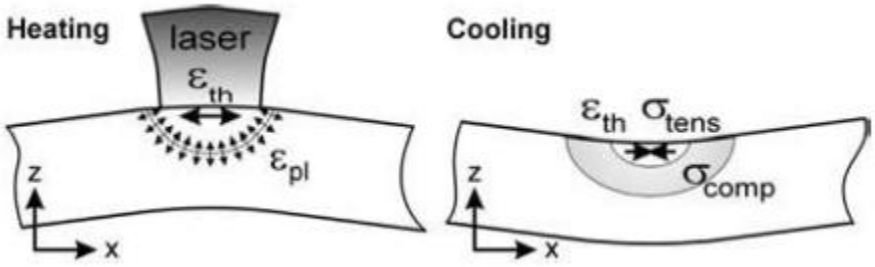

Figure 9: Mechanism of formation of residual stresses due to constrained expansion of top molten layers [76]

Excessive residual stresses can cause parts to crack during the process [9, 78], distortion of the part geometry after separation from the substrate [79-81], and negatively affect the performance of the material [15, 82, 83]. Apart from residual stress, cracking in SLM parts can be exacerbated by a number of mechanisms, including hot tearing, weakness at grain boundaries, and incomplete melting between layers [2].

Porosity formation has been a pervasive issue in SLM development, and a great deal of research has been done in order to understand how they form, how to minimize their appearance,

and how to detect them during processing. In industrial settings, it is common practice to apply hot isostatic pressing in order to reduce porosity as well as to close micro-cracks. Various mechanisms have been suggested to explain pore formation. These include the collapse of keyhole-mode melt pools [84], rapid enclosure of the gas contained in between powder particles before it can expelled through the melt pool surface [85], and due to the dynamic, splashing nature of the melt pool in conjunction with the rapid solidification [86].

2.2 A Review of NiTi and the SME

NiTi is a functional alloy that exhibits the shape memory effect. The SME occurs due to a diffusionless martensitic transformation which can be triggered by temperature change, applied stress, or in some cases applied magnetic field. The martensitic phase transformation occurs between two solid phases, by lengthening or contraction of lattice parameters, between the austenite phase which is stable at high temperatures and the martensite phase which is stable at low temperatures [87]. The temperature associated with the transformation are the martensitic start and finish temperatures (M_s and M_f) and the austenitic start and finish temperatures (A_s and A_f). In shape memory materials the martensitic transformation is fully reversible. By taking advantage of the martensitic transformation under different conditions of stress or temperature it is possible to obtain large reversible deformations. In the one-way SME, the material must be in the low temperature martensite state. In this state, the microstructure is made up of self-accommodated martensite twins. On the application of stress, the strain is accommodated by detwinning and martensite reorientation, rather than plastic dislocation, and proceeds by the motion of twin interfaces until only one or a few variants of the twins remain. When the stress is removed, the deformation remains. However, when the material is heated, the detwinned

martensite structure reverts to austenite, and the deformation is reversed [87-89]. The situation is shown in Figure 10. This case is called one-way because during cooling, no further deformation occurs.

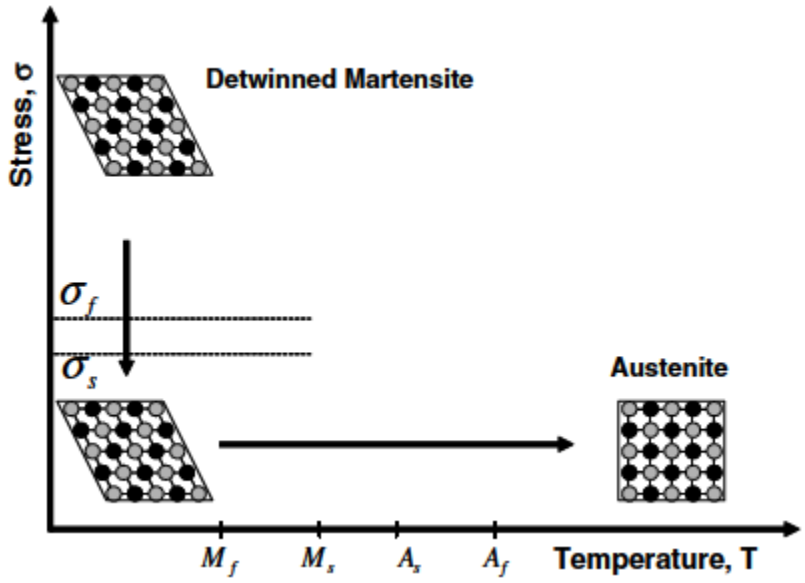

Figure 10: Diagram showing the one-way SME. Stress applied to twinned martensite results in a deformation that remains after the stress is removed. The deformation is reversed when the material is heated to transform to austenite [88].

Pseudoelastic transformation is achieved when stress is applied to the shape memory material when it is above the A_f temperature. In this case, a stress is applied to the austenite, upon which the material undergoes a stress-induced transformation to detwinned martensite. The deformation associated with this transformation can be of an order of magnitude greater than conventional elastic deformation. When the stress is removed, the material transforms back into austenite, and the deformation is reversed fully. This is shown in Figure 11. In NiTi, the austenite has the B2 CsCl structure, and the martensite has the B19' monoclinic structure [90].

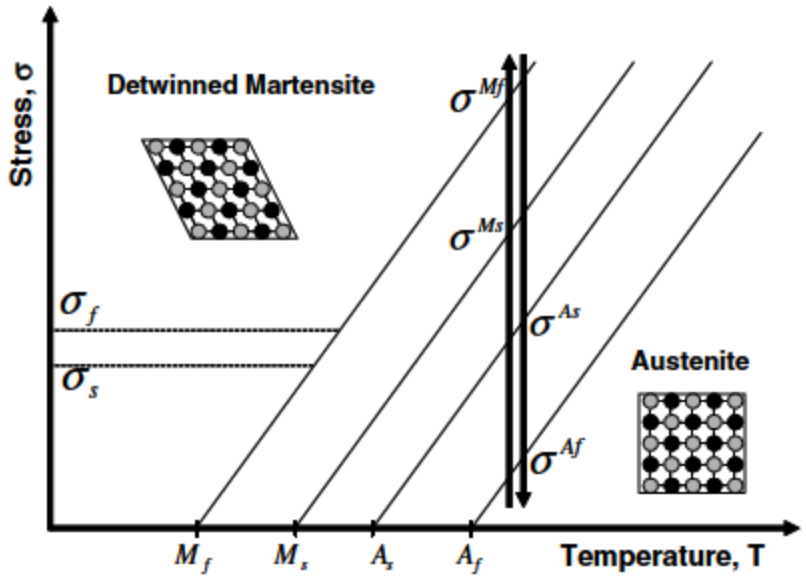

Figure 11: Diagram showing pseudoelasticity. Stress is applied to austenite, resulting in a stress-induced transformation to martensite. The large deformation associated with the transformation is reversed when the stress is removed [88].

The relationship between the transformation temperatures and microstructural and composition changes can be understood the Gibbs energy formulation put forward by Ortin and Planes [91]. The energetic requirement for the forward transformation between austenite to martensite, and the reverse transformation from martensite to austenite is given by:

$$-\Delta G_{ch}^{A-M} + \Delta G_{rev}^{A-M} + \Delta G_{dis}^{A-M} = 0$$

$$-\Delta G_{ch}^{M-A} - \Delta G_{rev}^{M-A} + \Delta G_{dis}^{M-A} = 0 \quad (1)$$

where ΔG_{ch}^{A-M} and ΔG_{ch}^{M-A} are the chemical Gibbs free energy differences between austenite and martensite for the forward and reverse transformations respectively, ΔG_{rev}^{A-M} and ΔG_{rev}^{M-A} are the reversible Gibbs free energy barriers, and ΔG_{dis}^{A-M} and ΔG_{dis}^{M-A} are the dissipative Gibbs free energy barriers [44, 91]. The equations (1) show that the reversible and dissipated energy barriers must be balanced by the chemical term, which is achieved by undercooling or

superheating. The dissipation term, as expected, opposes transformation in both the forward and reverse directions and always increases the energy cost. The reversible energy imposes an energy cost in the forward direction, but aids the reverse transformation. This is shown schematically in Figure 12.

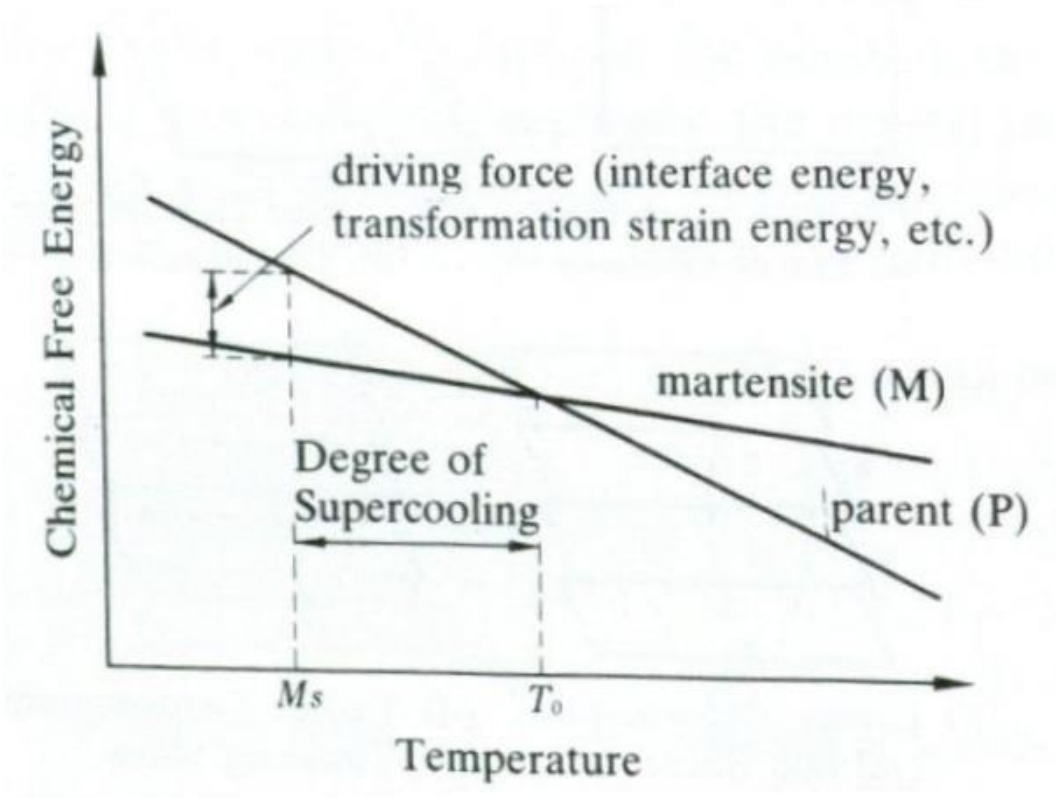

Figure 12: Schematic Gibbs energy curves for martensite and austenite. Supercooling provides the driving force to overcome energy barriers associated with the transformation [89].

2.2.1 Relationship between Microstructure and Transformation Temperatures

It can be seen that the transformation temperatures shift depending on the energy cost required for the transformation and to T_0, which is temperature at which the chemical Gibbs energies of martensite and austenite are equal. In NiTi, the transformation temperatures are

strongly dependent on the NiTi composition ratio, due to the shift in the Gibbs energy curves and thus T_0. This can be seen in Figure 13.

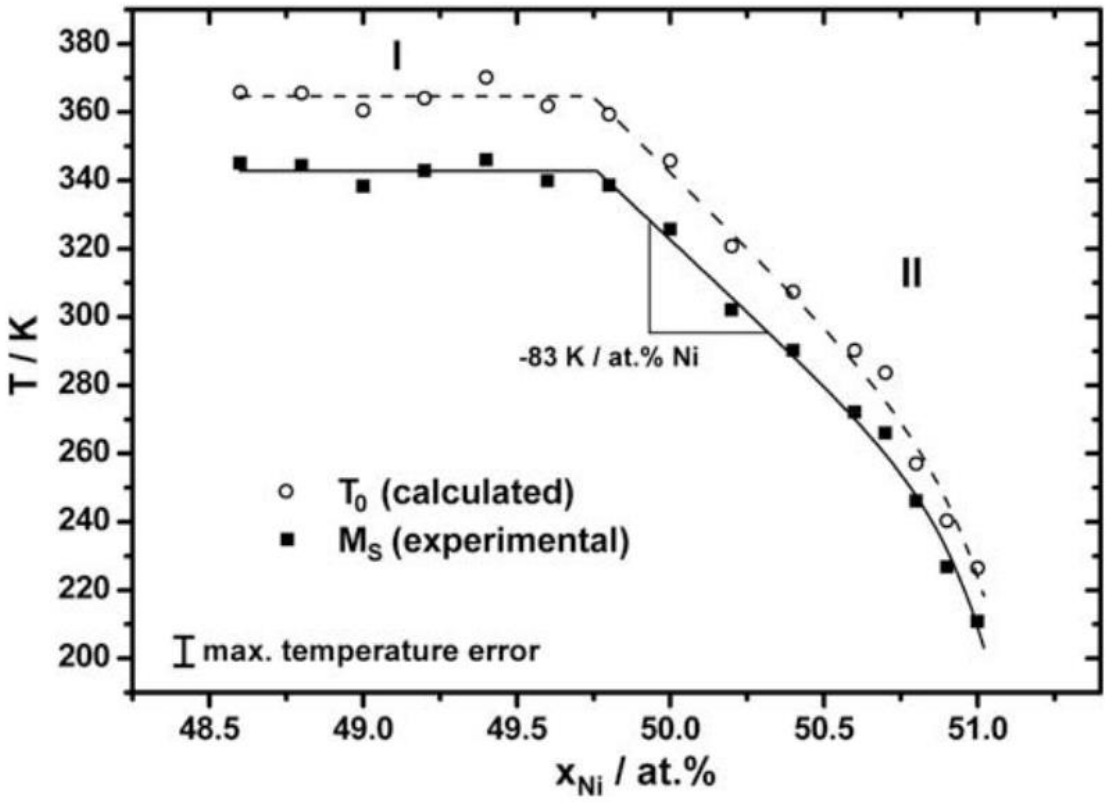

Figure 13: Effect of Ni content on the M_s temperature and calculated T_0 temperature [43].

Below equiatomic NiTi ratios, the M_s temperature remains relatively constant at 70°C. As the Ni content increases, the M_s temperature begins to decrease, and is sharply suppressed on reaching 51 at% Ni.

Precipitation in NiTi affects the transformation temperatures by a number of competing mechanisms. Figure 14 shows the phase diagram for the NiTi system. On the nickel-rich side of the diagram the precipitates that can form are Ni_4Ti_3, Ni_3Ti_2, and Ni_3Ti. Ni_3Ti_2 and Ni_3Ti form at higher temperatures and longer durations of aging [90], so during SLM processing Ni_4Ti_3 is expected. On the Ti-rich side, Ti_2Ni precipitates can form.

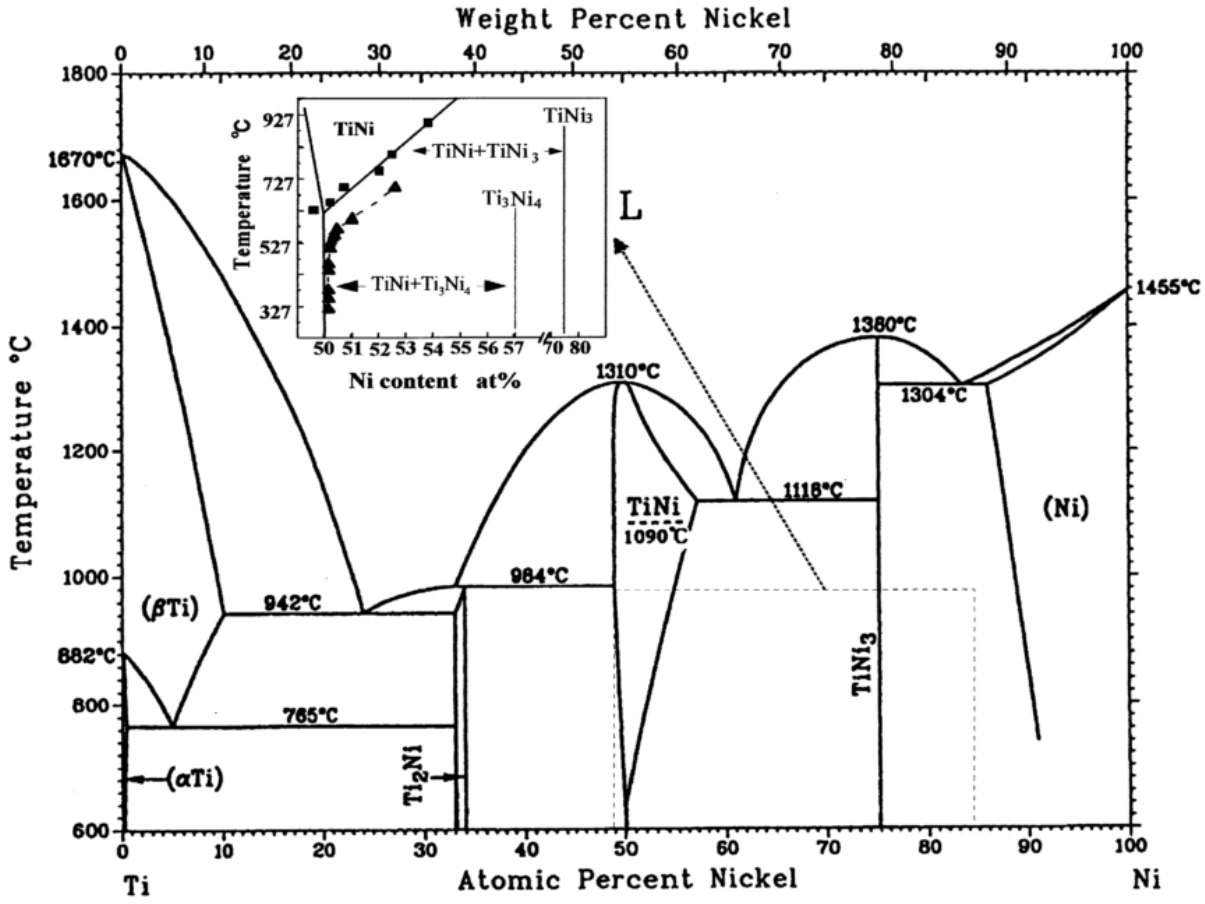

Figure 14: The NiTi phase diagram [90].

Formation of the precipitates changes the Ni content of the matrix. In a Ni-rich material with formation of Ni_4Ti_3, the matrix Ni content will decrease, shifting the transformation temperatures higher. In a Ti-rich material with Ti_2Ni, the transformation temperatures remain constant with Ni content, so they do not shift. The volume fraction and interparticle distance of precipitates has an effect on the thermal hysteresis ($A_f - M_s$). When the precipitates densely populate the matrix, with a small interparticle distance between them, additional reversible and dissipative energy is required to advance the martensitic transformation. This has the effect of suppressing the

transformation temperatures [44, 92]. When the interparticle distance increases, for example by coarsening induced by aging, the transformation temperatures increase.

The other microstructural factors that affect the transformation temperatures can be summarized by the following:

- Increases in dislocation density increase the temperature difference between the start and finish of both transformations, I.E. broader transformations [47].
- Applied oriented stress increases the transformation temperatures by a linear factor of 6-10 MPa/°C in NiTi [46].
- Decreases in grain size to the nanoscale increases the thermal hysteresis, which has the effect of suppressing the transformation temperatures [48].
- Crystallographic texture can alter the hysteresis depending on the orientation relationship of the applied stress direction and the primary orientations of the texture [49].

These are also shown in figure form to demonstrate: effect of precipitation (Figure 15), effect of grain size (Figure 16), effect of stress (Figure 17), and effect of dislocation density (Figure 18).

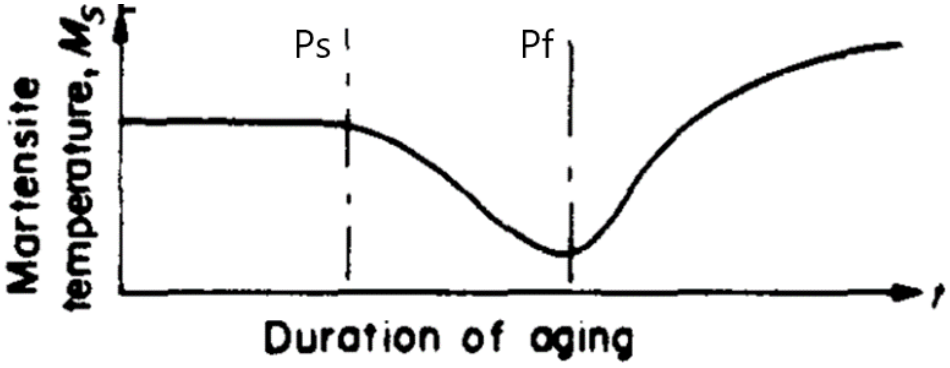

Figure 15: Diagram showing the effect of precipitation on the M_s temperature, with the combined effect of composition change and interparticle distance change. At P_s, the nucleation of precipitates causes the interparticle distance to decrease, suppressing M_s. At P_f, the coarsening of precipitates increases the M_s, and after sufficient aging the M_s is higher than the initial state due to the decrease of Ni in the matrix [45].

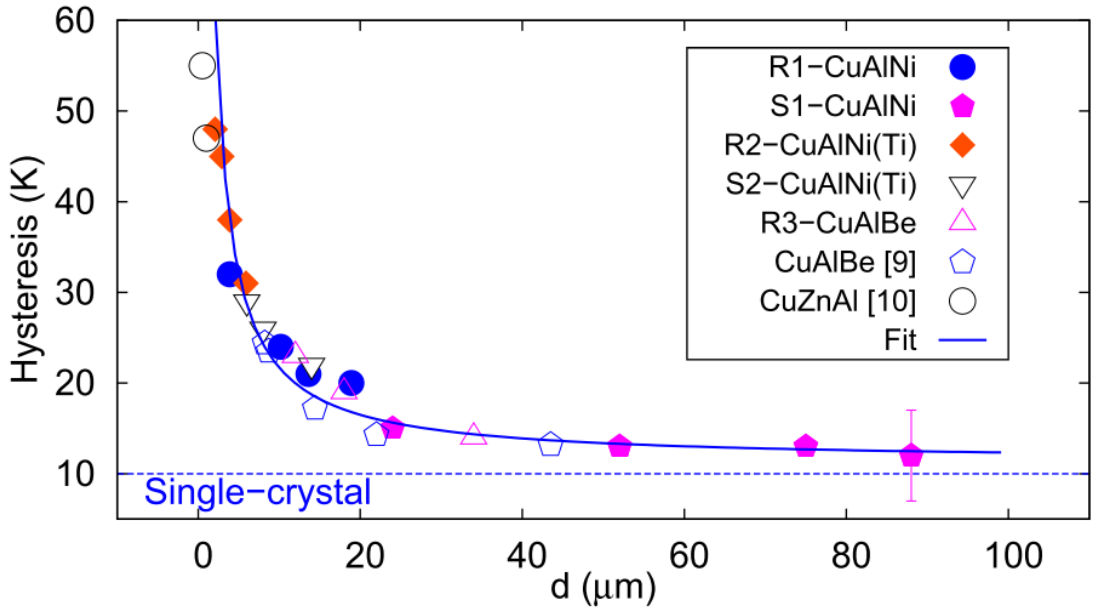

Figure 16: Effect of grain size on the thermal hysteresis in Cu-based shape memory alloys. When the grain size is above 20μm there is no appreciable change, but upon reaching the nanoscale increases dramatically [48].

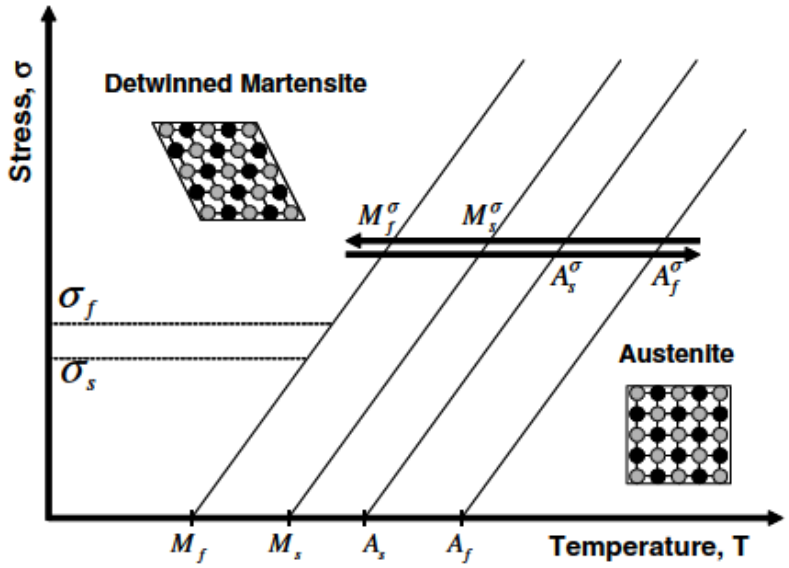

Figure 17: Diagram showing the effect of stress on the transformation temperatures. The indicated transformation path show that on heating and cooling at elevated stress, the transformation temperatures also increase [88].

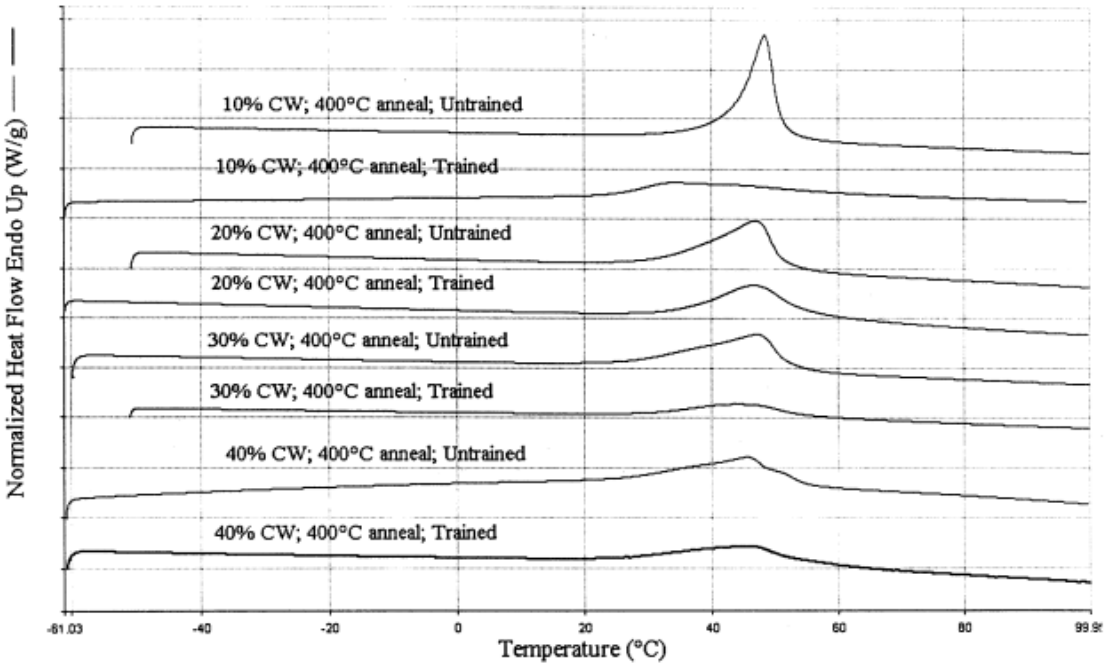

Figure 18: Effect of cold work and dislocation density on transformation temperatures. The peaks represent differential scanning calorimetry (DSC) curves during the forward transformation. The peaks in heat flow indicate transformation. It can be seen that when the extent of cold work is increased, the peaks broaden [47].

2.3 A Review of SLM-built NiTi

The earliest research works investigating SLM-built NiTi were motivated by demonstrating the capability of this technique for certain applications. In 2006, Chalker et. al. used SLM to build Ni-rich NiTi springs for a MEMs application; the springs were then successfully trained for two-way shape memory effect (TWSME) behavior by repeatedly compressing and heating them [93]. This work appears to show the first published results demonstrating successful usage of SLM to build NiTi parts, as well as the first example of TWSME in such parts. The same group replicated their results two years later using cantilever beams [94]. Over the next few years the trend of application-centric research continued, with demonstrations of scaffolds for orthopedic implants [55, 56, 95-98], research into properties with

a focus on biomedical devices [99, 100], and actuators with complex lattice geometries [101]. In 2010, Meier et. al. published a work which investigated the effect of process parameters on porosity, microstructure, and shape memory behavior of a Ti-rich NiTi alloy [102]. Following this, between 2010-2015 a small number of works investigating process-performance-microstructure relationships were published. However, between 2016 and 2018 there was a dramatic growth of research interest and a large number of such works were published. Currently, there exists a large body of work on this topic, which will be reviewed in the following sections.

2.3.1 Process Parameters for SLM-built NiTi

The microstructure, properties, and shape memory behavior of SLM-built NiTi are dependent on the process parameters. There is a wide range of process parameters that have been previously used in the literature to produce dense parts; these are summarized in Table 1. Note that a number of works replicate the process parameters of previous works, and those are not shown in the table. Also, some earlier works do not report the process parameters, choosing instead to report the volumetric energy density. The volumetric energy density is calculated by

$$\mathrm{E}_v = \frac{P}{V * t * h} \tag{1}$$

where E_v is the volumetric energy density, P is the power, V is the velocity, t is the layer thickness, and h is the hatch distance. As can been seen from the table, the previously explored parameter space is quite large. The literature has reported successful builds using P as low as 36W, all the way up to 300W; V between 60 mm/s and 2000 mm/s, and hatch distances between 50-200μm.

Table 1: Published process parameters and Ni content of studies of SLM-built NiTi.

Ni Content (at%)	Laser Power (W)	Laser Speed (mm/s)	Hatch Dist. (μm)	Ref.
49.3	80	NR	50-200	[93]
51.1	60-80	171-133	120	[23]
49.9	50	160-120	80	[103]
49.9	50	60-220	80-160	[98]
50.8	100-250	100-1250	90-120	[24]
50.9	56-100	107-297	120	[34]
50.1	40-250	160-1100	50-75	[30]
49.7-50.7	36-77	100-600	NR	[25]
50.2	250	1100	60	[36]
50.8	250	1250	120	[38]
50.6	40-250	160-1042	50-80	[33]
50.1	50-300	100-2000	120-700	[104]
NR	75-200	313-1333	50-80	[105]
50.8	100-250	125-1500	120	[106]

Haberland et. al. examined the relationship between process parameters (P and V) on the quality and diameter of single melt tracks. By examining single tracks laid onto a single layer of powder, it is possible to determine the process window where tracks are continuous and stable, and the melt pool diameter, which determines the suitable hatch distance to ensure proper

overlap between adjacent tracks [72]. Haberland et. al. investigated combinations of P and V where P was between 36-77W, and V was between 100-600 mm/s [25].

It was found that high V (600 mm/s) and low P (36W) were not sufficient to yield continuous tracks. Additionally, it was observed that the porosity decreased as energy density increased, with a minimum of 200 J/mm^3 required to yield fully dense parts. This is shown in Figure 19. Finally, the energy density was also linked to the level of oxygen, nitrogen, and carbon contamination in the finished samples (Figure 20). While energy density of 200 J/mm^3 yielded fully dense parts, it also resulted in elevated levels of oxygen and carbon contamination (Figure 20).

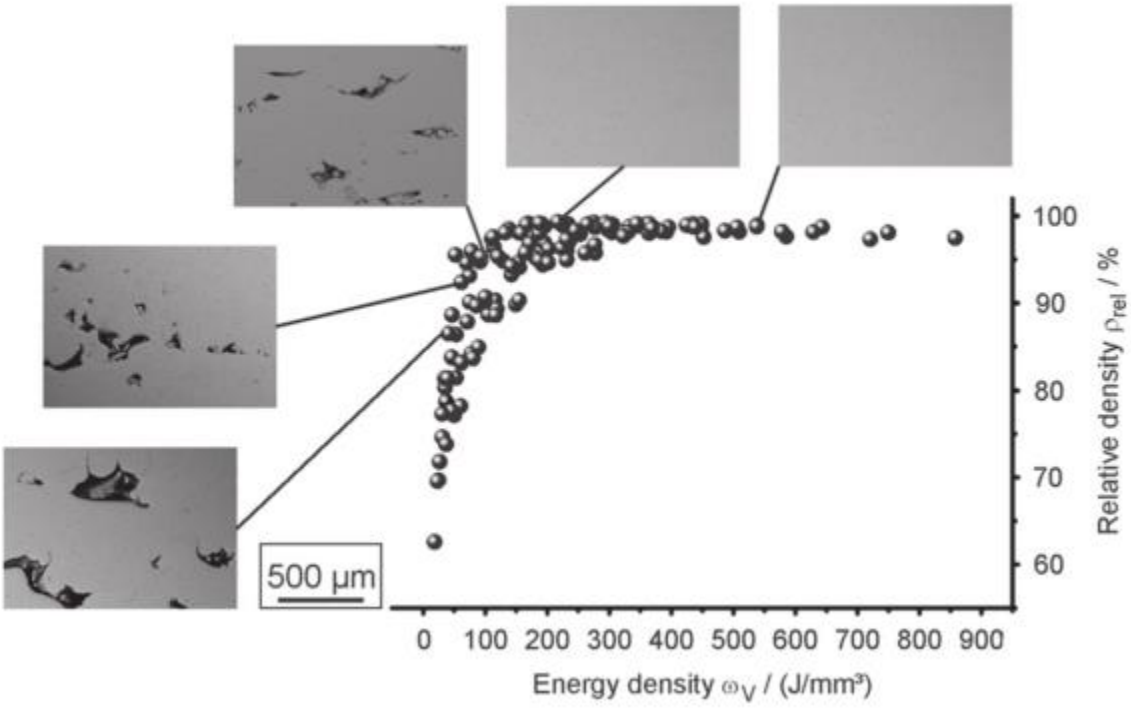

Figure 19: Relationship between energy density and part density in NiTi [25].

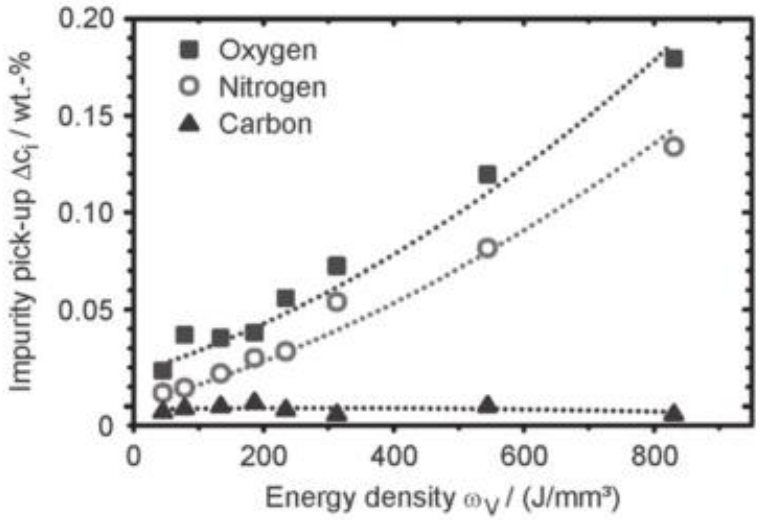

Figure 20: Relationship between contamination and energy density in NiTi [25].

Later, Walker et. al. re-examined single tracks in NiTi but using higher P, with the range of P between 50-300W [104]. Walker found that there was a maximal density that could be obtained in both the V and energy density spaces. When the V or energy density were too low, or too high, the part density began to decrease. Figure 21 shows the relationship between V on the part density at different levels of P. At a given level of P, there is a maximum in part density, with lower density observed with lower and higher scan velocities. As the P value increased, the V at which the maximum density was observed also increased. Figure 22 shows the part density with respect to energy density. Contrary to the earlier results of Haberland, it was observed that excessive energy density resulted in higher porosity. This is likely due to the fact that Haberland's results used a maximum of 77W. The porosity in high energy density (i.e. high laser power, low velocity) parameter sets has previously been attributed to instability in the melt pool resulting from the dynamic nature of the thermal process in the high energy input regime [72]

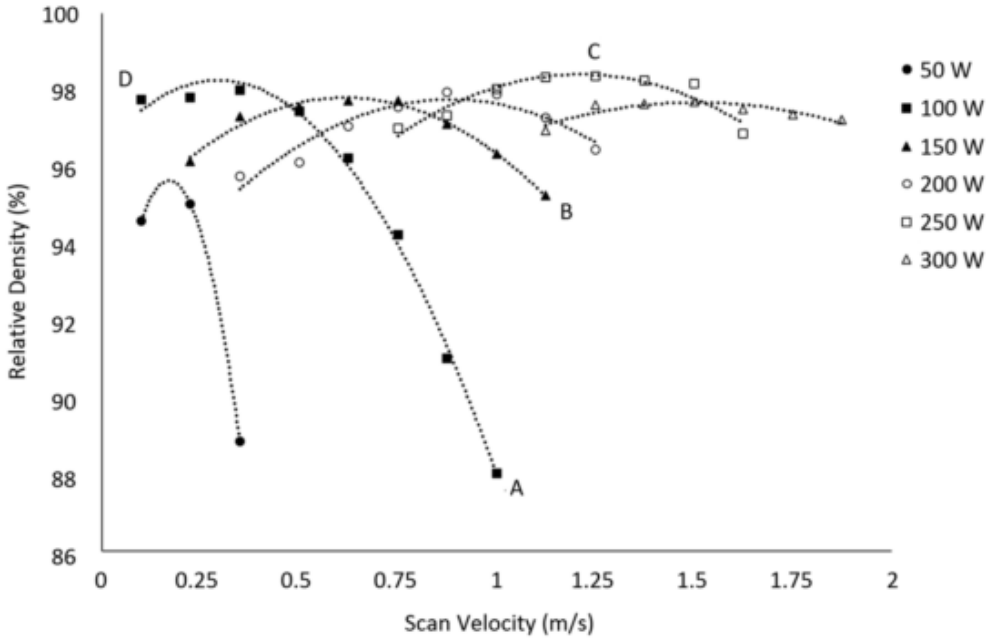

Figure 21: Effect of velocity on part density, using various levels of laser power [104].

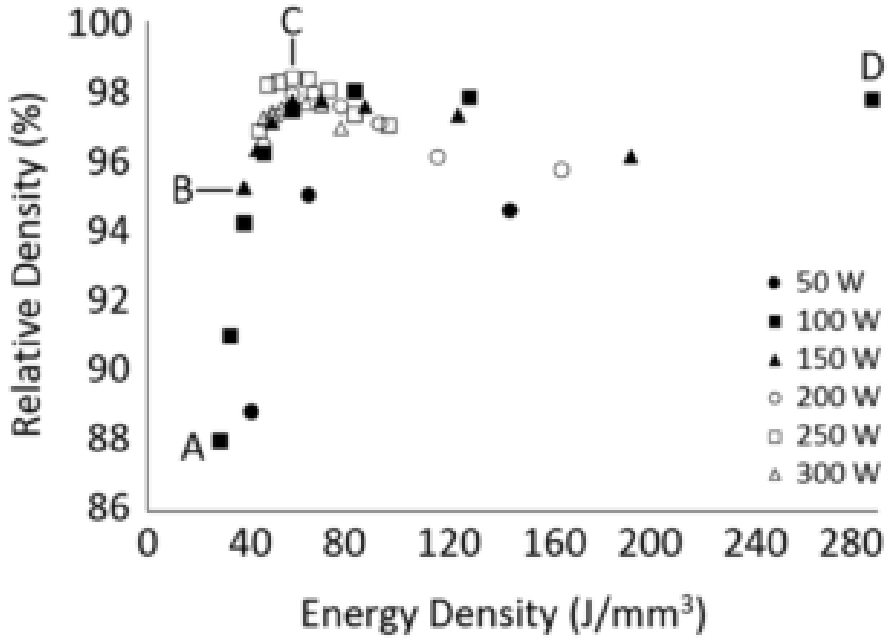

Figure 22: Study of effect of energy density on part density by Walker et. al. [104].

2.3.2 Effect of Process Parameters on Transformation Temperatures

Various works have investigated the relationship between the process parameters on the transformation temperatures under zero stress conditions. Haberland et. al. measured the transformation temperatures using differential scanning calorimetry (DSC). It was found that when the starting powder Ni content was higher (50.7 at%) the M_s temperature increased with energy density (Figure 23) [107]. When the Ni content was closer to equiatomic, the M_s temperature remained relatively constant with energy density.

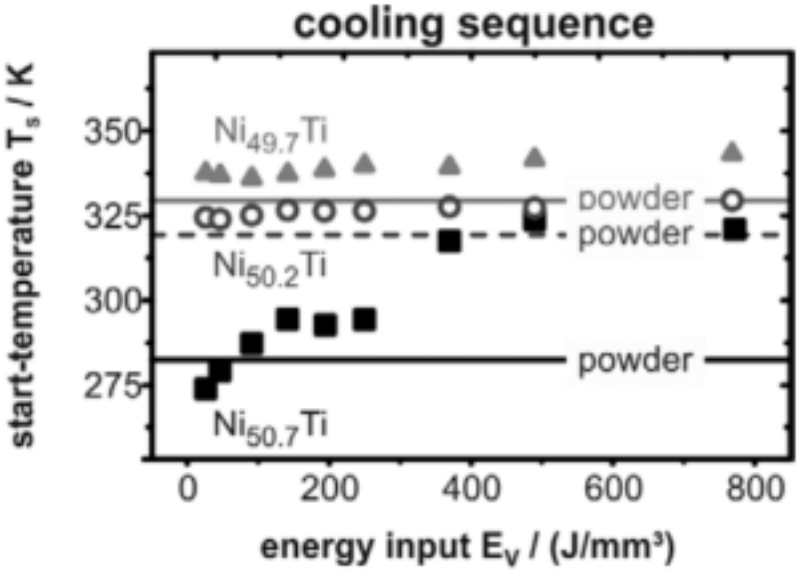

Figure 23: Effect of energy density on M_s temperature of various Ni compositions [107].

Due to the fact that the transformation temperatures did not shift in the near-equiatomic composition materials, the change of M_s was attributed to the formation of Ni-rich precipitates and the evaporation of Ni at high energy densities. Bormann et. al. also observed a similar trend in a Ni-rich 51.1 at% composition [23].

Contrary to these results, Dadbakash et. al. investigated several parameter sets using low P (40W) and high P (250W), while keeping the energy density relatively constant (102-126

J/mm^3) [30]. It was found that samples built using lower P had M_s temperatures 41°C higher than those built using higher P. This study used a wider range of P than the previous studies by Haberland and Bormann, so just as the effect on part density, not only the energy density but the P and V must be considered.

Speirs investigated the effect of process parameters using V rather than energy density [33]. It was found that the M_s temperature decreased with increasing V (Figure 22). It was also observed that under some process conditions very broad transformation peaks occurred, and this was attributed to inhomogeneity. The effect of oxygen in the chamber was also examined; when the oxygen level was 220ppm, the M_s temperature was less sensitive to the effect of V than when the oxygen level was 1800ppm.

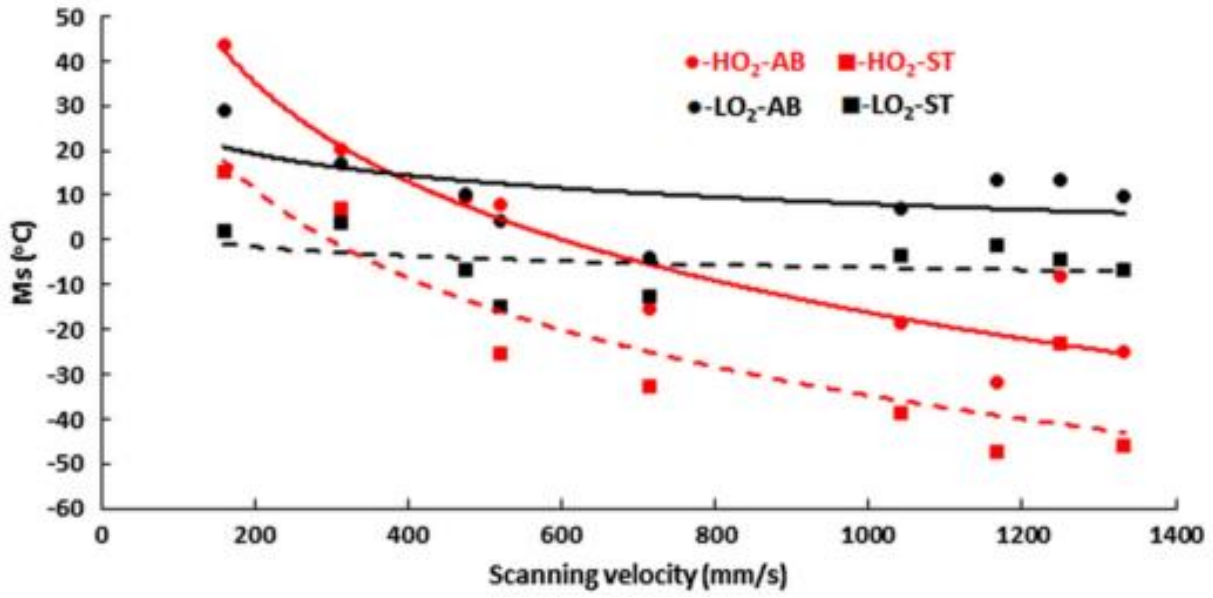

Figure 24: Effect of V on M_s temperature. AB curves are as-built, ST curves are solution treated. HO_2 curves were processed under high oxygen conditions, LO_2 under low oxygen [33].

2.3.3 Mechanical Properties

While there have been several works investigating the broad effect of changing the process parameters on the transformation temperatures, the studies of thermomechanical behavior have been limited to fewer, individual process parameter sets; additionally, most of the current works have studied samples under compressive load, rather than under tensile loads.

Haberland et. al showed that it was possible to produce SLM-built NiTi samples with properties comparable those of conventional NiTi under compression [29]. Pseudoelastic reversible strains of 3% were obtained, and it was shown that the cyclic stability response matched that of conventionally processed NiTi (Figure 25).

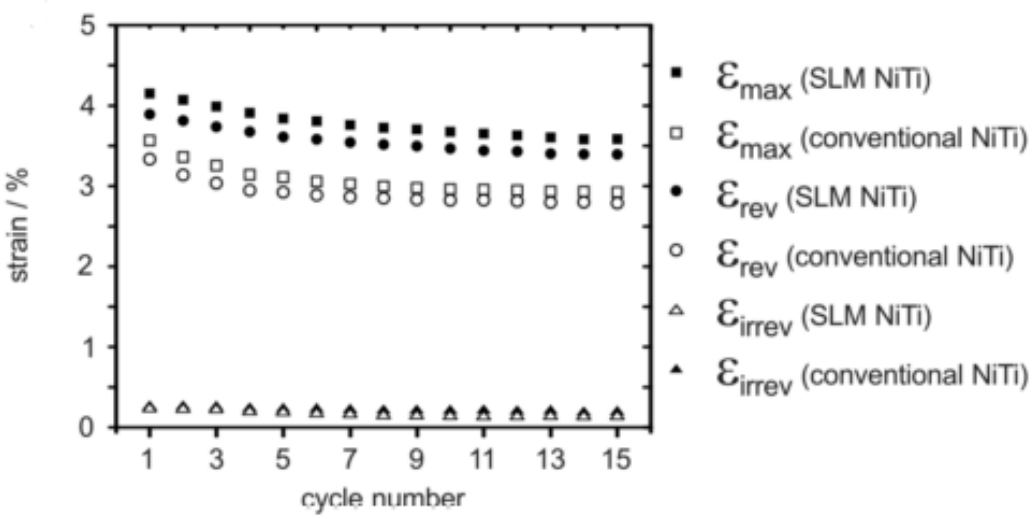

Figure 25: Evolution of strains during pseudoelastic cycling for SLM-built NiTi and conventional NiTi [29].

Later, Moghaddam et. al obtained pseudoelastic reversible strains of 5.6% under compression [108]. The higher reversible strain was attributed to the use of high P (250 W) in order to reduce porosity and cracking, while also using a smaller hatch distance of 80μm.

Several works investigated the effect of heat treatment on the thermomechanical response; it was found that solution treatment and aging treatment were effective at improving the recoverable strain [32, 38, 41]. Studies of mechanical behavior in tension showed that significant transformation strains of 4.5% could be achieved with the correct process parameters [40]. However, the samples were brittle, and broke under relatively low loading conditions [35, 40].

Anisotropy of mechanical properties is known to occur in SLM materials, and this has also been confirmed in NiTi shape memory behavior. Several studies have observed strong texture in the direction of the beam [36, 41]. Differences in recoverable strain, stiffness, and ultimate tensile strength depending on the direction of the test samples has also been reported [36, 109].

2.3.4 Variability in the Literature

Currently, there has been little attention paid to variability or repeatability in SLM-built NiTi. A review of the current literature revealed that out of 35 works that gave experimental results (19 being DSC experiments and 20 with mechanical testing) only 1 work showed statistical values such as standard deviation, and 5 works gave error bars. Only 7 papers performed repeated experiments (Figure 26).

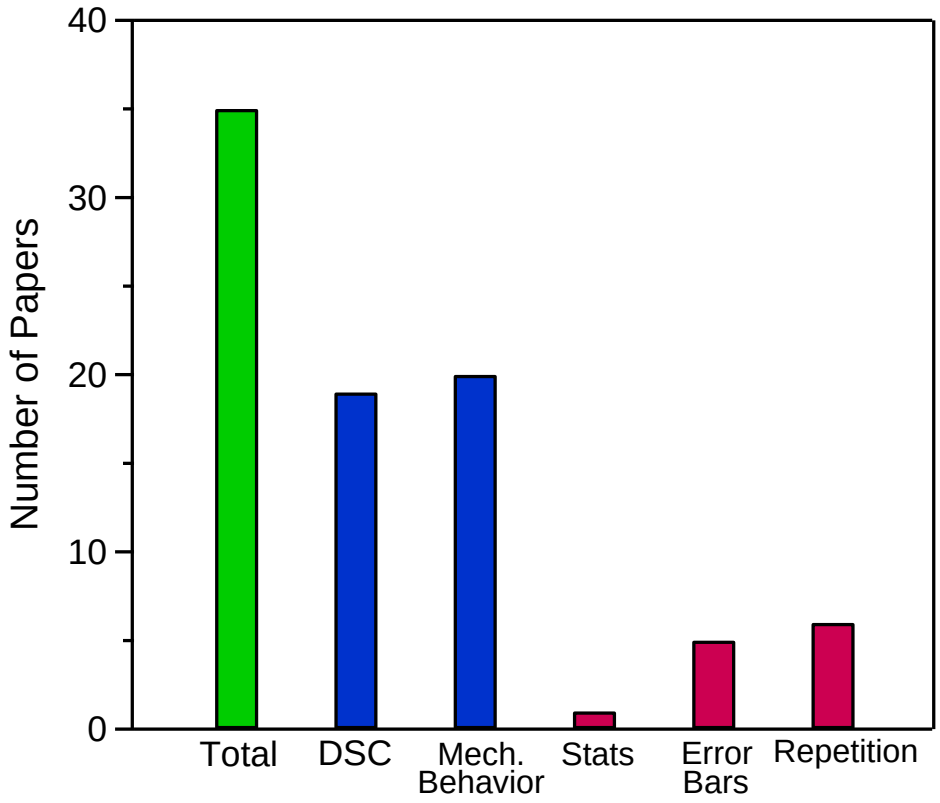

Figure 26: Review of statistical reporting in the current literature.

In the broader context of SLM across all materials, there have also been very few studies that have addressed this issue. Luecke et al. compared the variation in ultimate tensile strength and yield strength of UNS 17400 stainless steel to results obtained from a conventional wrought product [10]. It was found that the normalized standard deviation was twice as large for additive products than for wrought products. Brown et. al studied the effect of machine-to-machine variability by obtaining Nickel alloy 625 powder and sending it to a number of different research groups, where identical specimens were printed using identical process parameters but on different SLM machines [11]. It was found that despite every effort to keep the build conditions

identical, there were significant differences in mechanical properties, and the variability in mechanical properties, from machine to machine (Figure 27).

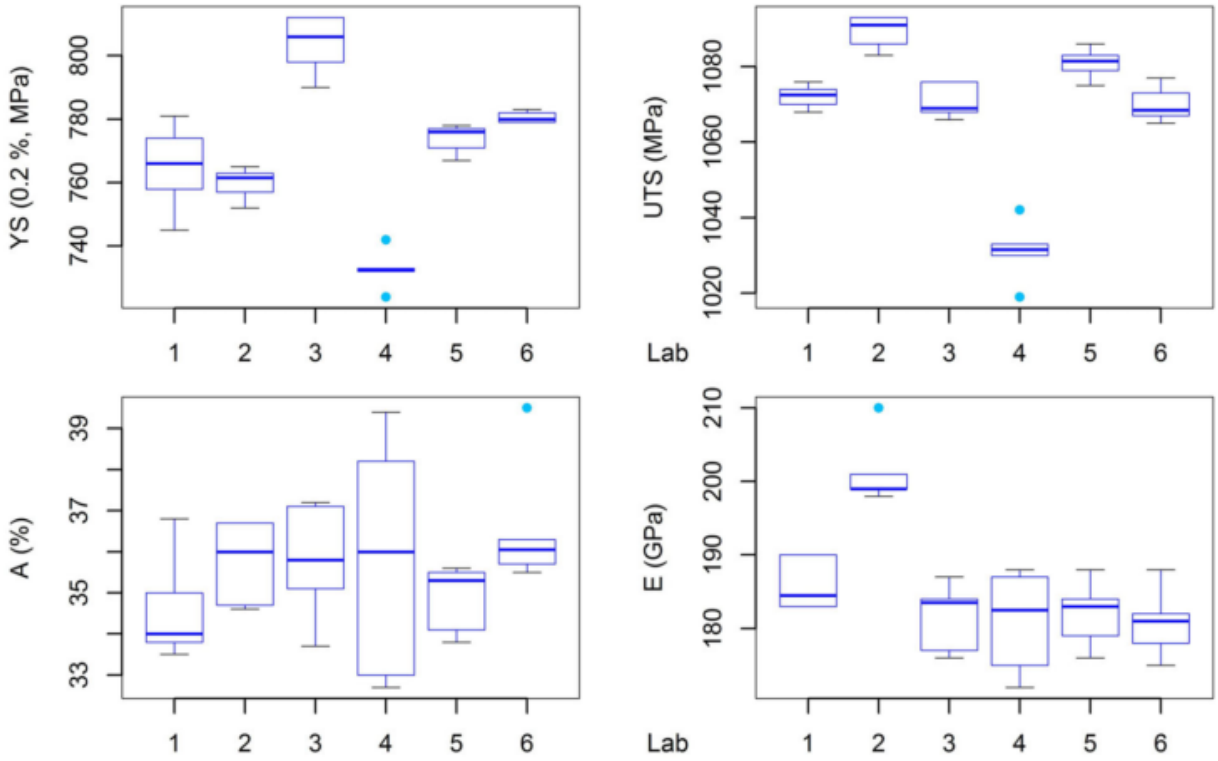

Figure 27: Machine-to-machine variability study of mechanical properties [11].

CHAPTER III

EXPERIMENTAL METHODS

This chapter reviews the conditions, procedures and equipment used to fabricate, process, characterize, and test the materials used in the current work.

3.1 Feed Stock Fabrication

A 32mm diameter, 7.5kg rod with a nominal composition of 50.9at% NiTi was commercially produced using vacuum induction melting by SAES Getters S.p.A. This starting material was then gas atomized under argon into powder with a d_{50} of 18.5µm. Figure 28 shows the measured powder size distribution. The batch was sieved using a 170 mesh screen to remove larger particles. The remaining 5kg of powder retained a particle distribution that is suitable for laser powder bed manufacturing. The powder was stored under high purity argon in a glovebox between uses, and virgin powder was kept separately from recycled powder.

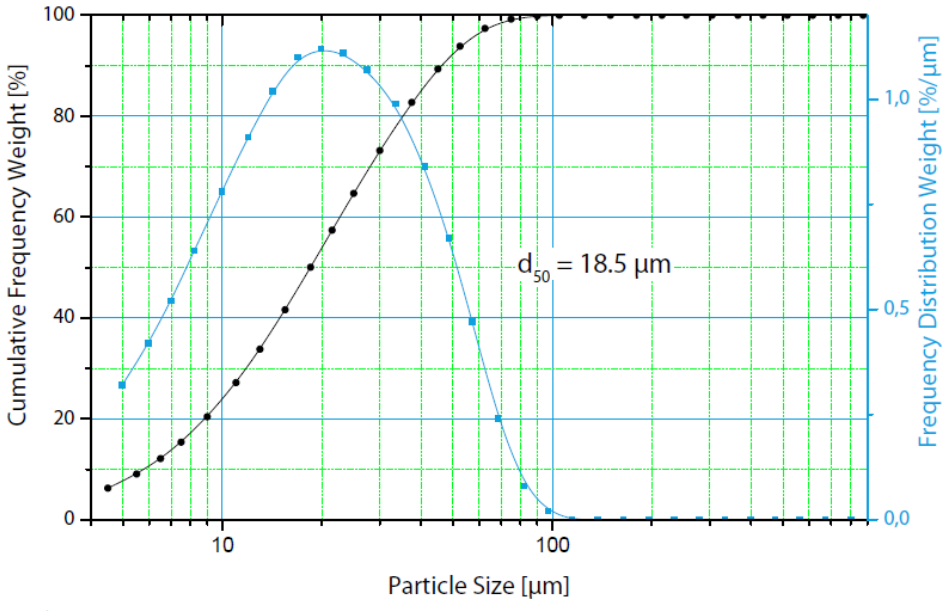

Figure 28: Particle size distribution and cumulative particle size distribution of the gas atomized NiTi material. Courtesy: Nanoval GmbH.

3.2 Sample Fabrication

The powder was consolidated using a 3D Systems ProX 100 3D printer equipped with a 50W maximum power, 1070nm wavelength laser. The build area was shielded using an argon purge system, equipped with an oxygen sensor to ensure a low level of ambient oxygen during printing. The samples were printed onto substrates machined from equiatomic NiTi bulk material. After printing, samples were removed from the substrate using electrical discharge machining (EDM). Individual specimens were taken from each sample by further EDM processes.

3.3 Characterization of Shape Memory Behavior and Mechanical Testing

Detection and measurement of transformation temperatures was performed using DSC. Small specimens weighing between 30-60 mg were cut with a 3mm diameter. The samples were tested in sealed aluminum pans under flowing nitrogen, with a heating cooling rate of 10°C/min. The equipment used was a TA instruments Q2000. After testing, the transformation temperatures were determined using the tangent method on the heat flow vs. temperature data. Figure 29 shows typical DSC curves for NiTi in various conditions. At the top of the figure is the single step B2-B19' transformation expected for single phase NiTi without precipitates. In the middle of the figure is the B2-R-B19' R-phase transformation observed in Ni-rich materials after aging. At the bottom of the figure is the multiple step transformation which is observed in medium Ni content materials where precipitates nucleate inhomogenously.

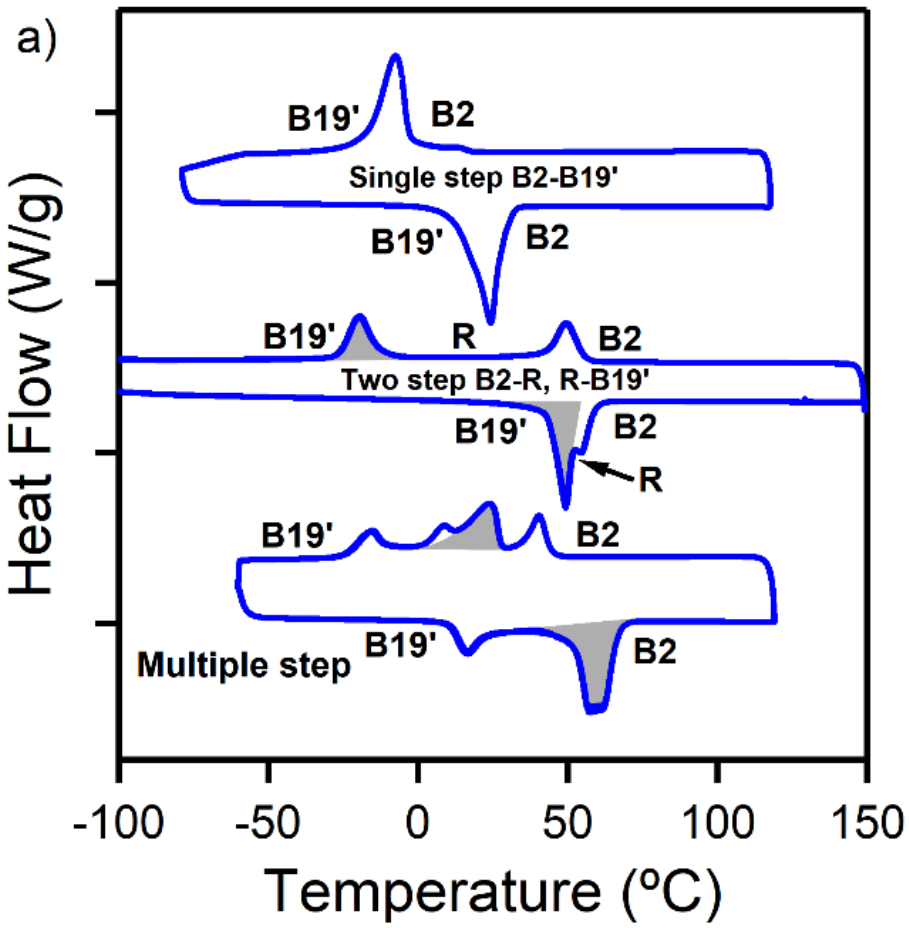

Figure 29: Typical DSC curves showing various expected shape memory responses for NiTi. Top: Single step transformation. Middle: R-phase transformation. Bottom: Multiple step transformation.

Mechanical testing specimens in the shape of 1mm thickness compact dogbones with a gauge section of 3x8mm were cut from individually printed larger blocks such that each block yielded multiple specimens. The printed blocks had dimensions of 28x32x12mm. After EDM cutting the specimens from the printed blocks, each specimen was mechanically ground to remove the EDM layer using papers up to 400 grit. The samples were cut from the interior material of each block to avoid the outer printed layers, which contain a higher fraction of porosities. The samples were tested on a servohydraulic MTS tensile test frame instrumented

with a high temperature extensometer. Heating and cooling were performed by conduction through the grips, with heating applied by resistance bands, and cooling by flowing liquid nitrogen through copper tubing coils wrapped around the grips. The temperature at the sample and each grip was directly measured using thermocouples.

3.4 Microstructural Characterization

Samples for optical microscopy, electron probe microscopy, scanning electron microscopy (SEM), and transmission electron microscopy (TEM) were prepared using mechanical grinding and polishing with successively fine papers up to 1200 grit, followed by a final polishing step with a colloidal silica solution. Furthermore, TEM specimens were prepared by using twinjet polishing on a Struers Tenupol-5, in a 3M H_2SO_4 / alchohol solution maintained at -20°C. Alternate TEM specimens were also prepared using the focused ion beam (FIB) lift-out technique; a Tescan Lyra-3 with a Gallium source was used to prepare thin foils with dimensions of 10x15x1µm, followed by thinning until the foil was transparent to low accelerating voltage (5kV) imaging. SEM imaging was also performed on the Tescan Lyra-3, under both secondary electron (SE) and backscattered electron (BSE) imaging modes. Compositional analysis was performed under electron dispersive spectroscopy (EDS) mode again using the Tescan Lyra-3, as well as wavelength dispersive spectroscopy (WDS) using a Cameca SXFive. Very high resolution compositional analysis was performed using atom probe tomography (APT) using a Cameca 3D Atom Probe. TEM imaging was performed using a FEI Tecnai G2 F20 operating at 200kV.

CHAPTER IV

EFFECT OF PROCESS PARAMETERS ON THE TRANSFORMATION TEMPERATURES AND VARIABILITY OF THE STRESS-FREE SHAPE MEMORY RESPONSE

For successful application of an SMA to an application, it is critical that the material's shape memory response meet the design requirements. For example, biomedical applications often require that the A_s be below body temperature, allowing the device to deploy while it is inside the body. High temperature applications for power generation might require that the M_s temperature be close to the operating temperature of the device, in order to reduce the amount of energy required to cool the SMA for the actuation stroke. In order to consider AM processes as an option for producing SMA parts, it is necessary that the scale of variability in the shape memory behavior be quantified; additionally, should that variability be observed, it becomes necessary that the relationship between process parameters and the variability be understood, in order to control and minimize it. To that end, this chapter focuses on an investigation of the variability of the stress-free shape memory behavior, in particular the transformation temperatures.

It is well known that both part-to-part variability and machine-to-machine are critical issues for AM [4, 110]. In this section, we focus on part-to-part variability; that is, the effect of process parameters on the repeatability of transformation temperatures of multiple parts printed on the same machine. Additionally, it has been observed that the microstructure of the same part can differ from location to location in a single printed part [111], so this is taken into account for the current work.

This chapter is divided into three parts. The first details the process for determination of the process parameter window which was used to form parts free from significant defects. In the second part we examine the stress-free shape memory behavior of successfully built NiTi test coupons using DSC. In the last part we print multiple parts using the same process parameters repeatedly in order to investigate how process parameters affect part-to-part variability.

4.1 Determination of the Process Window

Previous studies had shown that depending on the process parameters, samples with excessive porosity, delamination, or cracks would results. In order to produce fully dense samples free from delamination, 49 10x10x10mm samples were built using varying P, V, and hatch distance. The layer thickness was kept constant at 30µm. Out of the 49 samples, 9 were free of visible cracks, while the rest displayed various defects. Figure 30 shows examples of several of the defective samples.

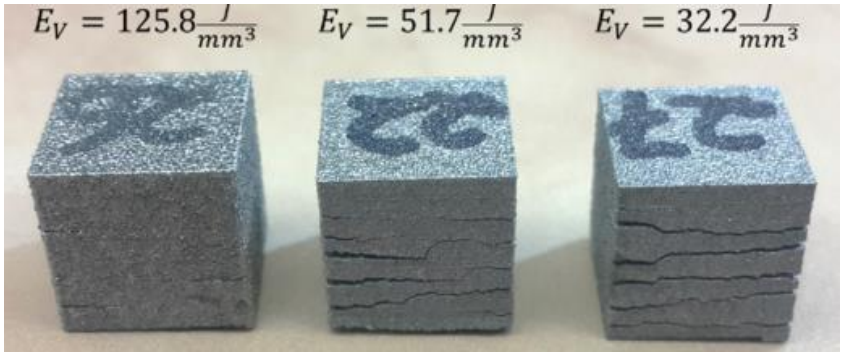

Figure 30: NiTi samples showing cracking and delamination [112].

The laser power was varied between 35-50W, velocity between 70-450 mm/s, and the hatch distance between 35-120µm. The parameter sets are listed in Table 2.

Table 2: Process parameter sets used to build initial samples, with varying laser power, velocity, hatch distance, and calculated energy density. Last column denotes which parameter sets yielded crack free specimens.

Laser Power (W)	Laser Speed (mm/s)	Hatch Distance (μm)	Energy Density (J/mm^3)	Linear Energy Density (J/mm)	Build Success
50	70	120	198.4	0.714	X
35	80	120	121.5	0.438	
50	80	35	595.2	0.625	X
50	80	120	173.6	0.625	X
41	83	95	173.3	0.494	
41	85	40	402.0	0.482	X
49	85	106	181.3	0.576	X
48	89	113	159.1	0.539	X
49	91	47	381.9	0.538	X
45.5	94	68	237.3	0.484	X
41.5	103	55	244.2	0.403	
50	103	116	139.5	0.485	
48.5	109	62	239.2	0.445	X
48.5	110	77	190.9	0.441	
45.5	115	39	338.2	0.396	
44.5	120	96	128.8	0.371	
47.5	122	81	160.2	0.389	
44	131	89	125.8	0.336	
36.5	149	91	89.7	0.245	
37	159	115	67.5	0.233	
43	177	117	69.2	0.243	
41	196	83	84.0	0.209	
38	205	62	99.7	0.185	
40.5	214	70	90.1	0.189	
42.5	223	98	64.8	0.191	
44.5	251	72	82.1	0.177	
45.5	270	119	47.2	0.169	
49.5	279	85	69.6	0.177	
48	288	113	49.2	0.167	
35	297	76	51.7	0.118	
35.5	307	66	58.4	0.116	
36.5	316	42	91.7	0.116	
45	325	53	87.1	0.138	
39.5	334	102	38.6	0.118	
48.5	353	79	58.0	0.137	
47	362	104	41.6	0.130	
36	371	96	33.7	0.097	
48.5	381	59	71.9	0.127	
39	390	64	52.1	0.100	
46	399	51	75.4	0.115	
44	418	106	33.1	0.105	
43.5	427	49	69.3	0.102	
42	436	57	56.3	0.096	
40	445	93	32.2	0.090	
35	450	35	74.1	0.078	
35	450	120	21.6	0.078	
50	450	35	105.8	0.111	
50	450	120	30.9	0.111	

By varying the P, V, and hatch distance, the volumetric energy density varied between 21.6 and 595.2 J/mm^3, and the linear energy density varied between 0.714 and 0.078 J/mm. Figure 31shows a 3d plot in the laser power, velocity, and hatch distance space. Red markers denote successful builds, while black markers denote failed builds.

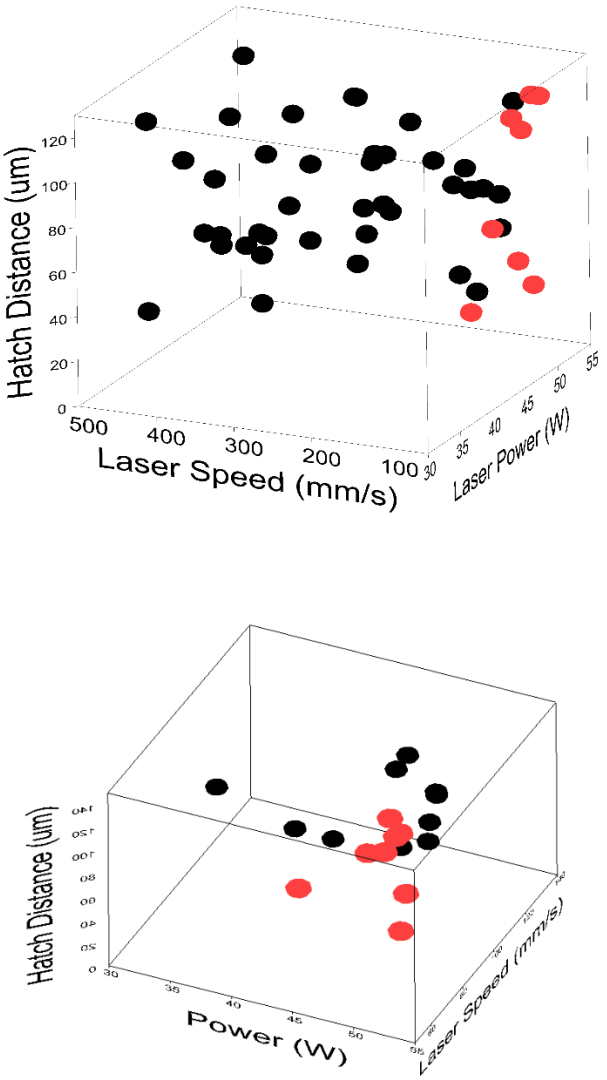

Figure 31: 3D plot of laser power, velocity, and hatch distance showing success or failure of builds, with red markers denoting success. Top: full space, Bottom: Velocity below 140 mm/s.

The figure shows that successful builds were clustered towards the low V region of the plot; the highest V parameter setting that produced successful builds was 109 mm/s. By expanding the low V region, it can be seen that success region is clustered towards the high P, low V, low hatch distance region of the plot. Successful builds were observed in the volumetric energy density range between 159-595 J/mm^3, and in the linear energy density range between 0.445-0.714 J/mm; however, in both cases there were specimens inside the success ranges that exhibited cracking. This reiterates earlier findings that it is necessary to consider all of the process parameters alongside the energy densities. In several cases, the volumetric and linear energy densities were high due to the small hatch distance and low V; however, the P was low enough that the melt tracks were not continuous, leading to poor density. For a more in-depth discussion of the buildability of NiTi, please see Mahmoudi et. al [112].

4.2 DSC Experiments

DSC specimens were removed using EDM from the center of the successful 10x10x10mm cubes printed in the previous section. Samples were cycled between -80 to 150°C to avoid first cycle affects, which would give erroneous measurements for the true transformation temperatures of the printed material. Figure 32 shows the DSC curves for the successful builds, sorted by linear energy density. It can be seen from the figure that there are two types of curves; several curves have sharper, narrow transformation peaks, while others have broader, gradual transformation peaks. This confirms the earlier observations by Speirs et. al [33]. Several of the curves exhibit a secondary, minor peak near 60°C. This is likely to correspond to the R-phase transformation, which occurs when the matrix contains Ni_4Ti_3 precipitates.

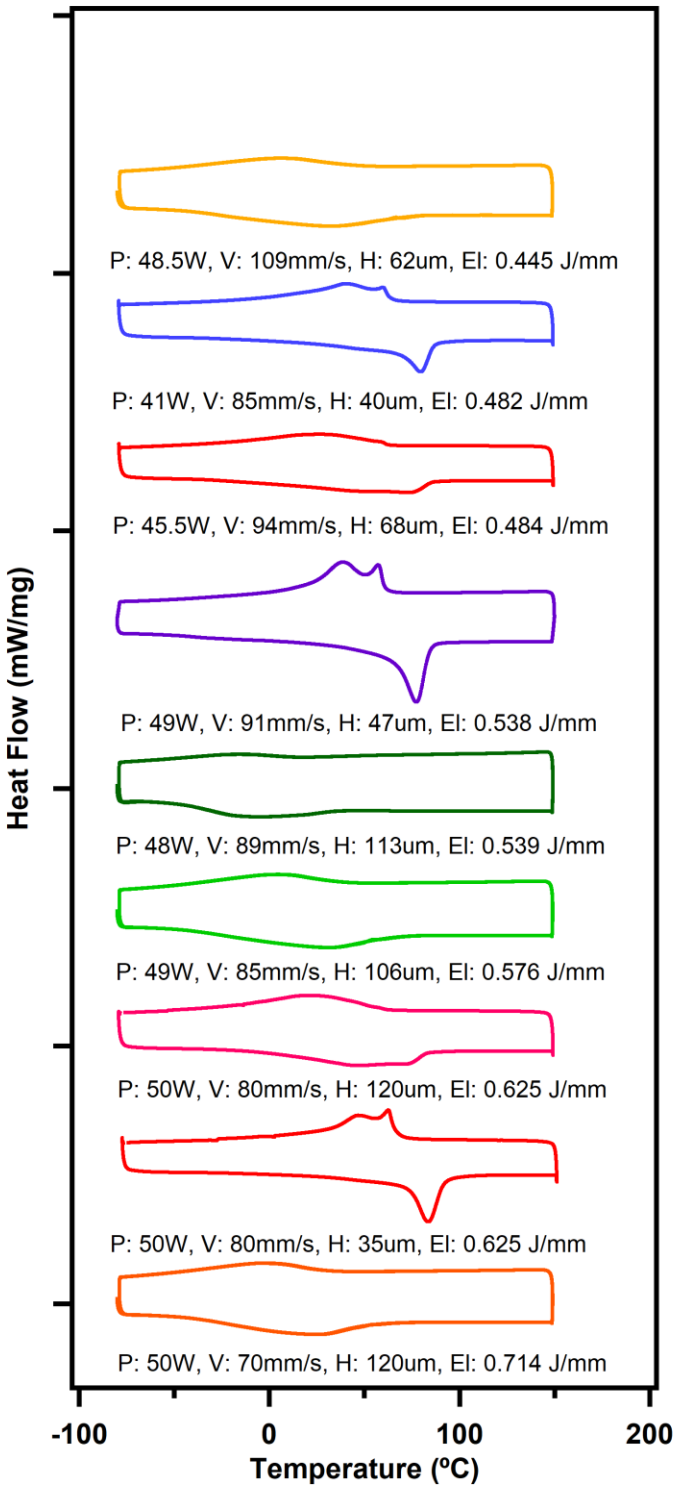

Figure 32: DSC results for the successful builds, in order of linear energy density.

Table 3 shows the measured transformation temperatures, thermal hysteresis, and breadth of the martensite and austenite transformation intervals as well as the linear and volumetric energy density and the hatch distance. It can be seen that the transformation temperatures do vary greatly depending on the process parameters; the M_s ranges between 12 and 64°C, the M_f between -65 and 25°C, the A_s between -51 and 69°C, and the A_f between 31 and 90°C. The hysteresis does not change appreciably; it ranges between 19 to 26°C. The interval of the martensite peak ($M_s - M_f$) ranges between 39 to 114°C, and the interval of the austenite peak ($A_f - A_s$) ranges between 21 to 126°C.

Table 3: Transformation temperatures measured for the 9 successful samples, as well as the calculated hysteresis, the martensite interval, and the austenite interval.

E_l J/mm	E_v J/mm^3	Hatch Distance	M_s °C	M_f °C	A_s °C	A_f °C	Hyst °C	M_{int} °C	A_{int} °C
0.539	159.1	113	12	-65	-48	31	19	77	79
0.625	173.6	120	62	-34	-4	82	20	96	86
0.576	181.3	106	39	-69	-49	64	25	108	113
0.714	198.4	120	34	-64	-47	57	23	98	104
0.484	237.3	68	64	-23	-28	85	21	87	113
0.445	239.2	62	47	-67	-51	75	28	114	126
0.538	381.9	47	61	18	62	85	24	43	23
0.482	402	40	63	0	66	86	23	63	20
0.625	595.2	35	64	25	69	90	26	39	21

The very large shifts in transformation temperatures indicate that significant changes in microstructure or composition are occurring during the processing. According to the M_s temperature-Ni content relation, a shift of 120°C occurs when the composition changes from 50.9 at% NiTi to 50.0 at% NiTi [43]. It is interesting to note that the hysteresis does not change appreciably despite the process parameters used. Figure 33 shows the effect of volumetric energy density on M_s temperature, A_s temperature, and the hysteresis. It can be seen that at low

volumetric energy densities the transformation temperatures are low, and increase with the volumetric energy density. However, from energy density of 240 J/mm^3 and higher the transformation temperatures remain relatively constant.

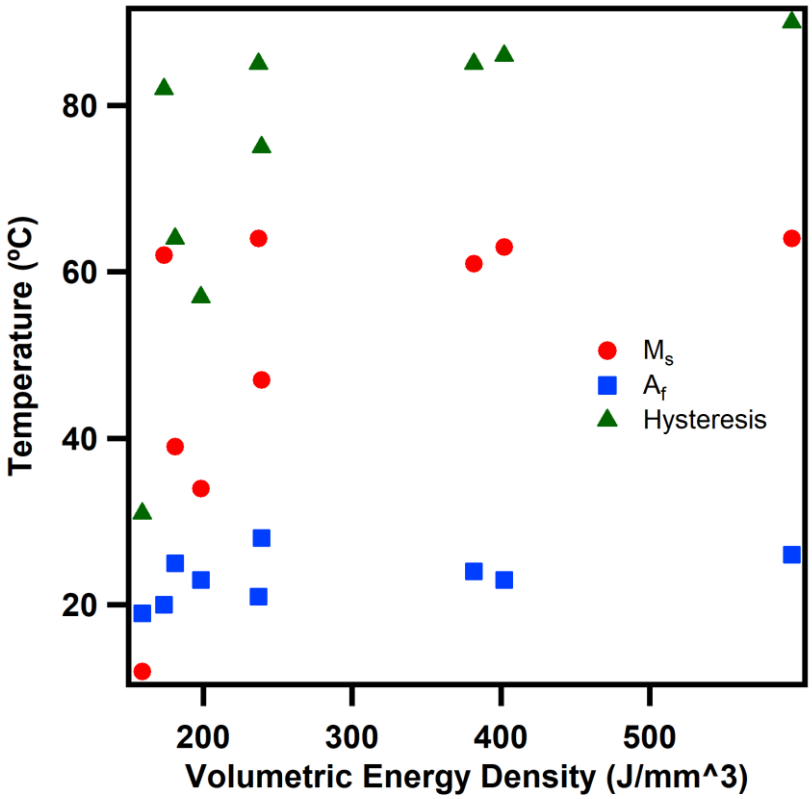

Figure 33: Effect of volumetric energy density on M_s, A_f, and hysteresis.

The intervals for both the austenite-martensite and martensite-austenite transformations did not correlate to either the linear energy density or the volumetric energy density. Instead, the parameter that influenced the intervals most strongly was the hatch distance. Figure 34 shows the DSC curves grouped by hatch distance. The curves where the corresponding hatch distance was below 47µm resulted in transformation intervals smaller than 63°C, while those with hatch distances above 62µm resulted in transformation intervals larger than 77°C. This indicates that

hatch distance is a critical parameter for controlling the width of the transformation peaks. Additionally, there is a hatch distance parameter above which wide transformations occur, and this critical hatch distance is between 50-60μm.

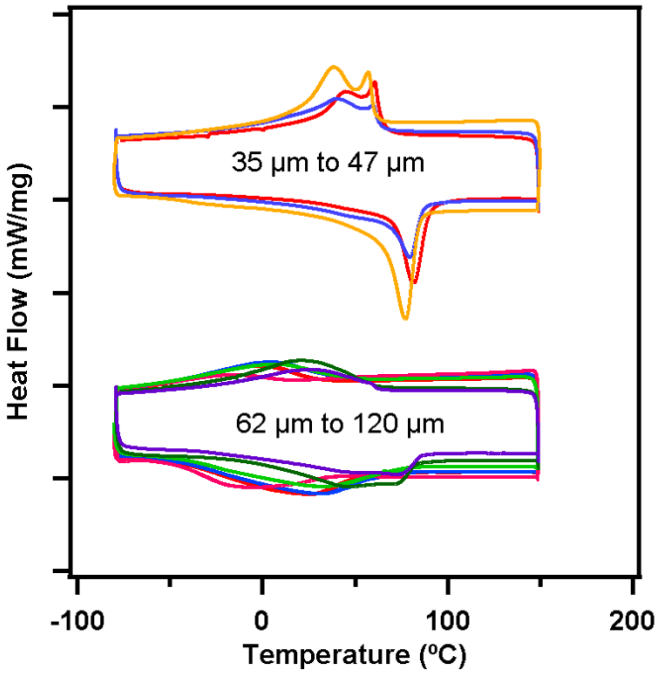

Figure 34: Wide and narrow transformation peak DSC curves grouped by hatch distance [58].

4.3 Variability in the Stress-Free Shape Memory Response

The types of variability in SLM-built parts that we investigate in the current work can be organized into three different categories. These are summarized below:

- Localized variability: variation in properties, microstructure, or composition on the scale of the melt pool (hundreds of microns)
- Part variability: variation on the scale of a single constructed part (millimeters)
- Part-to-part variability: variation that occurs when parts are built using the same processing parameters, machine conditions, powder, and geometry.

Machine-to-machine variability can also occur between different models and manufacturers, and has been previously observed, but is not considered in this work.

The first category of variability, the localized variability, can be seen in the broad peaks discussed in the previous section. To examine this, we focus on the DSC response for two specimens that were printed using the same P and V, but different hatch distances. Since the hatch distance was observed to be the most critical parameter for determining peak width, this allows us to separate the effect of the size of melt pool geometry (which changes due to P and V), and focus solely on the effect of hatch distance on variability. The two selected process parameter sets are listed in Table 4. Note that these parameter sets have identical linear energy density, but very different volumetric energy density. These will be referred to by H35 and H120, according to the corresponding hatch distances of 35μm and 120μm.

Table 4: Selected parameter sets for further study of variability

Sample Name	Laser Power (W)	Laser Speed (mm/s)	Hatch Distance (μm)	Energy Density (J/mm^3)	Linear Energy Density (J/mm)
H35	50	80	35	595.2	0.625
H120	50	80	120	173.6	0.625

The linear energy density of both the H35 and H120 samples is 0.625 J/mm, while the H35 sample has an energy density of 595.2 J/mm^3, and the H120 sample has an energy density of 173.6 J/mm^3. Figure 35 shows a comparison of the H35 and H120 specimens to a sample of the virgin powder used to build the specimens. The virgin powder did not exhibit shape memory transformation before heat treatment.

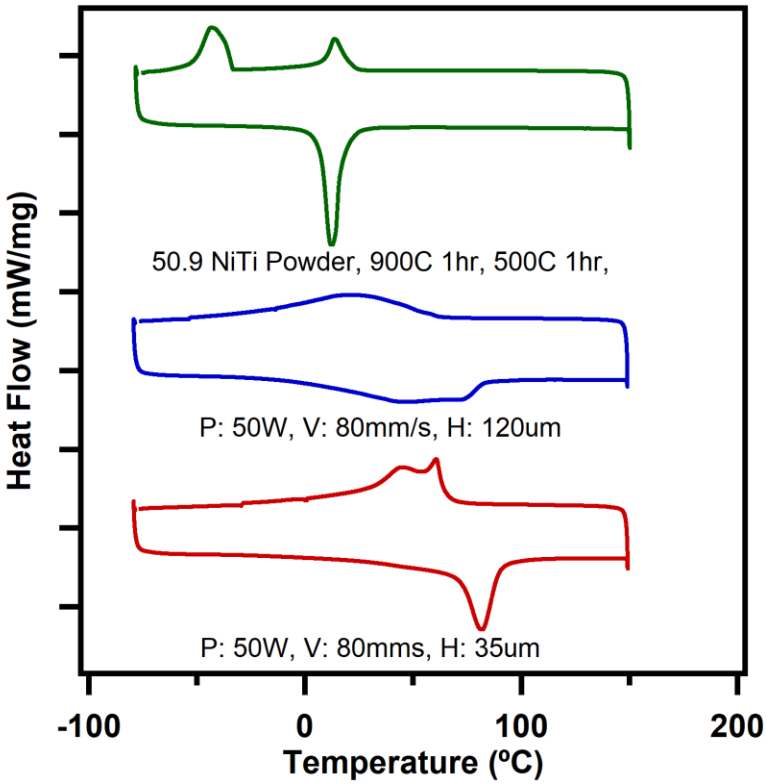

Figure 35: Comparison of DSC curves of the H35 and H120 samples to solution and heat treated powder.

The solution treated and heat treated powder exhibits a DSC curve characteristic of a conventional Ni-rich alloy that has been precipitate heat treated. Note the additional minor peak during the reverse transformation that corresponds to the R-phase transformation, and is indicative of the formation of Ni-rich precipitates. The R-phase peak corresponds to the B2 austenite to R-phase transformation, the second, larger peak during cooling corresponds to the R-phase to B19' transformation, and the single peak during heating corresponds to the B19'-B2 transformation. The breadth of the austenite transformation peak is 14°C, and the breadth of the martensite transformation peak is 17°C. This contrasts greatly with the transformation peaks of the wide hatch distance H120 specimen, which had an austenite transformation peak width of

86°C, and a martensite transformation peak width of 96°C. The narrow hatch distance H35 specimen had an austenite transformation peak width of 21°C, and a martensite transformation peak width of 39°C. The peak widths for the powder are similar to those of conventional materials and indicate that the material is mostly homogenous; the greater part of the matrix transforms at the same temperature since the local compositional and microstructural differences are in the nanoscale. The H120 sample, however, has transformation peaks which are of an order of magnitude greater. This indicates local compositional and/or microstructural differences that are at least smaller than the size of the DSC specimen, 3mm by 1mm. The broad transformation peaks indicate this inhomogeneity because it means that different local regions of the matrix are transforming at different temperatures, and in NiTi these transformation temperatures are dictated by composition or microstructure. The H35 sample has transformation peaks that are slightly wider than the powder specimen, but still much narrower than the H120 sample. Again, this indicates that the H35 sample exhibits homogeneity of composition and microstructure, due to the fact that different local regions of the matrix are transforming at the same temperature.

Since we observed the first category of variability, we move on the second kind; the part variability. This means detection of differences in transformation temperature for different locations of a single part. Previous works in DED and EBM have indicated that part variability occurs as a matter of height along the vertical axis of the part [111, 113], so specimens were taken from the top, middle, and bottom of the central vertical axis of both the H35 and H120 samples. A schematic showing the locations of the specimens is shown in Figure 36. The specimens were cut as a 3mm cylinder from the center, then 1mm thick discs were then cut from locations on the vertical axis centering on 0.5mm, 5mm, and 9.5mm.

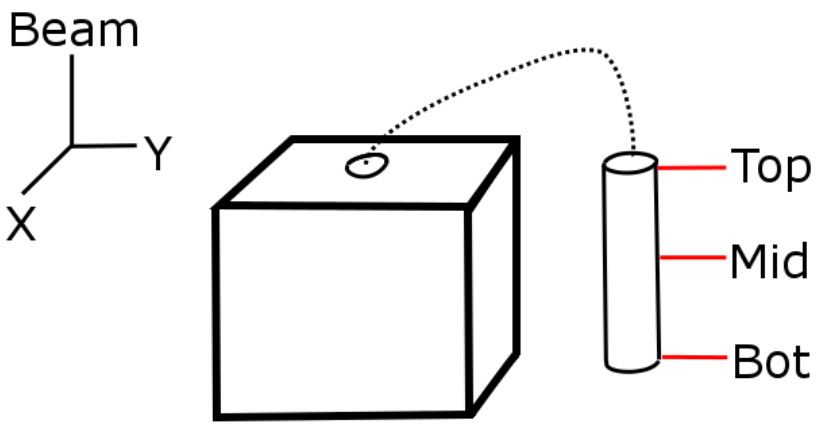

Figure 36: Location of the 3 specimens taken from the H35 and H120 samples to investigate part variability.

The results of the DSC experiments of the 3 locational specimens for the H35 and H120 samples are shown in Figure 36. It was observed that both for both the H35 and H120 conditions, all of location dependent specimens exhibited the same transformation peak width behavior regardless of location. Additionally, the DSC curves were nearly identical regardless of specimen location. The DSC curves for the location dependent specimens are shown in Figure 37, and the measured transformation temperatures are shown in Table 5.

Table 5: Transformation temperatures for location-dependent specimens taken from H35 and H120 samples.

Sample	M_s	M_f	A_s	A_f
H35 bot	64	26	70	90
H35 mid	64	29	69	90
H35 top	64	29	70	89
H120 Bot	61	-15	0	81
H120 mid	62	-14	-1	83
H120 top	63	-14	-3	83

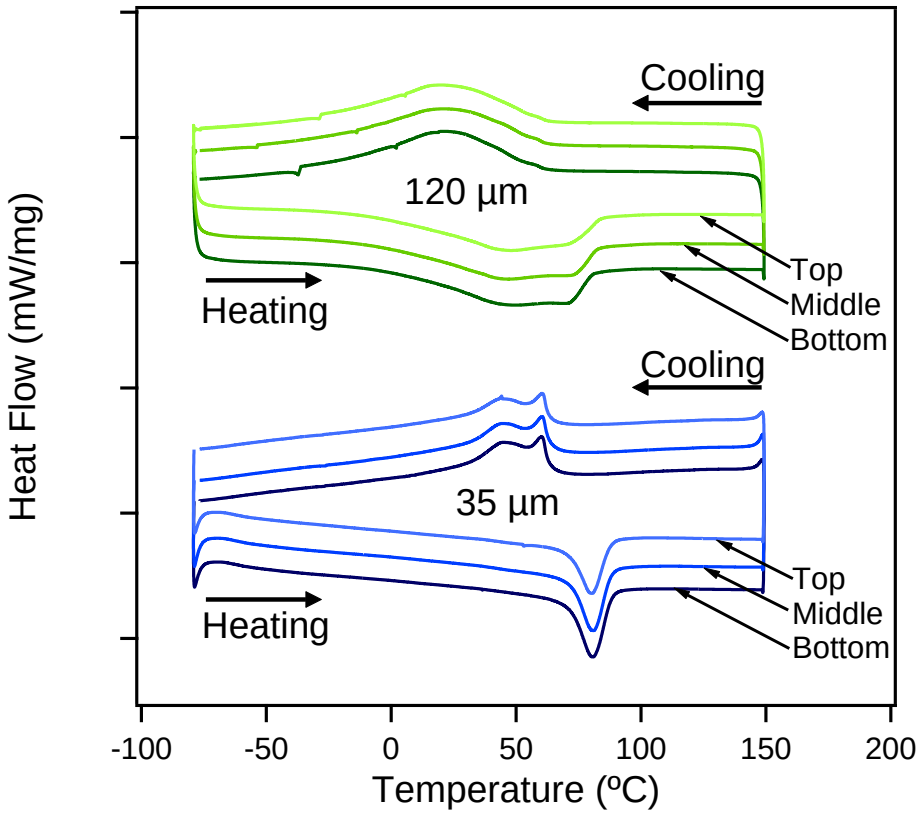

Figure 37: DSC results for specimens taken from top, middle, and bottom of H35 and H120 samples [58].

The transformation temperatures for the location dependent specimens were extremely consistent. For the H35 samples, the largest variation in transformation temperature was 3°C for the M_f temperature. For the H120 samples, the largest difference was 3°C for the A_s temperature. Despite the localized variability (micron scale) in the H120 samples, it was observed that no part variability (mm scale) existed.

To address the part-to-part variability (repeatability), multiple specimens using the H35 and H120 process parameters were built. Two additional cube 10x10x10mm samples were made. In order to observe if part geometry also affected the variability, 5 cylindrical hoops with a diameter of 25.4mm, a thickness of 1mm, and a height of 10mm were built using both H35 and

H120 sets. Finally, two sets each of 1mm thick, 5mm high, 30mm long beams were built. The resulting DSC curves are shown in Figure 38.

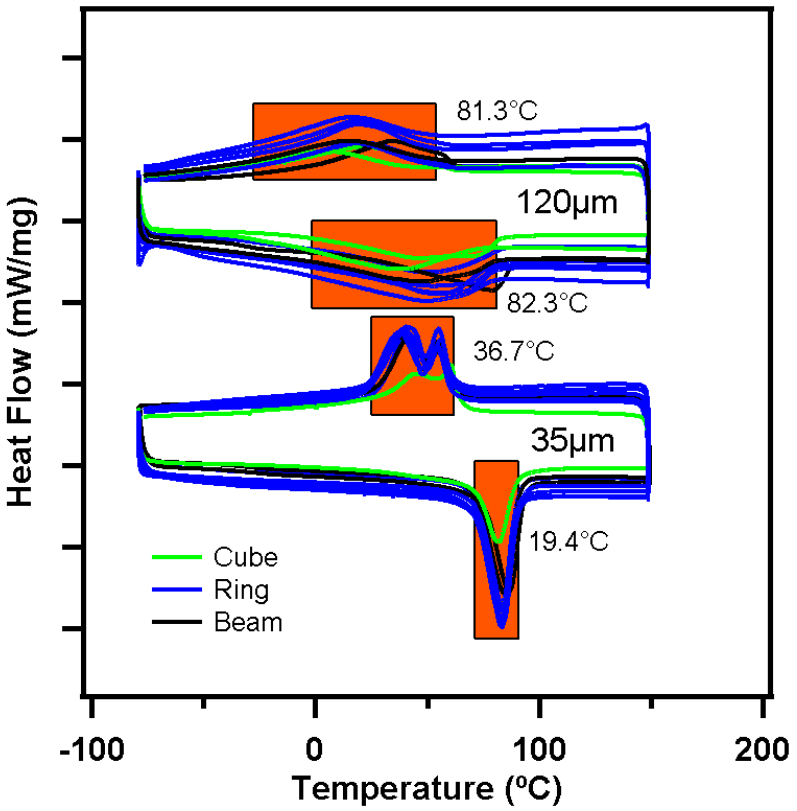

Figure 38: DSC curves for the H35 and H120 assorted cube, ring, and beam shapes. The breadth of the transformation peaks is highlighted in orange [58].

It can be seen from the DSC curves that the H35 specimens are very consistent with regards to the transformation temperatures. Each curve approximately mirrors each of the others. There is a slight difference considering the cube specimens; the enthalpy of transformation (the area under the peak) is slightly smaller for the cubes rather than the other specimens. This may possibly be due to the cube samples being much larger in volume than the ring or beam shapes, and since the H35 parameter set has a high energy density of 595.2 J/mm^3, this may mean that the cubes were exposed to higher levels of oxygen contamination during the process. The H120 specimens show

significantly higher scatter with regards the transformation curves. The peaks shift up and down on the temperature axis, and it can be seen that the height of the peaks varies as well. The transformation temperatures measured from the DSC experiments performed on the repeated H35 and H120 specimens are shown in Figure 39.

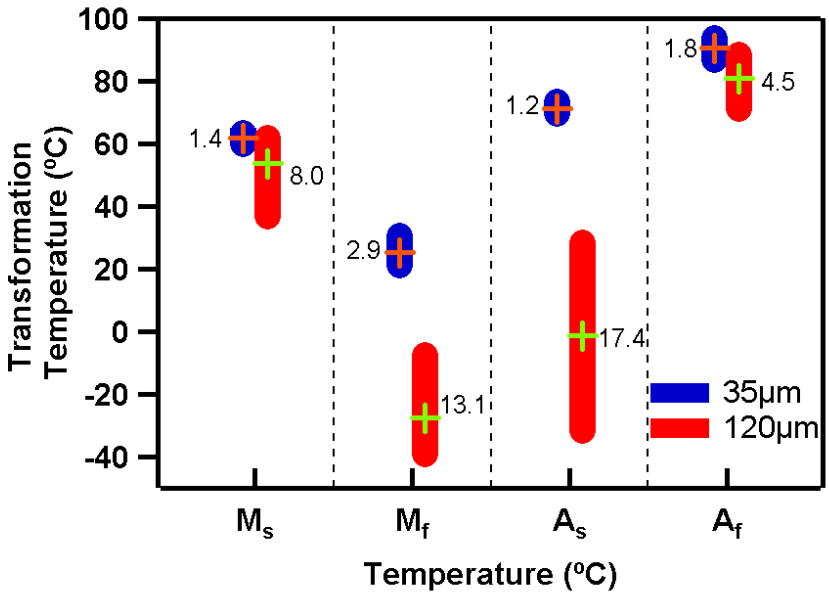

Figure 39: Range, average, and standard deviation of the four transformation temperatures for all H35 and H120 samples. The vertical bars represent the range of measured values, the markers represent the average value, and the number next to each bar is the standard deviation [58].

First, regarding the average values of the transformation temperatures. The average of the M_s and A_f temperatures were relatively close for the H35 and H120 specimens. The difference in M_s between H35 and H120 was 8.1°C, and the difference in A_f between H35 and H120 was 9.8°C. The difference in the M_f and A_s temperatures was much more markedly pronounced. The difference in M_f temperature between H35 and H120 was 52.7°C, and the difference in A_s temperature was 72.7°C.

The variation in transformation temperatures was much larger for the H120 specimens than for the H35 specimens. From the figure, it can be seen that the range of transformation temperatures for H120 was larger for each transformation temperature when compared to H35. The biggest range was for the H120 A_s temperature, followed by the M_s and M_f temperatures. For the H35 specimens, the M_f range was slightly larger than the A_s, A_f, and M_s temperatures. The standard deviation values followed similar trends. All of the standard deviations for the H120 specimens were larger than those for H35. The largest standard deviation for the H120 specimens was the A_s temperature, at 17.4°C, followed by the M_f temperature, at 13.1°C, then the M_s temperature, at 8.0°C, and finally the A_f temperature, at 4.5°C. The largest standard deviation for the H35 specimens was the M_f temperature, at 2.9°C, followed by the A_f temperature, at 1.8°C, then the M_s temperature, at 1.4°C, and finally the A_s temperature, at 1.2°C.

In 2004, Sczerzenie performed a study of variability in transformation temperatures for various conventionally processed NiTi products made by the Special Metals Corporation [65]. In that study, the transformation temperatures were measured in two different categories; in the first, large numbers of samples from an individual heat of solution treated NiTi were measured. In the second, the transformation temperatures were measured from four different processes, including material from different heats. Here, we will compare the results of the SLM-built NiTi specimens against both categories. However, it should be noted that the most comparable case is the first category, since the SLM-built NiTi was made using the same powder in the same equipment. The study of different processes and heats is more comparable to a SLM study wherein different batches of powder and different equipment has been included. The processes included vacuum induction melting, vacuum arc melting, redrawn coil, and wire. The

comparisons can be seen in Table 6. In comparison to the most comparable case, that of the air-cooled and water-quenched wire from a single heat, the H35 and H120 specimens showed higher standard deviations. The wire standard deviations were all under 0.6°C, while the smallest H35 standard deviation was 1.4°C and the smallest H120 standard deviation was 4.5°C. In comparison to the multiple-process, multiple-heat standard deviations, the H35 exhibited similar levels of variability while the H120 standard deviations exceeded them. So, the H35 specimens exhibited variation in transformation temperatures slightly higher than wire from a single heat, but similar to multiple-process, multiple-heat material. The H120 specimens exhibited variability far greater than both the single heat wire, and the multiple-process, multiple-heat material.

Table 6: Standard deviations for H35 and H120 specimens from the current work, as well as various conditions from literature. * Denotes values taken from literature. AC and WQ correspond to air cooled and water quenched NiTi wire from the same heat. 0 and 75 correspond to multiple-process, multiple-heat experiments where 0 and 95 were the desired A_s temperature of the material [65].

Condition	M_s	M_f	A_s	A_f
H35	1.4	2.9	1.2	1.8
H120	8	13.1	17.4	4.5
*AC	0.3	0.6	0.2	0.5
*WQ	0.3	0.6	0.2	0.3
*0	3.5	7.7	2.4	4.8
*95	1.6	2.4	1.7	2.7

4.4 Summary of main findings

In this section, the variability of the transformation temperatures of SLM-built NiTi was investigated. It was found that depending on the process parameters, samples exhibited wide or narrow transformation peaks, where wide transformation peaks were associated with localized variability due to inhomogeneity in composition or microstructure. The process parameter most

strongly correlated with the peak width was the hatch distance. Samples built using hatch distances below 47μm exhibited broad peaks, while those built with hatch distances above 62μm exhibited narrow peaks. There is a critical value for the formation of broad or narrow peaks, and this is in the range of 50-60μm. The observation of the wide peaks confirmed the existence of localized, micron scale variability. Furthermore, specimens were taken from different locations (relative to the vertical height) of two specimens of the H35 and H120 process parameter sets, corresponding to narrow and wide transformation peaks respectively. It was found that regardless of location, the DSC curves were very similar for all of the H35 and for all of the H120 samples. This observation indicated that part variability (on the mm scale) was negligible. Finally, specimens of the H35 and H120 were repeatedly built using different geometries. It was found that the H120 specimens showed higher standard deviations than the H35 specimens, and that H120 specimens exceeded the variability of conventional NiTi products, while H35 was comparable to conventional NiTi products. This indicates that part-to-part variability occurs in NiTi samples with broad peaks, and can be controlled by proper selection of the hatch distance.

CHAPTER V

MICROSTRUCTURAL INVESTIGATION OF THE CAUSES OF VARIABILITY IN THE SHAPE MEMORY RESPONSE

In the previous section, it was found that localized, micron scale variability as well as part-to-part variability could result in during SLM processing of NiTi. Additionally, it was found that the variability was controlled by the hatch distance process parameter. The observation of broad transformation peaks indicated that some inhomogeneity and variation in the composition or microstructure was occurring; however, from DSC experiments alone the specific mechanisms could not be identified.

In this section, a wide range of multiscale compositional and microstructural investigations will be presented. The key goal is to go through each of the possible mechanisms that can affect the transformation temperatures in NiTi and present evidence that either inhomogeneity exists or does not in the H35 and H120 specimens. These specimens are chosen because the H35 exhibits homogenous martensitic transformation, while the H120 exhibits inhomogenous transformation. The possible mechanisms for changes in martensitic transformation temperatures in NiTi are summarized below:

- Composition
- Precipitate formation
- Dislocation density
- Grain Size
- Stress

5.1 Investigation of Compositional Variability

Using WDS, the average composition of the material was measured through each step of the process; from billet, to gas atomization of powder, and finally to SLM processed parts. Table 7 shows the composition measurement values as well as the standard deviation.

Table 7: Composition measured by WDS of material throughout the processing history.

Sample	Ni Content (at%)	Standard Dev. (at%)
50.9 at% Billet	50.08	0.08
Gas Atomized Powder	49.96	0.39
H35 specimen	47.95	0.91
H120 specimen	49.09	0.40
50.0 at% comparison	48.87	0.13

Before discussing these results there are several things that must be noted. First, the values were obtained by taking a large number of measurements across 20 different locations across each sample. This means that the measured values are not indicative of local variation, but simply an average overall value. Secondly, there is an inherent bias error when taking WDS measurements. This means that while the differences between the different measurements is precise, they all differ from the true value by the same amount. This can be seen by the measurement of the 50.0 at% NiTi equiatomic material; the measurement from this material gives 48.87 at% Ni. This means that the bias error is near 1.13 at%. This can also be seen from the 50.9 at% NiTi billet measurement, which measures 50.08 at% Ni.

After gas atomization, the material loses a negligible amount of Ni, 0.12 at%. This difference is within the range of a standard deviation, so is likely not significant. However, after the SLM process it can be seen that a significant amount of Ni loss occurs, depending on the hatch distance. For the H35 sample there was a loss of 2.01 at% Ni, and for the H120 sample there was a loss of 0.87 at% Ni. The final Ni contents were 47.95 at% Ni for H35, and 49.09 at% for H120. The higher overall Ni loss for H35 is due to the much higher volumetric energy density when using that parameter set, with 595 J/mm^3, in comparison to the H120 which had a volumetric energy density of 174 J/mm^3. The standard deviation of the powder material, and both the H35 and H120 samples was higher than those of the two billet materials. This indicates that some measure of compositional variability occurs during the gas atomization process, and through the SLM process as well.

In order to determine the localized variability, we first performed SEM secondary electron imaging to examine the geometries of the melt tracks. The SEM images are shown in Figure 40. The SEM images are taken from the top surface (X-Y) plane of the 10x10x10mm cubes. For the H120 sample, the effect of the laser rastering across the surface from the top and bottom of the image are visible. Several melt tracks are highlighted in the image. By examining the final melt track, it can be seen that the melt pool is approximately 160μm in diameter. The melt pool diameter for the H35 samples is exactly the same, since both samples have the same P and V process parameters. The only difference between the two is the degree of overlapping of the melt tracks. For the H120 sample, two adjacent melt tracks are highlighted, and the overlap zone is shown. For the H35 sample, the overlap is much greater, since the center of each track is only 35μm apart.

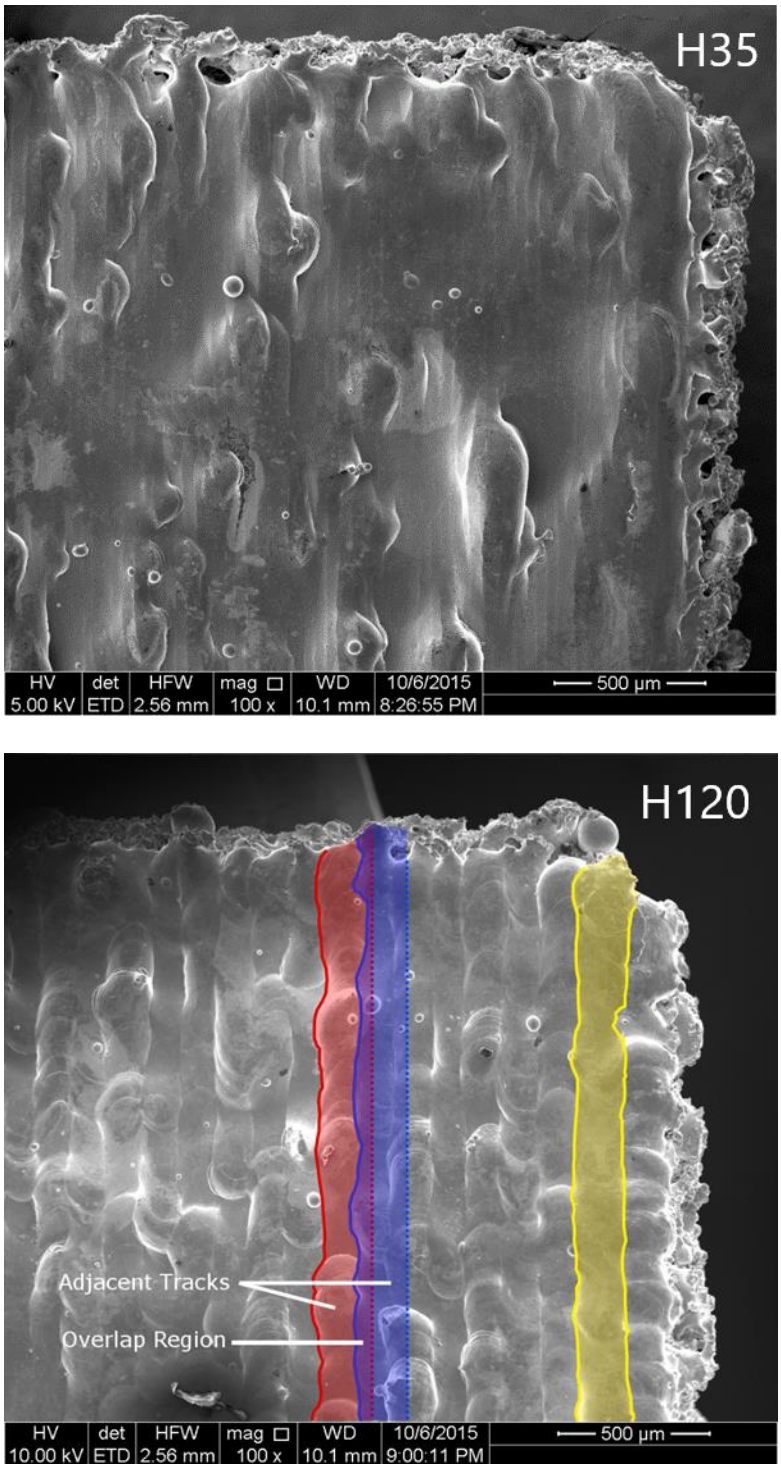

Figure 40: SEM images showing the top surfaces of the H35 and H120. The images show the top X-Y surface. For the H120 image it can be seen that the melt pool is around 160µm in diameter [58].

Figure 41 shows a schematic for the cross section of the melt pools in the X-Z plane, perpendicular to the surfaces shown in the previous SEM images. The melt pools are represented by the roughly lenticular shapes. For the H120 specimens it can be seen that since the melt tracks are 120µm apart, and the melt pools are 160µm in diameter, there is an overlap region between adjacent melt pools of 40µm, and a single melted region of 80µm. However, for the H35 specimens each point in the material is remelted 7 times.

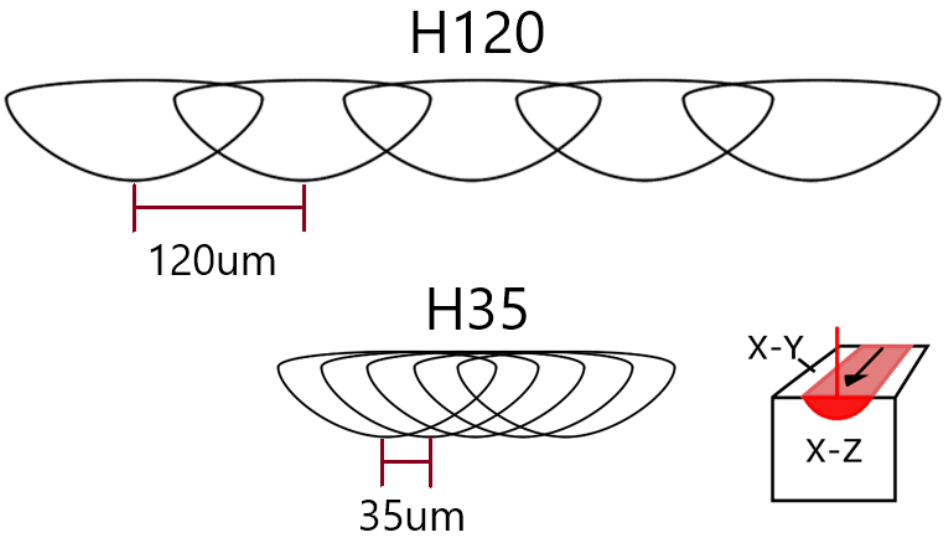

Figure 41: Schematic of the cross section in the X-Z plane of the melt tracks for H120 and H35.

The melt pool cross sections can be seen by cutting the cubes in half vertically in the X-Z plane, polishing the surface, etching, and then imaging using an SEM secondary electron detector. Figure 42 shows the polished and etched X-Z plane of the center of the H35 cube. After etching, individual layers of the build can be observed. The waviness of these layers attests to the stochastic nature of the thermal process. Several micro-pores can also be seen. The rectangular holes are the result of FIB sample preparation.

Figure 42: Polished and etched X-Z plane of the H35 cube. Individual X-Y layers, as well as single melt tracks can be seen.

Figure 43 shows the polished and etched X-Y plane of the H120 cube. In this case, the individual layers are less visible. It can be seen that individual melt tracks are also less visible, and more separated than in the H35 case.

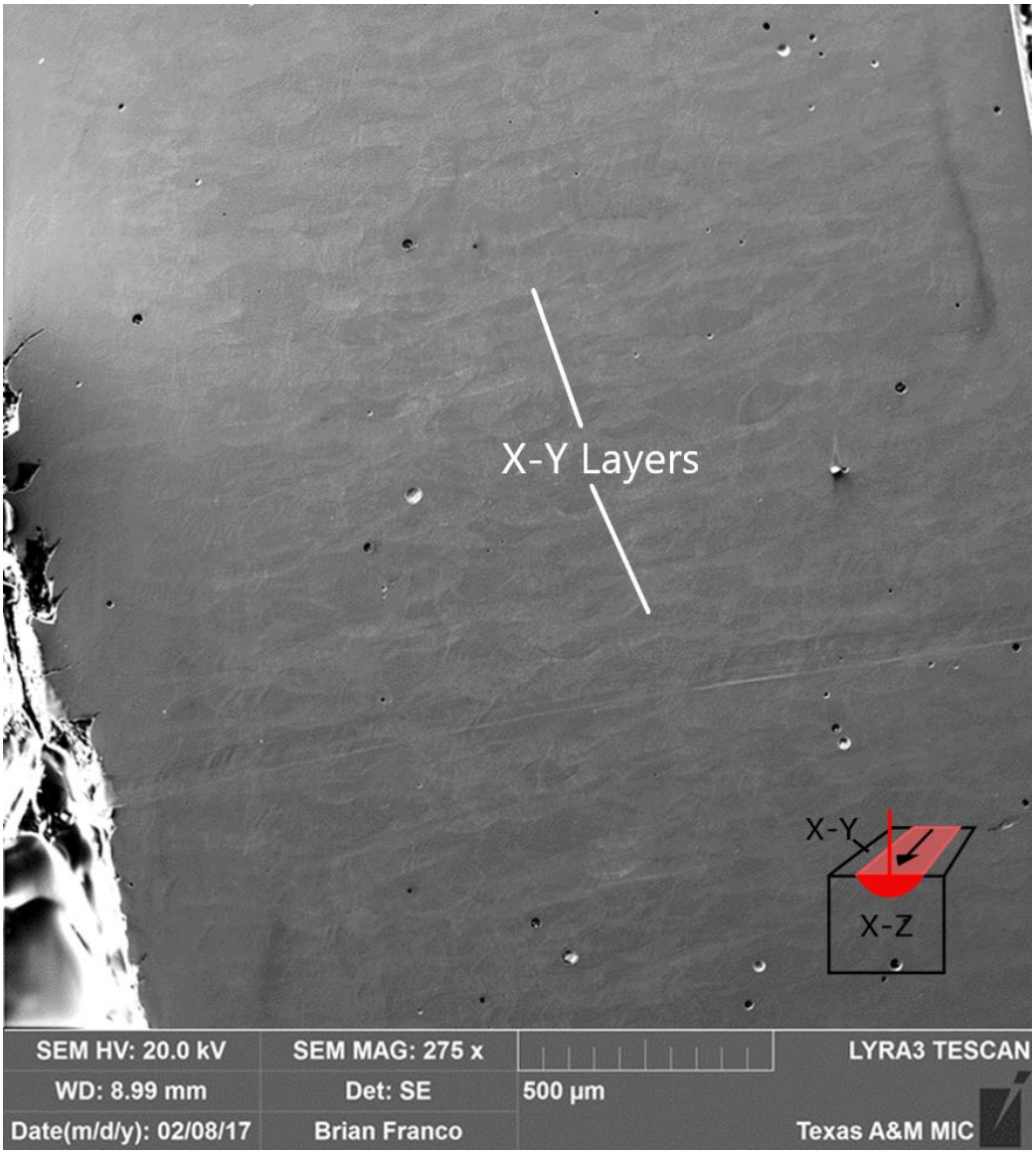

Figure 44: Polished and etched X-Z plane of the H120 cube. The layers and melt pools are less prevalent than the H35 sample, but can still be seen.

On higher magnification, the individual melt pool boundaries are more easily discernible. Figure 45 shows the high magnification SEM image of the X-Z plane for H35. At this higher magnification the subgrain structure of the matrix can be more clearly seen. Subgrain structures have been previously reported in the literature for SLM-built NiTi [36].

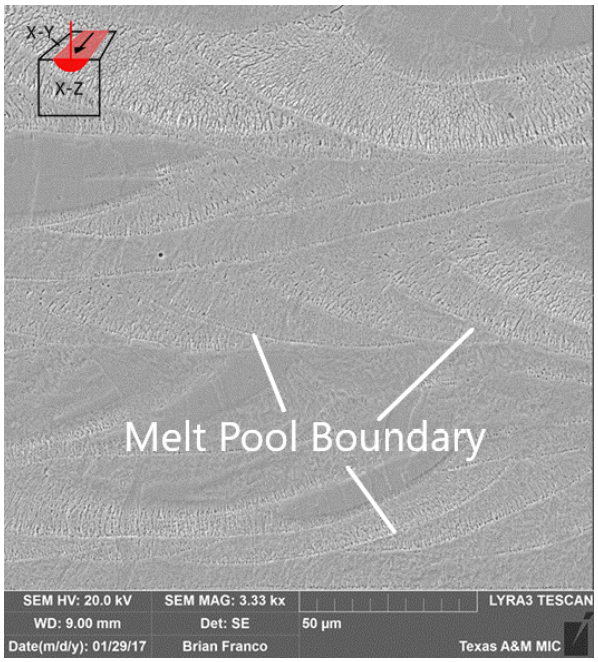

Figure 45: High magnification SEM image of the X-Z plane of H35 sample, showing the melt pool boundaries in higher detail.

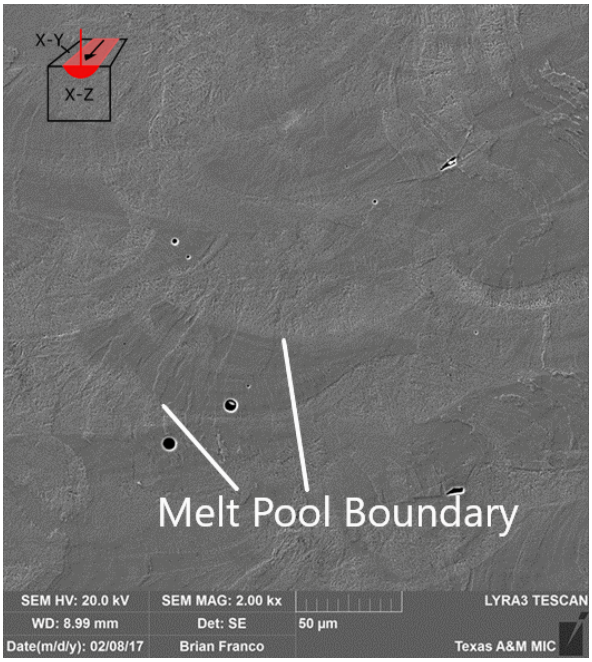

Figure 46: High magnification SEM image of the X-Z plane of the H120 sample, showing the melt pool boundaries in higher detail.

Figure 46 shows the high magnification image of the H120 sample. Again, the melt pool boundaries are less discernable than the H35 sample, and the cell structures are barely visible.

Since it was possible to observe the morphology of the melt tracks, the next step was to determine if compositional gradients could be detected across the melt pools. It was expected that such compositional difference would occur due to the high thermal gradient between the center and the edge of the melt pools, as well as due to the difference in thermal history between remelted regions and single melted regions. Figure 47 shows the results of EDS line and area compositional scans.

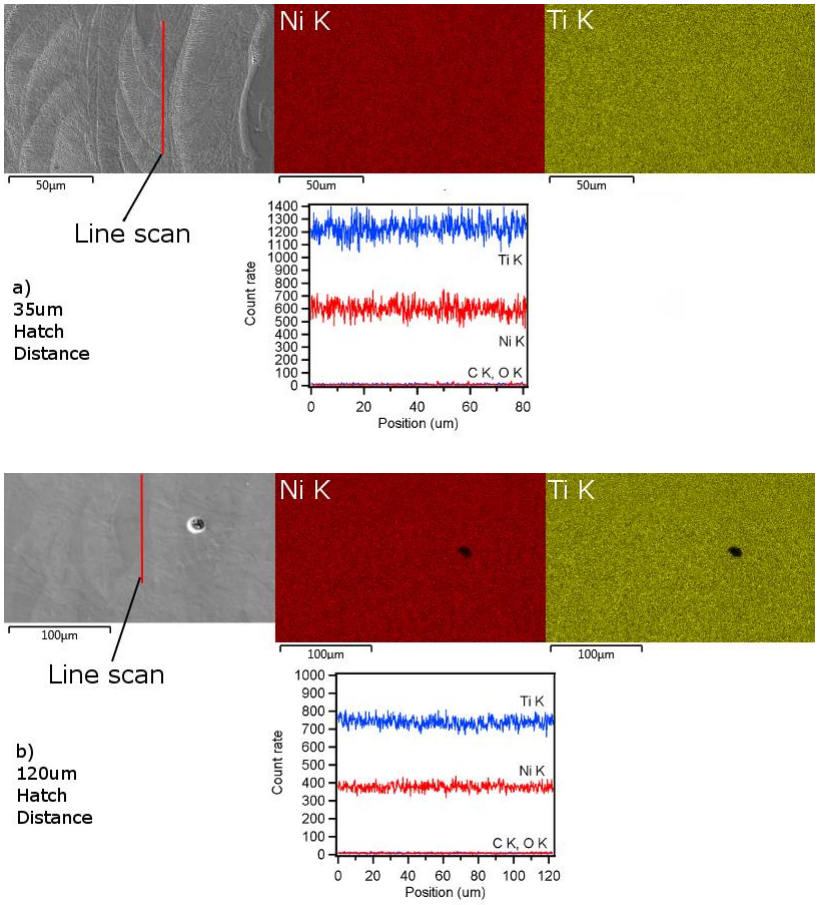

Figure 47: EDS line and area scans for a) H35 and b) H120.

The EDS line and area scans showed no composition gradients across individual melt pools, or in the general area of the melt pools. However, since the spot size of the EDS beam was on the order of 10μm, it was likely that the compositional differences were being averaged together if they were fine in scale.

To that end, WDS analysis was performed using a much finer spot size. Area maps were constructed in a 256x256 pixel grid, with each pixel corresponding to a 2μm square. The resulting WDS maps are shown in Figure 48.

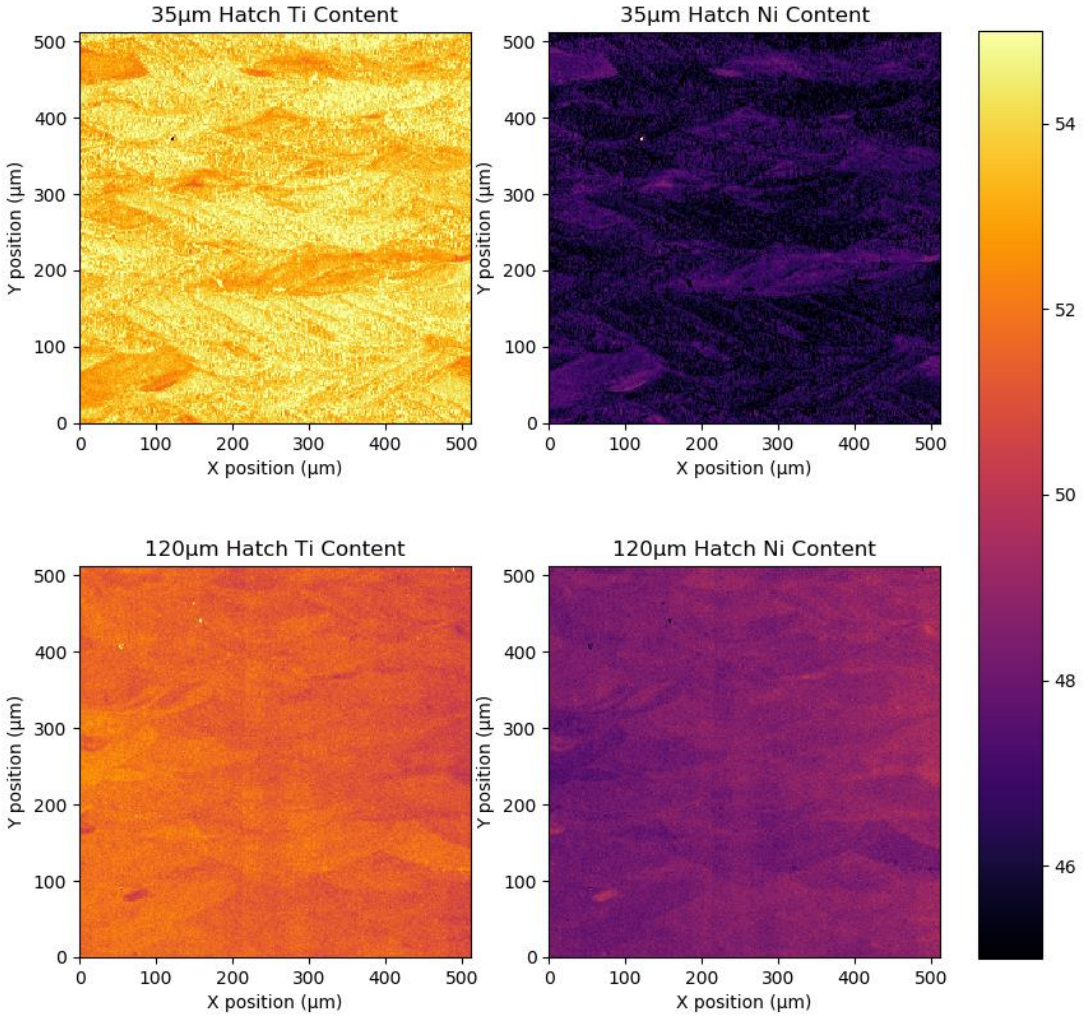

Figure 48: WDS area maps for Ni and Ti at% for the H35 and H120 samples.

It can be seen from the figure that composition gradients are in fact observed for both the H35 and H120 samples. The overall composition agrees well with the earlier averaged measurements in various locations. The H35 material appears lower in Ni content than the H120 material. For the H35 sample, the melt pool boundaries appear to be richer in Ni than the inter-boundary regions. The H120 the composition differences appear to occur in different melt pools, with some cross sections being higher in Ni content than others. This is likely due to the repeated cross hatch pattern of the beam forming a 3D repeating grid like shape; since it is impossible to cut the samples exactly parallel to the grid axis, the different melt pools have different thermal histories, and thus different compositions.

Figure 49 shows the density plots of all of the individual composition measurements used to make the previous area maps. Table 8 shows the mean and standard deviation values for the Ni content (at%) measurements. The mean values are lower than those captured in the previous averaging WDS measurements. For the H35, the Ni content measured 46.09 vs 47.95 at%, and for H120 it was 48.56 vs 49.09 at%. This may indicate that there are compositional differences on a larger scale than was captured in the area maps. The standard deviations of both H35 and H120 agreed well with previous WDS measurements however.

Table 8: Mean and standard deviation of Ni content, at% for H35 and H120.

Sample	Mean (at%)	Standard Deviation (at)%
H35	46.09	0.84
H120	48.56	0.45

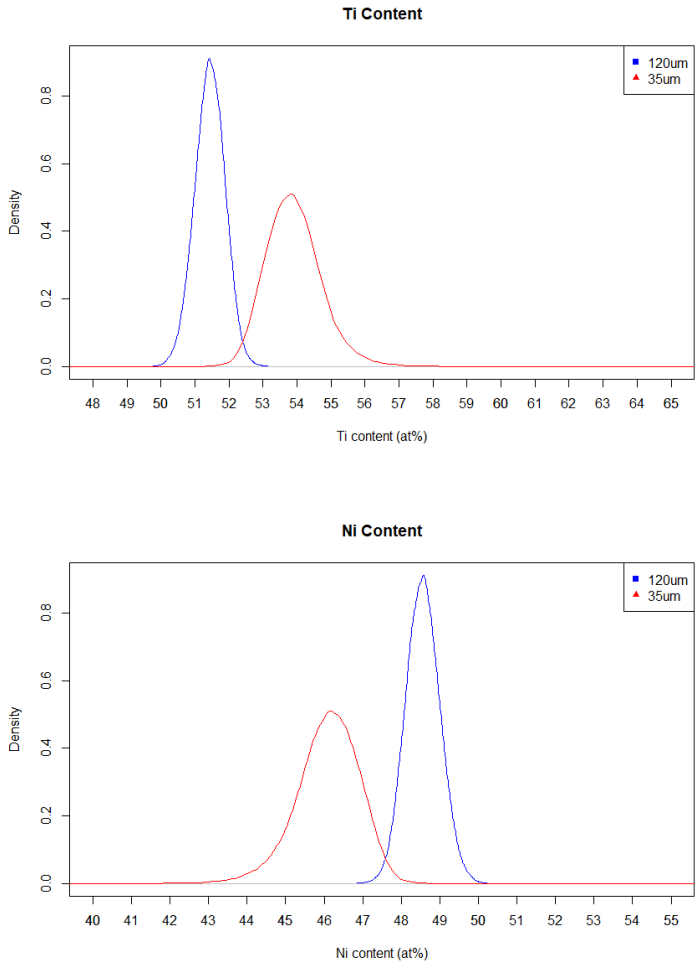

Figure 49: Density plot of composition measurements for Ni content and Ti content for H35 and H120.

From the density plots of Figure 49, it can be seen that the distribution of H35 Ni content is broader than that of the H120 Ni content. However, both the H35 and H120 distributions are below 50 at% Ni. Referring back to the previous section, the M_s temperature of H35 was 64°C and the M_s temperature of H120 was 62°C. According to the Ni-content M_s temperature relationship, the maximum M_s temperature that occurs when the Ni content reaches 49.75 at% Ni is 57°C. The transformation temperatures of H120 and H35 correspond well to Ti-rich materials. Since the distribution of Ni content in both H120 and H35 are below equiatomic, according to

the Ni-M_s temperature relation, composition is unlikely to contribute to variation in transformation temperature.

5.2 Precipitates and Dislocations

In order to characterize the size, type, and distribution of precipitates, TEM specimens were taken using FIB from selected locations with respect to the melt pools. For the H35 sample, the selected FIB locations corresponded to the center of a selected melt pool. For the H120 sample, the FIB locations corresponded to the center and edge of a selected melt pool. Figure 50 shows SEM-SE images, with the locations of the FIB-TEM specimens highlighted.

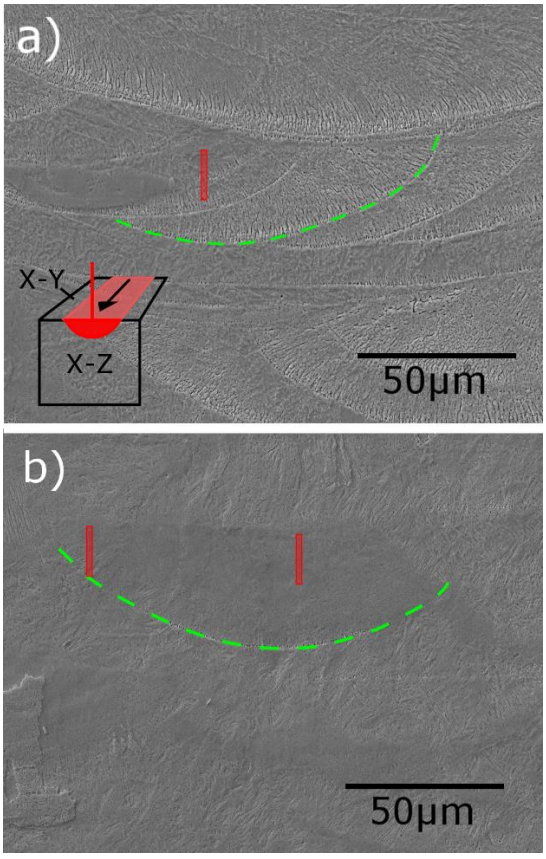

Figure 50: SEM images showing locations where FIB-TEM specimens were taken for a) H35 and b) H120. The red markers indicate the locations where TEM specimens were taken [58].

All 3 conditions (H35, H120 center, and H120 edge) exhibited a structure composed of subgrains which were between 200-600nm in diameter. The matrix was a mixture of B2 austenite, R-phase, and small areas of B19' twins. Figure 51 shows a TEM image displaying the microstructure of the H120 center sample.

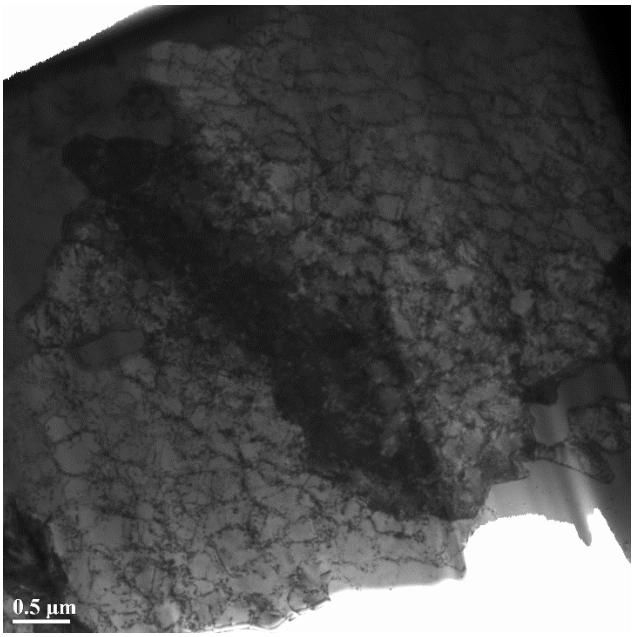

Figure 51: Low magnification TEM image of the H120 center sample.

This was expected since the samples cooled down from high temperature where they were in the B2 phase, and at room temperature had cooled down past the M_s temperature, but not below the M_f temperature.

At higher magnifications, it was found that small, 10's of nanometer diameter precipitates decorated the subgrain boundaries, with some precipitates filling the subgrain interiors. TEM images showing the precipitates and subgrains are shown in Figure 52.

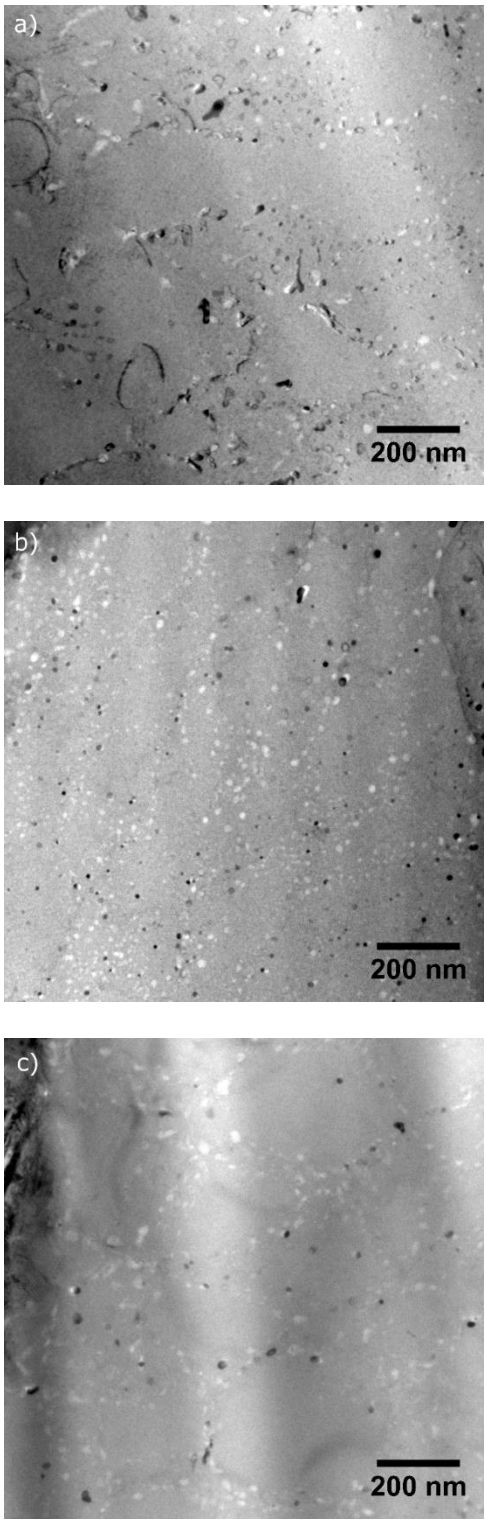

Figure 52: TEM images showing precipitates and subgrains for a) H35, b) H120 center, and C) H120 edge specimens [58].

The precipitates observed in the H120 center sample and the H120 edge sample have a regular, spherical morphology. However, the precipitates in the H35 sample have elongated, irregular shapes. This is likely due to the number of remelting/reheating cycles that each sample location undergoes. The H120 center sample and H120 edge sample experience fewer reheating cycles than the H35 sample. During each reheating event, and during each subsequent layer, the temperatures in the melt pool under consideration experience temperature elevation due to the new melt pools being formed adjacent to and above them. The H120 material, due to the wide hatch distance, stays in the

Figure 53 shows EDS spot measurements of various locations in the matrix and on precipitates. It can be seen that the precipitates are highly Ti rich, and have a Ti:Ni ratio of close to 2 to 1. This indicates that the precipitates are Ti_2Ni or Ti_4Ni_2; this is unsurprising since the composition of the samples is Ti rich.

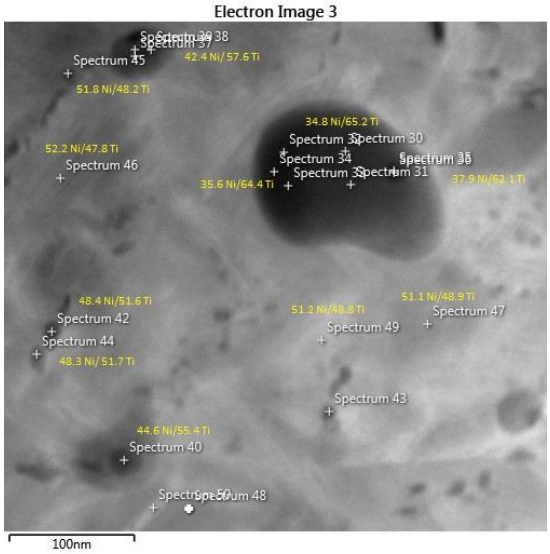

Figure 53: TEM EDS spot measurements of various points in the matrix and precipitates.

In order to further determine the composition of the precipitates, APT experiments were performed on the H35 and H120 center samples. In this case, line scans through a number of precipitates detected the amounts of Ti, Ni, C, O, and TiO. The results are shown in Figure 54.

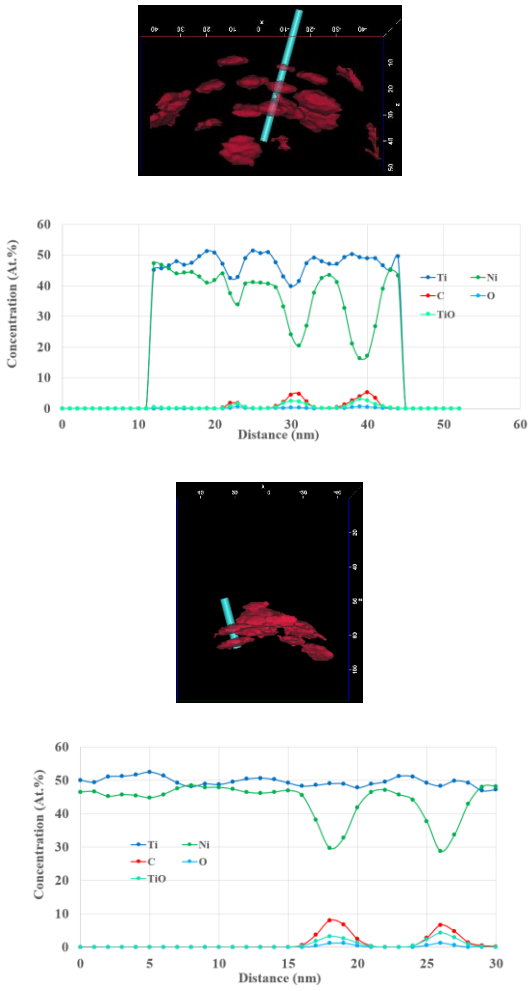

Figure 54: APT line scans for top) H35 and bottom) H120 center.

The APT line scans revealed elevated levels of C, O, and TiO. This further evidence indicates that the precipitates are likely Ti_2Ni-O, Ti_4Ni_2-O, TiC and TiO. The elevated C content comes from the Nanoval gas atomization process, which uses a carbon crucible to melt the feed material

before atomization, and the elevated O content occurs due to the high energy densities during SLM processing. Furthermore, high resolution TEM imaging revealed a second, smaller distribution of precipitates. These can be seen in Figure 55. These precipitates are smaller than 3nm in diameter, and are an order of magnitude smaller than the Ti2Ni-O precipitates previously observed. The small interparticle distance associated with these precipitates indicates that they are likely to affect the transformation temperatures.

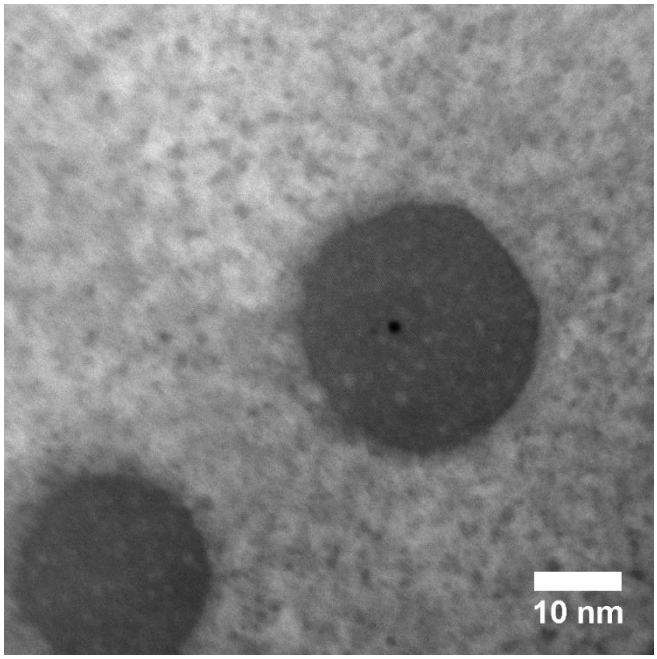

Figure 55: High resolution TEM from H120 edge, showing small, <3nm precipitates [58].

Returning to the large precipitates, differences in precipitate size, volume fraction, and number fraction were observed. The precipitate size and volume fraction measurements are shown in Table 9. The total volume fraction of precipitates was highest for H35 with 0.086, followed by H120 center with 0.078, and the smallest was H120 edge with 0.066. The number densities for H35 and H120 center were similar, with 160 and 156 precipitates per μm^2 respectively, with H120 edge having the highest number density of 198 precipitates per μm^2.

Figure 56 shows density plots for the precipitate sizes for H35, H120 center, and H120 edge. All of the distributions are right skewed; the bulk of the precipitates in all three specimens are smaller, below 1000nm^2. The figure shows that the distributions for both the H35 and H120 center precipitates are very similar. The mode for H35 is 121nm^2, for H120 center is 92nm^2, and for H120 edge is 49nm^2. This means that for H120 edge, the largest number of precipitates are smaller in area than those of H35 and H120 center.

Table 9: Volume fraction and number density of precipitates for H35, H120 center, and H120 edge samples

	H35	H120 Center	H120 Edge
Volume Fraction	0.086	0.078	0.066
Number Density (num/μm^2)	160	156	198

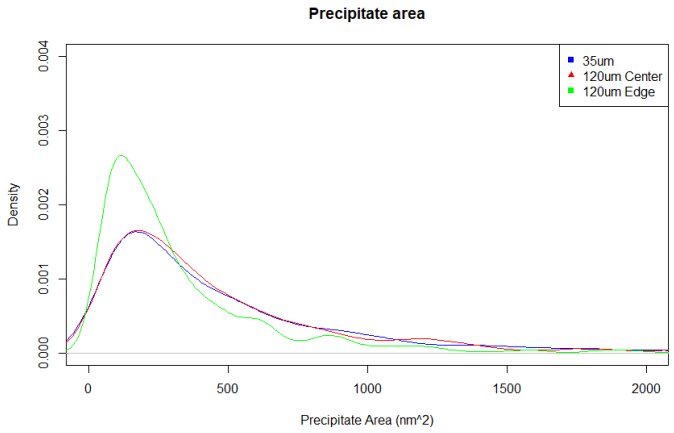

Figure 56: Precipitate area density plots for H35, H120 center, and H120 edge.

Figure 57 shows TEM images of the H35, H120 center, and H120 edge specimens tilted for optimum contrast for dislocations. It can be seen that the H35 sample has a very low

dislocation density, especially in comparison to H120 center and H120 edge. H120 center has the highest dislocation density of the three samples, while H120 edge shows fewer dislocations.

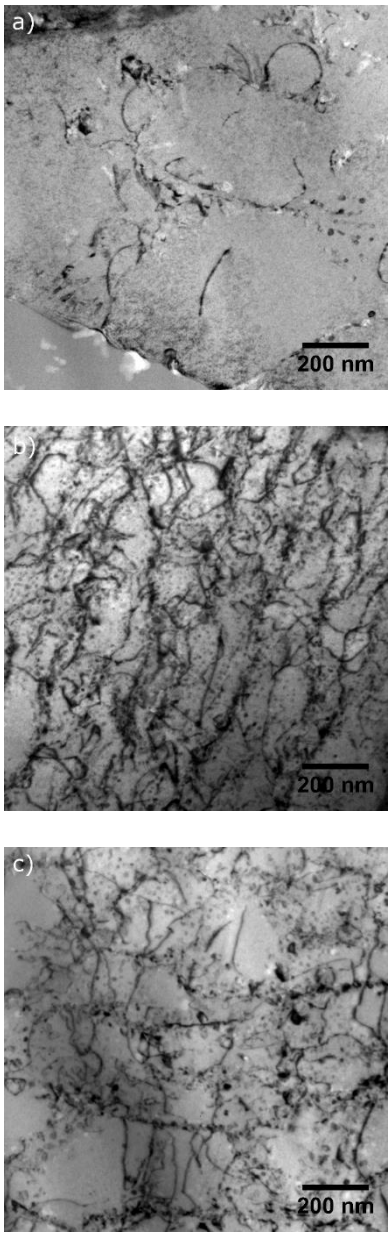

Figure 57: TEM images of a) H35, b) H120 center, and c) H120 edge specimens tilted to obtain optimum contrast of dislocations [58].

5.3 Discussion

Out of the six possible mechanisms that could have affected the transformation temperatures, three have been investigated so far. The remaining two are grain size and stress. Figure 58 shows color-etched optical microscope images for H35 and H120, in both the X-Y and X-Z plane.

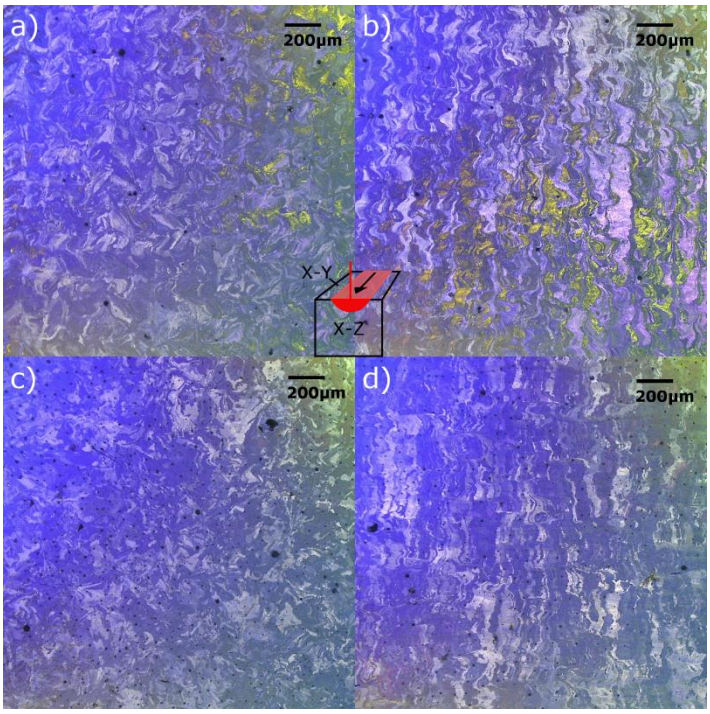

Figure 58: Color-etched optical microscopy images for a-b) H35, and c-d) H120. The images on left correspond to the X-Y plane, and the right to the X-Z plane [58].

The grain morphology agrees well with previous experiments by Bormann [34]. The top X-Y surfaces show a characteristic checkerboard pattern, which occurs due to the rastering of the beam in perpendicular directions. In the X-Z plane, it can be seen that the grains are elongated along the beam direction; this occurs due to epitaxial growth of the grains. While the grains are quite irregularly shaped, they are visible in the micron scale. This means that the grains are far too large to cause increases in thermal hysteresis, and concomitant shifts in the transformation

temperatures. Therefore, grain size can be eliminated as a possible source of variation in transformation temperatures. It should also be noted that a [100] texture oriented with the beam direction is expected. However, in SMAs texture affects the shape memory behavior under stress by affecting the fraction of martensite variants that are favorably oriented towards the shear direction [114, 115]; in the current case, since the DSC experiments are performed under load free conditions, they do not affect the transformation temperatures

Oriented stresses increase the transformation temperatures in SMAs. The stress-temperature relationship is normally given using a Clausius-Clapeyron type relation:

$$\frac{d\sigma}{dT} = -\frac{\Delta H}{\varepsilon T} \qquad 2)$$

where H is the enthalpy of transformation, and ε is the transformation strain [116]. Typical values for the stress-temperature coefficient range between 6-10 MPa/°C. Considering that the interval of transformation for H120 was 96°C, and using the low value of the coefficient, this would mean that the stress would need to reach 576 MPa in order to explain this shift in transformation temperature.

While the residual stresses have not been directly measured in SLM-built NiTi as of yet, there is a plethora of evidence to suggest that the residual stresses in the DSC specimens would not reach the necessary levels to impact the transformation temperatures. Gnaupel-Herold et. al performed neutron diffraction experiments in order to measure the residual stress at different locations in a 10mm cube made from 17-4 steel [117]. It was found that the highest residual stresses were observed at the external surfaces of the sample; in the center of the sample the residual stresses were near 100 MPa. It must be noted that these measurements were performed for a test artifact that had not been removed from the substrate. Mercelis et. al performed x-ray

diffraction to measure the residual stress on the surface of a 10mm high part [76]. It was found that on removing the part from the substrate, the residual stress dropped from 146-69 MPa in the X direction, and 165-65 MPa in the Y direction. Additionally, in the current work the DSC specimens were EDM cut from the center of the cubes. This would mean that the effect of the high X-Y plane residual stresses on the top and bottom surfaces and the high Z stresses on the outer planar surfaces would be relieved, and the residual stress in the DSC specimen would be further decreased. It is then unlikely that residual stress played a significant role in affecting the transformation temperatures in the H120 sample.

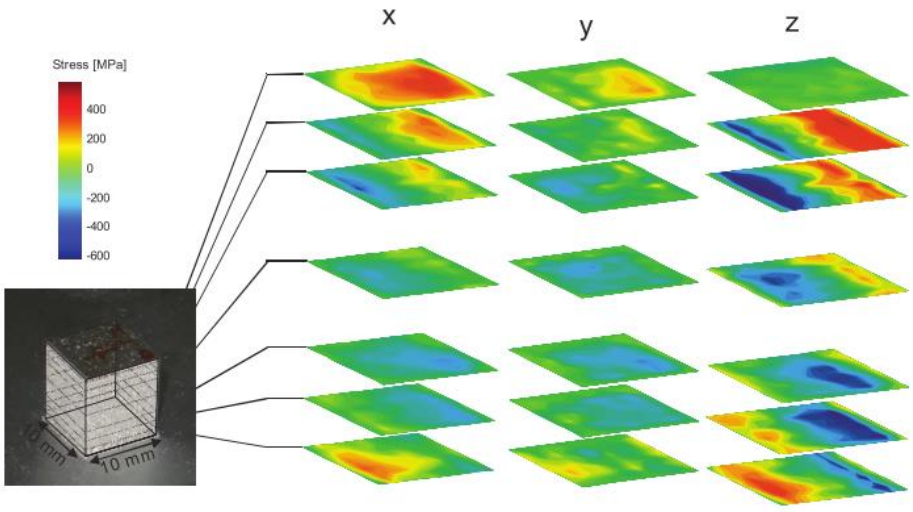

Figure 59: Residual stress x, y, and z components measured using neutron diffraction in a 17-4 stainless steel 10mm cube [117].

Returning then, to the three mechanisms where it was shown variability occurred; composition, precipitation, and dislocation density. It was found that compositional gradients were present in both the H35 and H120 samples. The Ni content in H35 was lower than H120, with an average of 46.09 at% Ni versus 48.56 at% Ni. Additionally, it was found that the distribution of composition was broader for H35 and H120. The changes in composition from the

initial measurement of 50.08 at% Ni are attributed to Ni evaporation during the SLM process. The mass flux of evaporation and evaporation coefficient are given by:

$$j = p_s(T_s)\sqrt{\frac{m_a}{2\pi * k_b T_s}} \tag{3}$$

$$\emptyset = \sqrt{2\pi\gamma_v} * Ma_{Kn}(T_s) * \frac{\rho_{Kn}}{\rho_s}\sqrt{\frac{T_{Kn}}{T_s}} \tag{4}$$

where j is the mass flux, p_s is the saturation vapor pressure, T_s is the surface temperature, m_a is atomic mass, k_b is Boltzmann's constant, $\emptyset$ is the evaporation coefficient, Ma_{Kn} is the Mach number, ρ_{Kn} is the vapor pressure at the Knudsen layer, and T_{Kn} is the temperature at the Knudsen layer [71]. Due to the temperature dependence of p_s and Ma_{Kn}, evaporation flux increases with temperature. Additionally, it is known that in NiTi alloys, Ni evaporates preferentially due to the difference in vapor pressures [118] (where Ni has a higher vapor pressure than Ti).

In the melt pool, the highest temperatures are observed for the center of the melt pool, since the beam is gaussian distributed and the highest energy flux is at the center. The center region will be at the boiling temperature, and the outer perimeter will be at the melting point. In NiTi, the melting point is 1310°C. While there is a lack of data as to the boiling temperature of NiTi, the boiling temperature of Ni is 2913°C, and of Ti 3287°C. Thus, across the melt pool there is a thermal gradient approaching 2000°C.

Oliveira et. al performed an experiment where a single laser track was laid upon a NiTi substrate with a Ni-rich composition (50.8 at%) [119]. The melted track was then measured using x-ray diffraction to determine the transformation temperatures at different points relative to the melt track.

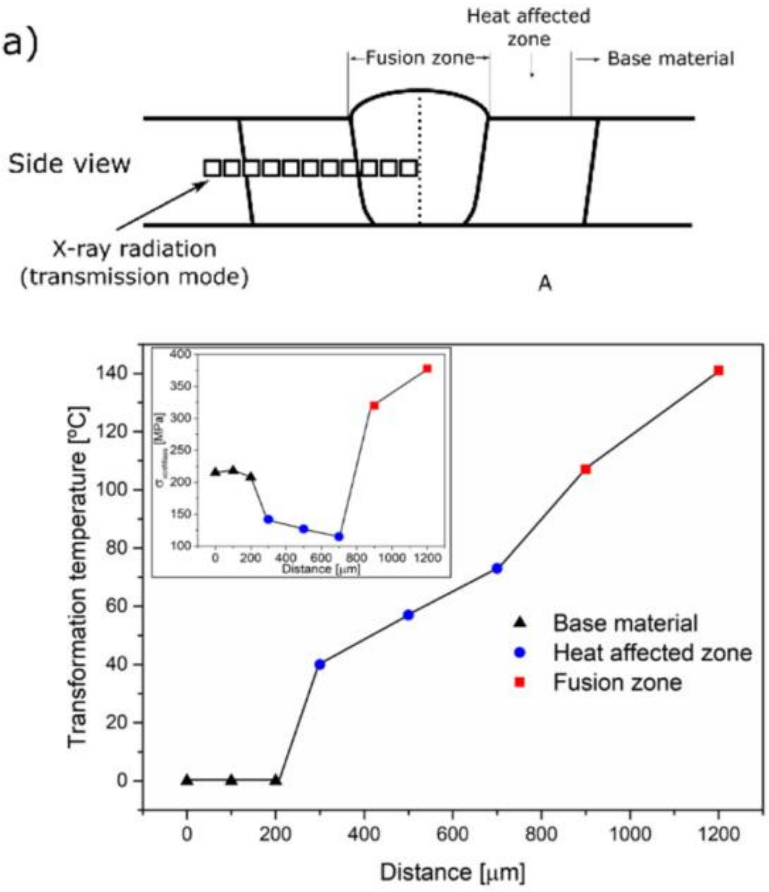

Figure 60: Experiment to determine transformation temperatures as a function of location across a melt track. Top) Schematic showing the melt pool and the locations of measurements. Bottom) Measured transformation temperatures [119].

Figure 60 shows the measured transformation temperatures as a function of location relative to the laser melt track. The highest measured transformation temperatures occurred in the direct center of the melt pool, decreasing gradually through the heat affected zone, and finally reaching to the lowest temperatures which correspond to the substrate. The difference in transformation temperature between the center of the melt pool to the substate is quite large, reaching 140°C. This gradient in transformation temperature was not only attributed to the gradient in composition, but a gradient in precipitate formation.

In SMAs, precipitate interparticle distance is known to suppress transformation temperatures and increase the thermal hysteresis [44]. In conventional NiTi, short duration, low temperature aging treatments correspond to fine distributions of closely spaced precipitates, and this condition results in low transformation temperatures. As the aging temperature and duration increases, the precipitates coarsen, with larger precipitates growing even larger at the expense of smaller precipitates which dissolve into the matrix, resulting in higher transformation temperatures [92]. It follows then that matrix locations near the center of the melt pool experience a different thermal history than those at the edge of the melt pool; which results in a difference in precipitate size, volume fraction, and interparticle distance. The effect of additional layers should also be considered; as further layers are added the previous layers experience additional thermal excursions, which cause further nucleation and coarsening of the precipitates. Ma et. al performed FEA simulations of single points during the SLM processing of NiTi [59]. The output of the simulation is shown in Figure 61.

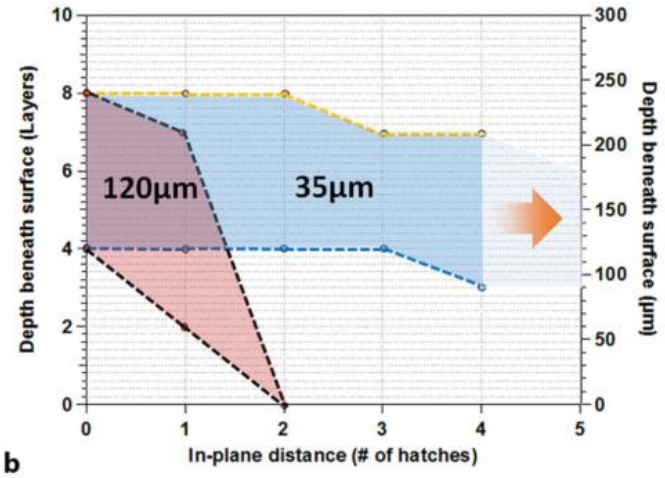

Figure 61: Simulated thermal history for single points in an SLM-built NiTi sample. The figure shows the spatial regions in which the material point remains in the thermal precipitation zone [59].

The figure shows that in the H35 sample the material experiences thermal excursions during the same layer even after more than 5 adjacent tracks have been formed. The first three layers above this are sufficient to remelt the material; however, the next four layers continue to increase the temperature in the first layer to the range in which precipitation occurs. Even in these additional reheating layers, the adjacent tracks continue to reheat the material point in question, leading to further precipitate evolution. For the H120 sample, it can be seen that the precipitate thermal zone is much smaller due to the wider hatch distance. The effect of adjacency of the tracks is more muted, and only the immediately adjacent tracks have sufficient reheating effect on the initial point (except in the first layer, where the third track impacts the first. Johnson et. al performed finite element thermal and precipitate simulations for the H35 and H120 conditions. The resulting phase fractions are shown in Figure 62.

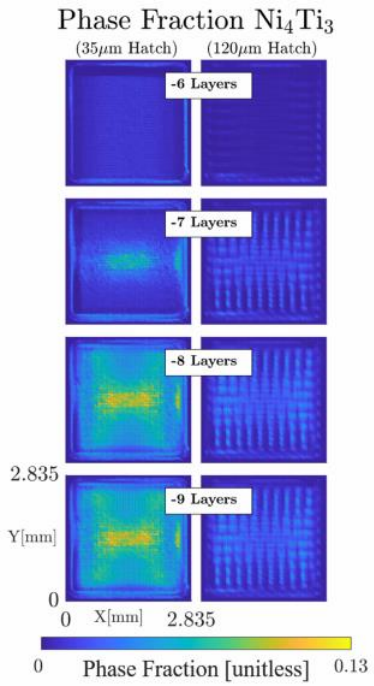

Figure 62: Simulated phase fractions of Ni_4Ti_3 in Ni-rich NiTi, with permission from author [120].

The figure shows that in the H120 sample localized regions with elevated volume fractions and low volume fractions of Ni_4Ti_3 occur in regular, repeating fashion. The pattern occurs due to the cross-hatched scan strategy used. In the H35 sample, the precipitate volume fraction is more homogenous since each local point has a thermal history very close to its adjacent neighborhood. These simulated results further validate the experimental results presented in this chapter, that H35 has locally homogenous precipitate distributions, while H120 has locally inhomogenous precipitate distributions.

Finally, it was observed that there was a difference in dislocation density between the H120 center and H120 edge specimens, with H35 having a very small dislocation density in comparison to the H120 specimens. Since dislocation density has the effect of broadening the transformation peaks in NiTi alloys, it is possible that composition, precipitation, and dislocations could all have an effect on the variation in transformation temperatures observed previously. In order to separate the effects, we performed thermal heat treatments on SLM-built NiTi specimens of the H35 and H120 conditions. Bernardini et. al performed experiments on the diffusion of Ni in a near equiatomic NiTi material [121]. Figure 63 shows the relationship between diffusion coefficient and inverse temperature. The diffusion coefficient at 510°C was reported as $7.7x10^{-19}$ m^2s^{-1}. At this temperature, the mean penetration depth of the Ni tracers was only 2μm after 81 days due to the low diffusion coefficient. Thus, heat treatment experiments were performed at 450 for 1 hour. At this temperature and time, there would be sufficient thermal energy to promote coarsening and dislocation motion and annihilation, while diffusion of Ni and Ti from rich regions and poor regions would be sluggish.

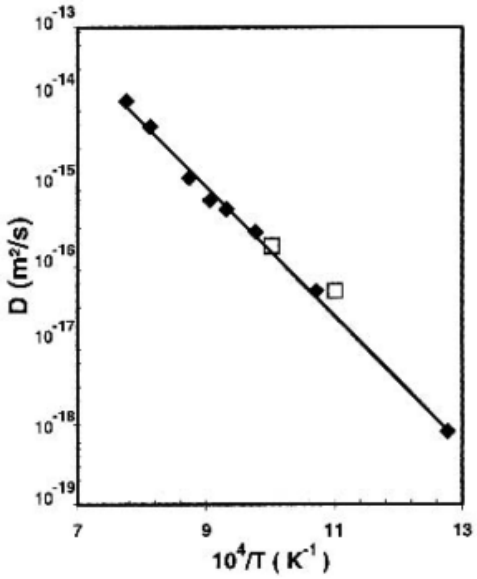

Figure 63: Diffusion coefficient for Ni in equiatomic NiTi with inverse temperature [121].

Figure 64 shows the results of DSC experiments of H35 and H120 heat treated to 450°C. It can be seen that the transformation temperatures of the H35 material do not change appreciably even after heat treatment. Instead, the transformation peaks increase in enthalpy without shifting in the temperature domain. In the case of H120, however, the transformation peaks have narrowed, and the transformation temperatures have shifted towards each other. Table 10 lists the transformation temperatures for both the heat treated and as-built H35 and H120 samples. For H120, the M_s and A_f temperatures were relatively unaffected by heat treatment. However, the M_f shifted by 52°C, and the A_s temperature shifted by 29°C. The austenite to martensite transformation interval decreased from 96°C to 45°C, and the martensite to austenite transformation interval decreased from 86°C to 61°C. For H35, the M_f temperature did increase by 10°C, while the other transformation temperatures remained relatively constant. The austenite to martensite transformation interval decreased for H35 from 39°C to 29°C.

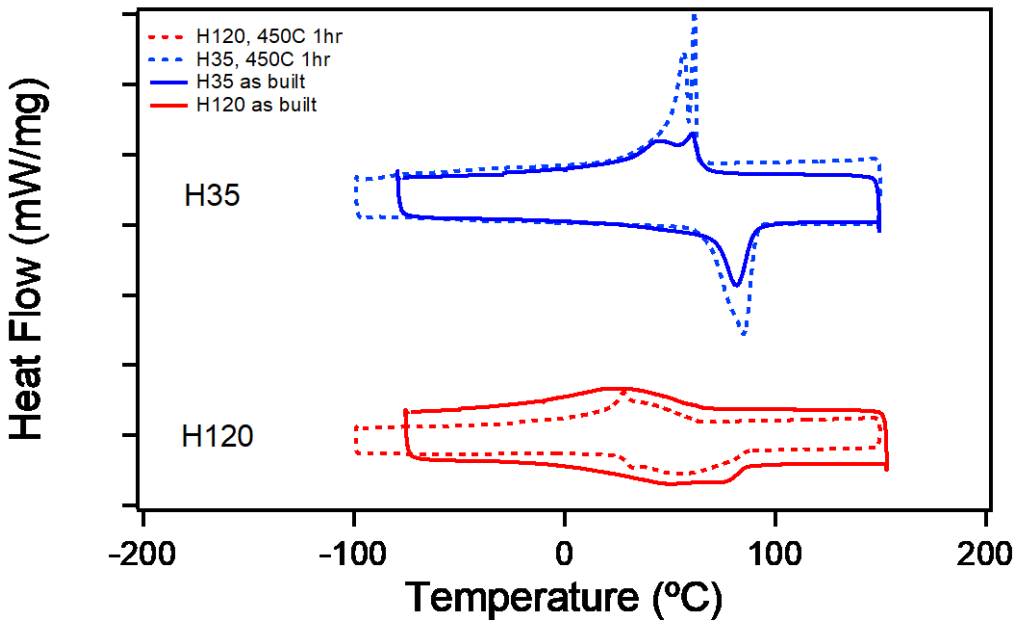

Figure 64: DSC experiments for H35 and H120 heat treated to 450°C for 1hr.

Table 10: Measured transformation temperatures from DSC experiments for H35 and H120 as-built and heat treated.

Sample	M_s	M_f	A_s	A_f	Hyst	M_{int}	A_{int}
H35	64	25	69	90	26	39	21
H35 HT	64	35	68	91	27	29	23
H120	62	-34	-4	82	20	96	86
H120 HT	63	18	25	86	20	45	61

The results of the DSC experiments on heat treated specimens indicates that heat treatment at low temperatures where long range diffusion is difficult was still effective at narrowing the transformation intervals in H120. The narrowing of the H120 transformation intervals indicates that the variation of precipitate volume and interparticle distance and/or the variation of dislocation density is decreased by the heat treatment, which is further evidence that the primary

mechanisms of variability in transformation temperature is dominated by precipitate and dislocation effects.

5.4 Summary of main findings

In this section, we investigated the microstructural and compositional mechanisms that could be responsible for variability in the stress-free transformation behavior of SLM-built NiTi. The proposed mechanisms were variations in composition, precipitate volume fraction and interparticle distance, dislocation density, grain size, texture, and residual stress.

Texture and residual stress were eliminated as possible mechanisms due to the conditions of the specimens and experiments. Since the measured transformation temperatures were taken under stress free conditions, texture could not have affected the results. Residual stresses in the DSC specimens was expected to be too low to cause the large variation in temperatures, due to the fact that the specimens were taken from the center region where residual stresses are lowest, cut free from the substrate, and then cut free from the 10mm cube, therefore relieving the greatest part of the residual stress.

Variability in Ni content, precipitate size, number fraction, and area fraction, and dislocation density were all observed. Ni content variation occurred due to preferential evaporation of Ni, and the steep thermal gradient across the melt pool. Precipitate size, number and area fraction variations occurred due to differences in thermal history in the H120 samples relative to the edge and center of the melt pool, mainly due to the large hatch distance. In the H35 sample, due to the small hatch distance each point in the material experienced similar thermal histories, and therefore had similar precipitate distributions. Dislocation density was

observed to vary dependent on location relative to the melt pool center or edge in H120, and H35 exhibited lower dislocation density than H120.

Since the Ni content of both the H120 and H35 was below the equiatomic level composition was not expected to be effective in changing the transformation temperatures. It was also found that heat treatments at low temperature, where long-range diffusion would be sluggish, did reduce the variability in transformation temperatures for the H120 specimen; this further indicates that the effect of precipitates and dislocation density dominated compositional gradient effects.

CHAPTER VI

VARIABILITY IN THE MECHANICAL RESPONSE OF NITI

In the previous sections it was shown that under stress-free conditions, the transformation temperatures of SLM-built NiTi exhibited both localized variability as well as part-to-part variability. It has been shown in the literature that part-to-part variability of mechanical properties (or the repeatability of mechanical properties in parts that have been built under the same processing conditions) is higher in SLM-built materials. In this section, we investigate the mechanical properties of SLM-built NiTi specimens tested under tension. Since it is known that variability occurs in the transformation temperatures under stress free conditions, it is necessary to see if this extends to the mechanical behavior of NiTi under stress, since most applications of NiTi will involve tensile or compressive stresses.

To accomplish this a large number of tensile specimens were built using SLM with the H35 and H120 conditions. The specimens were then tested under uniaxial tension to failure, and the mechanical properties measured thereafter. In the first part of this section we will detail the design of the experiments, the geometry and processing of the samples, and the conditions of testing. In the second part we discuss the variability of thermomechanical properties under stress at 100°C, and in the last part we discuss the variability of thermomechanical properties under stress at room temperature.

6.1 Details of the experimental design

For each process parameter set (H35 and H120) six different blocks (with dimensions 28x32x12) were printed for a total of 12 blocks. Each individual block, after EDM cutting,

yielded 4 separate tensile specimens, for a total of 24 per parameter set and 48 overall. The gauge cross section of each dogbone specimen was nominally 0.9x3mm. The H35 sample groups were given labels of A-F, and the H120 samples given labels of α- ζ. The list of specimens is given in Table 11. The tensile specimens were cut from the interior of the blocks with the width dimension of the tensile specimen oriented along the beam axis, and the length of the gauge section oriented in the X directions. All of the specimen blocks were printed using the same orientations. Since all of the specimens were tested with the uniaxial tensile stress in the same orientation, texture effects could be avoided.

Due to issues with sample fabrication, there were some minor differences in the specimens. The A-D groups for H35 and α-β groups for H120 had holes drilled for pinning in the tensile specimen; the holes were drilled using conventional bits. All other samples had holes cut using EDM. However, it should be noted that these differences would affect ultimate tensile stress and strain to failure; in the current work we disregard these mechanical properties, since in tension would be dominated by porosity, and instead focus on the elastic modulus and yield stress. Also, one test specimen for H35 group D failed prematurely due to machine failure, and no result was obtained.

Once the samples were cut and mechanically ground on the exterior surfaces using 400 grit paper, each individual sample was mechanically strained to failure at either 100°C or room temperature. The 100°C test temperature was due to the fact that at room temperature, both samples would have a mixture of austenite, martensite, and R-phase, and differences in mechanical behavior would result from the relative phase fractions of each. At 100°C the material from process parameter sets were at least 10°C above the austenite finish temperature, ensuring that the matrix was single phase, and thus the results would be more comparable.

Table 11: Experimental design for the tensile specimens tested at 100°C and RT for H35 and H120.

Process Parameter	Group	# Tests, 100°C	# Tests, RT
H35	A	2	2
H35	B	2	2
H35	C	4	0
H35	D	3	0
H35	E	4	0
H35	F	0	4
H120	α	2	2
H120	β	2	2
H120	γ	4	0
H120	δ	4	0
H120	ε	4	0
H120	ζ	0	4

6.2 Variability of mechanical properties under stress at 100°C

The results of the monotonic mechanical tests of H120 at 100°C are shown in Figure 65. At this temperature, the matrix in all samples is above the A_f, and so the dominant phase is austenite. At the yield point, the specimens from all groups exhibit gradual hardening until failure. Within each group, the specimens appear to have similar curves. For example, the H120 epsilon group, alpha group, and beta group all exhibit gradual hardening after the yield point. However, the delta and gamma groups have a more pronounced 'elbow' at the yield point. There is significant scatter in the failure at elongation, but this is expected due to the porosity dominated failure mechanism.

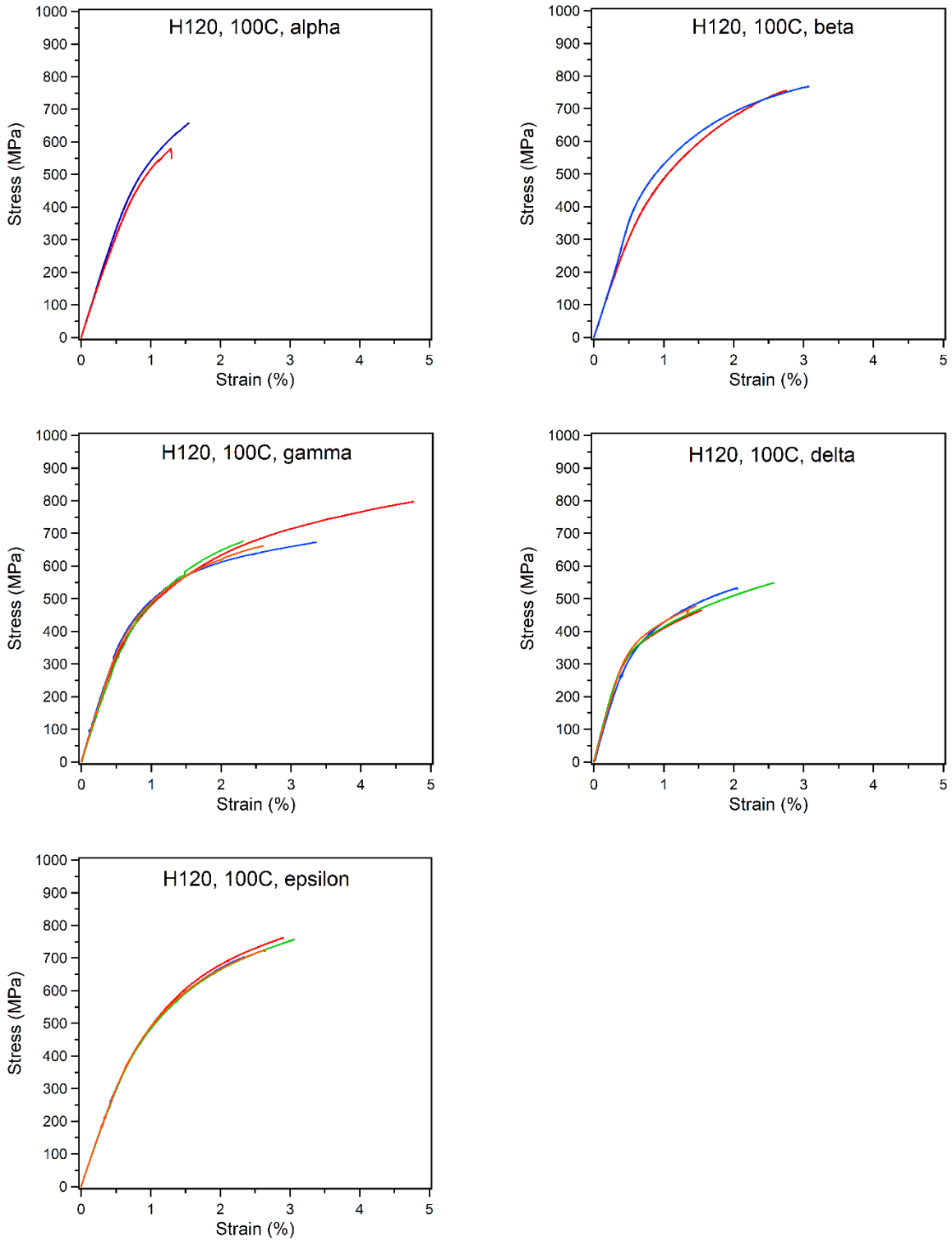

Figure 65: Monotonic mechanical test results for H120 specimens tested at 100°C separated by group.

Figure 66 shows all of the H120 stress-strain curves for testing at 100°C in a comparison plot. It can be seen that the curves are clustered together by grouping. Additionally, it can be noted that all specimens fail at low elongation in comparison to conventional NiTi; again, this is due to the presence of porosity in all specimens.

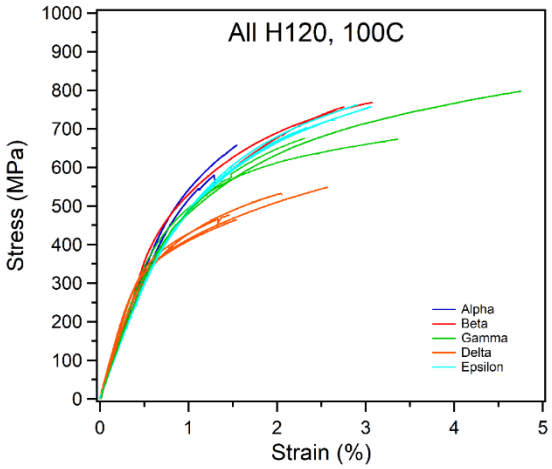

Figure 66: Comparison plot for H120 monotonic mechanical test results at 100C.

Figure 67 shows the H35 stress-strain curves for H35 tested at 100°C separated by group. At 100°C, the material is entirely in the austenite condition, considering the A_f temperature of 90°C. Again, as in the H120 specimens, the curves in each group are similar and there does not appear to be a great deal of experimental scatter. The H35 samples appear to have a more pronounced elbow at the yield point in comparison to H120, in which 3 of the 5 groups had more gradual hardening behavior, and two had elbow behavior. Figure 68 shows the overall comparison plot for all H35 100°C stress-strain curves. The stress-strain curves appear to less clustered than the H35 samples, with most of the curves more or less on top of eachother.

Table 12 gives the measured elastic moduli, 0.2% offset yield strengths, with mean and standard deviations, and the coefficients of variation for H35 and H120 samples. H35 had a

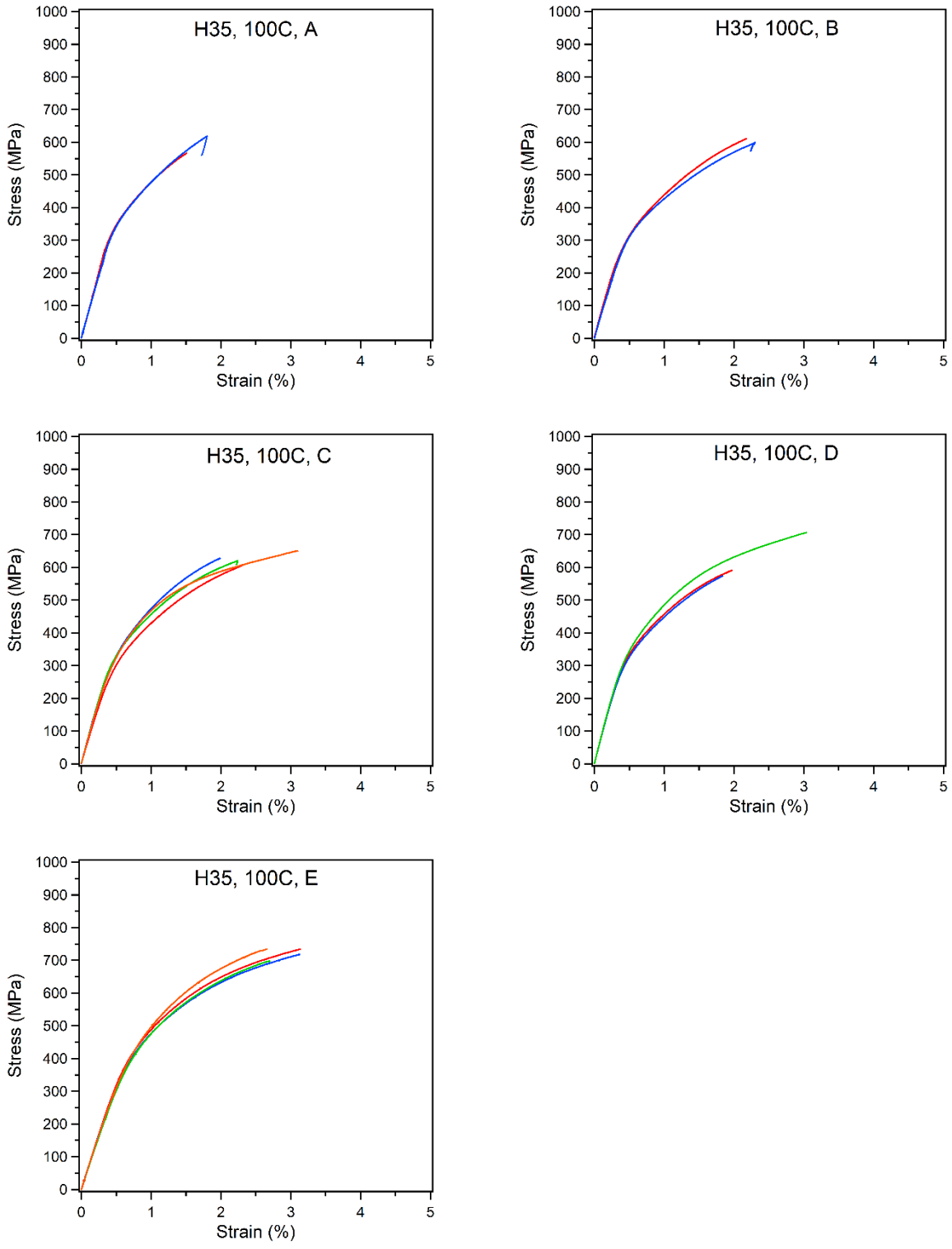

Figure 67: Monotonic mechanical test results for H35 specimens tested at 100°C separated by group.

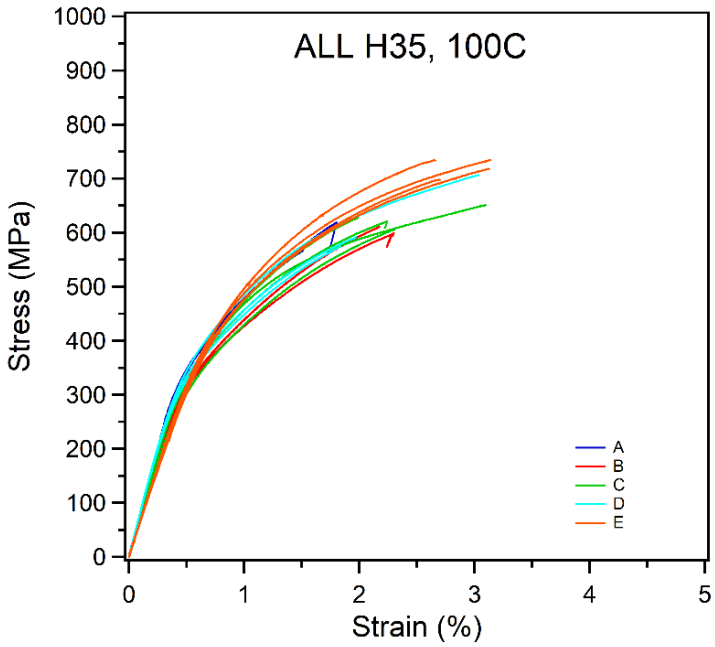

Figure 68: Comparison plot for H120 monotonic mechanical test results at 100C.

higher mean elastic modulus than H120, with 76029 MPa compared to 70910 MPa. The standard deviation for the elastic modulus of H35 was smaller than H120, with 6722 Mpa compared to 9079 MPa. The coefficient of variation for the elastic modulus for H35 was also smaller than H120, with 0.088 compared to 0.128. The mean yield strength of H35 was lower than that of H120, with 404 MPa versus 450 Mpa. The standard deviation for the yield strength was smaller for H35 than H120, with 36 MPa versus 61 MPa. Finally, the coefficient of variation of the yield strength of H35 was lower than that of H120, with 0.89 versus 0.136.

Table 12: Measured elastic modulus and 0.2% offset yield strength, with coefficient of variation for H35 and H120 specimens tested at 100°C.

Sample	E_m mean (MPa)	E_m std.dev (MPa)	V_{cE}	$Y_{0.2}$ mean (MPa)	$Y_{0.2}$ std.dev (MPa)	V_{cY}
H35	76029	6722	0.088	404	36	0.089
H120	70910	9079	0.128	450	61	0.136

6.3 Variability of mechanical properties under stress at room temperature

Figure 69 shows the result of monotonic testing of H35 at room temperature separated by group. At RT, the material is almost entirely martensite due to the M_s temperature of 64°C and M_f of 29°C. It can be seen that the samples exhibited yield points that were much lower than when testing at 100°C. This is due to the difference in deformation mechanism; at the higher test temperature the material is undergoing dislocation generation and possibly stress induced martensitic transformation. At RT, the deformation mechanism is detwinning of the self-accommodated martensite variants. The slope after the yield point is more gradual at room temperature in comparison to at high temperature, and again this is due to the difference in deformation mechanism. The curves are again quite similar inside the groups, showing a minor degree of experimental scatter.

Figure 70 shows the comparison plot for all of the H35 materials tested at room temperature. It can be seen that there is little clustering of the curves in comparison to H120 tested at 100°C.

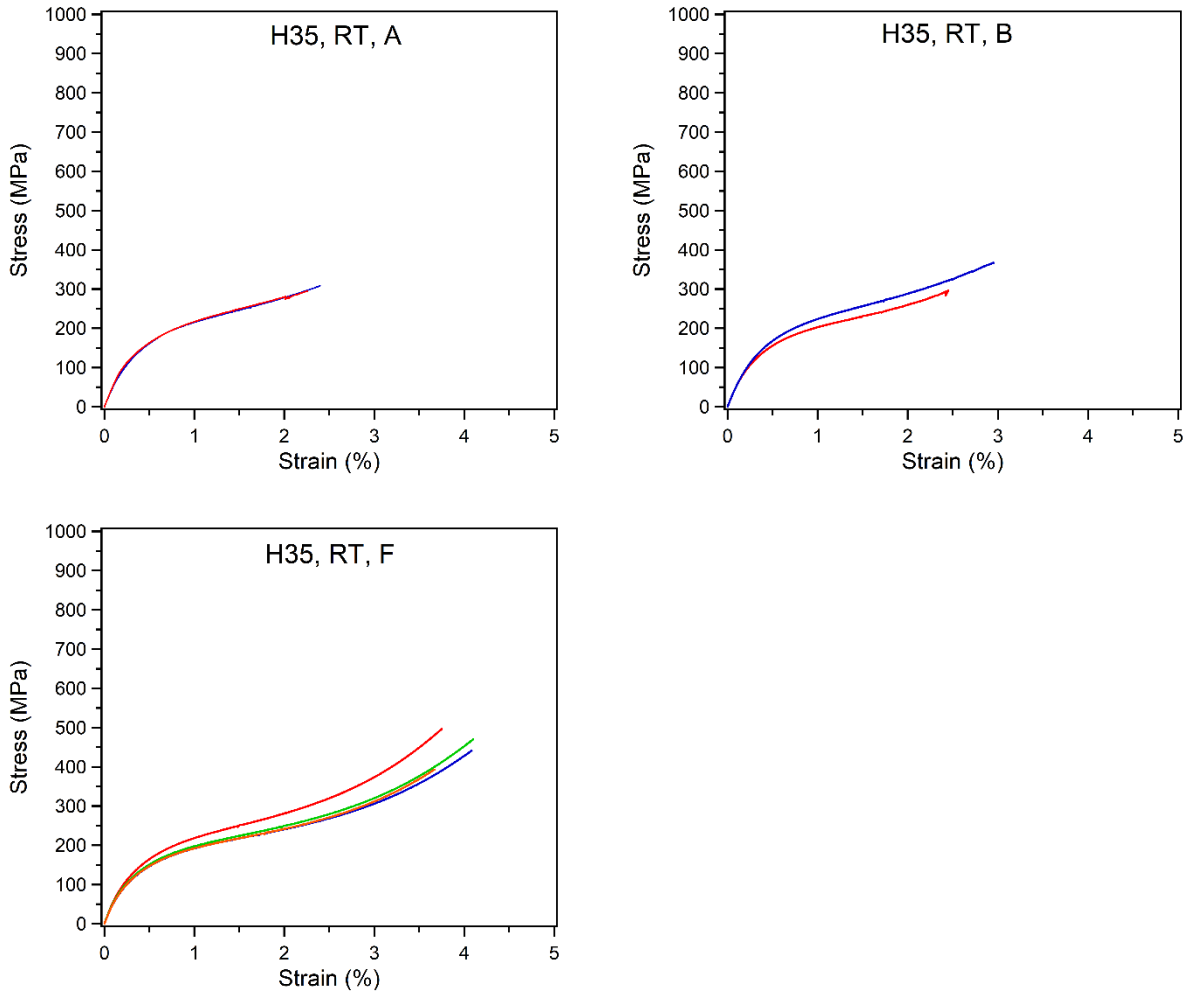

Figure 69: Monotonic mechanical test results for H35 specimens tested at RT separated by group.

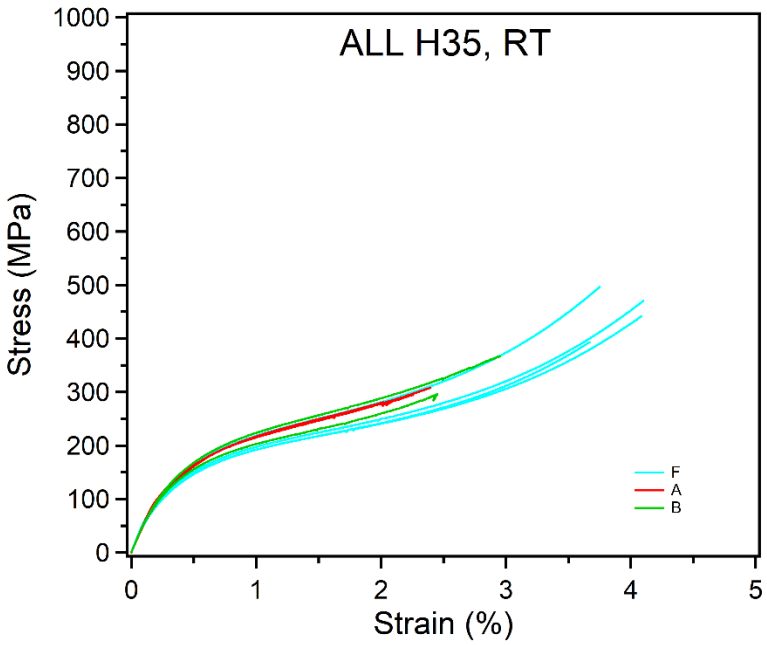

Figure 70: Comparison plot for H35 monotonic mechanical test results at RT.

Figure 71 shows the result of monotonic testing of H120 at room temperature separated by group. At room temperature, the material was partially in martensite, austenite, and R-phase; this is due to the fact that the M_s temperature is 62°C and the M_f temperature is -14°C. Thus, on cooling from high temperature the transformation has not been completed, and some austenite and R-phase remain. The specimens showed the lowest yield stresses of any of the test conditions, as well as the flattest plateau regions. Inside of each group, the stress-strain curves were very consistent.

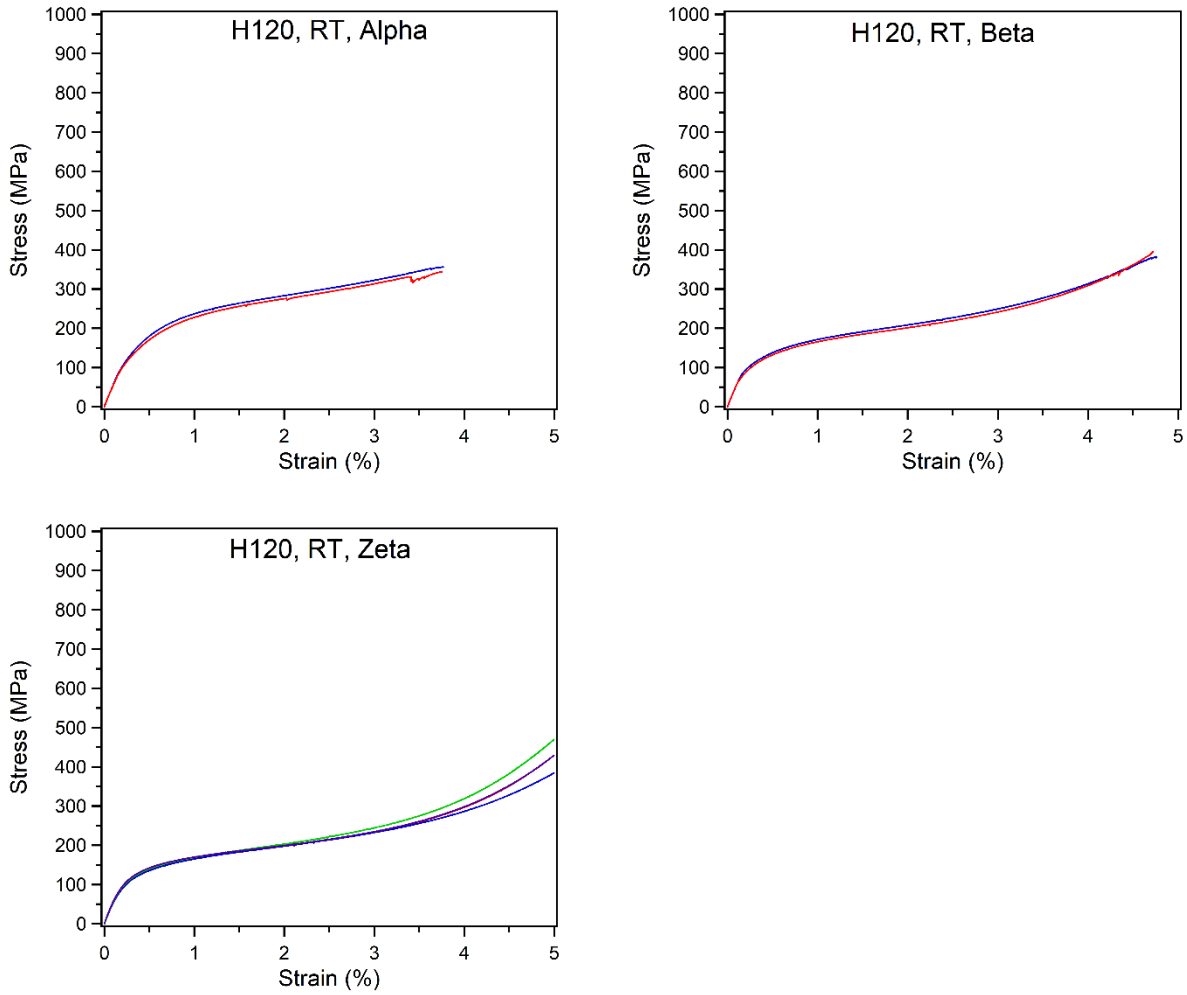

Figure 71: Monotonic mechanical test results for H35 specimens tested at RT separated by group.

Figure 72 shows the comparison plot for all H120 specimens tested at RT. From the plot it can be seen that there is separation of one of the groups. The Beta and Zeta groups are very consistent with each other, while the Alpha group showed a higher yield stress. However, the slopes of the plateau regions were approximately similar.

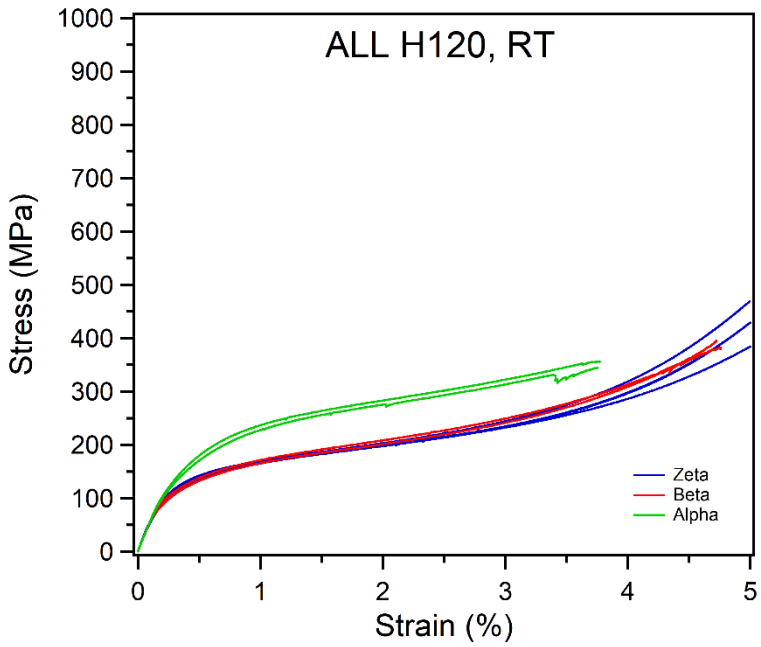

Figure 72: Comparison plot for H120 monotonic mechanical test results at RT.

Table 13 shows the mean, standard deviation, and coefficient of variation for the measured elastic modulus and yield strength of the H35 and H120 specimens. It can be seen that the elastic moduli and yield strengths are smaller at RT than at 100°C for both H35 and H120. The coefficients of variation for H35 was lower for the elastic modulus and slightly lower for the yield strength when comparing to those measured at 100°C. The coefficient of variation for elastic modulus was lower for H120 at RT than at 100°C, and the coefficient of variation for yield strength was higher. Comparisons between H35 and H120 at RT would be misleading, however, since the material conditions are different.

Table 13: Measured elastic modulus and 0.2% offset yield strength, with coefficient of variation for H35 and H120 specimens tested at RT.

Sample	E_m mean (MPa)	E_m std.dev (MPa)	V_{cE}	$Y_{0.2}$ mean (MPa)	$Y_{0.2}$ std.dev (MPa)	V_{cY}
H35	56268	2479	0.044	153	11	0.072
H120	59514	2255	0.038	141	23	0.163

6.4 Summary of main findings

In this section the mechanical behavior of SLM-built NiTi under the H35 and H120 conditions was investigated at 100°C and at RT. It was found that under tension, all specimens failed at lower elongation than conventionally processed NiTi. The early failure of the specimens is due to the porosity in the samples. It was observed that for H120 at 100°C and at RT, the stress-strain curves appeared to be clustered according to groups. This means that samples from the same printed block had similar mechanical properties. This agrees well with the previous DSC experiments on H120 that showed that there was no variation in transformation temperature for specimens cut from different locations in the same block. The H35 specimens at 100°C and RT appeared to show less clustering, and most of the results were more or less equivalent. It was also found that H120 at 100°C exhibited higher coefficients of variation in comparison to H35. A previous study of variability in stainless steels observed that the coefficient of variation for yield strength in a wrought stainless steel was 0.08 [10]; the coefficient of variation of the yield strength H35 was 0.089 and was therefore on par with that result. The coefficient of variation of the yield strength of H120 was 0.136 which exceeded the variation in conventional alloys.

CHAPTER VII

SUMMARY AND CONCLUSION

This work presents a study of variability in the stress-free transformation behavior and mechanical behavior of SLM-built NiTi. Variability has long been an issue of concern for the AM industry, and reduction of the variability requires additional time and money costs due to post-processing. Despite this fact, there has been very few published works on this topic, and none in the field of SLM-manufactured NiTi. This is of especial concern with regards to NiTi, which is sensitive to variations in microstructure and composition.

First, we presented experimental results showing that under stress free conditions, two different categories of variability occurred in SLM-built NiTi. These were localized variability on the micron scale, and part-to-part variability. The relationship between process parameters and variability was investigated, and a critical link between hatch distance and variability was found.

Once it was experimentally validated and quantified that variability occurred in the specimens, a wide array of experiments was performed to determine which of the various mechanisms was responsible for the variation in transformation temperatures. The mechanisms investigated were composition, precipitation, dislocation density, residual stress, grain size, and texture. It was determined that two of these mechanisms were most likely to be responsible for variability.

Finally, a large number of mechanical tests were performed to determine if the variability in transformation temperatures also resulted in variability in mechanical properties.

The following summarizes the main findings with regards to observation of variability in the stress-free condition:

- Localized, micron scale variability was observed in a number of test specimens. This form of variability presented as broad transformation peaks during DSC experiments.
- Depending on the process parameters, samples could be printed that exhibited homogenous transformations with narrow peaks.
- The critical process parameter that controlled the appearance of broad or narrow peaks was the hatch distance. When the hatch distance was larger than 60μm, broad transformations occurred. When the hatch distance was smaller than 50μm, narrow transformations were the result.
- Part-to-part variability was observed, additionally, the parameter that controlled the localized variability also controlled part-to-part variability. Samples that were printed with a wide hatch distance exhibited poor repeatability, but samples printed with a narrow hatch distance showed very good repeatability with regards to the transformation temperatures.
- The reduction in part-to-part variability was effective regardless of the part geometry.
- When the variability was reduced by using a smaller hatch distance, it was found that the standard deviations of the transformation temperatures were comparable to industrial, conventionally processed NiTi products.

The following summarizes the main findings with regards to the microstructural and compositional investigation of the causes of variability:

- The existence of compositional gradients on the micron scale was observed in both the H35 and H120 specimens.
- Compositional gradients were unlikely to be responsible for the transformation temperature variability, due to the fact that the compositions were Ti rich, and the transformation temperatures shifted after low temperature heat treatments.
- In the H120 specimens which exhibited high variability, differences in precipitate size, volume fraction, and number density depending on the location relative to the melt pool were observed.
- In the H120 specimens, dislocation density also changed depending on the location.
- The grain size was found to be too large to have a significant effect on the transformation temperatures.

The following summarizes the main findings of the investigation of variability in the mechanical properties of SLM-built NiTi.

- For the H120 samples tested at 100°C and at RT the stress-strain curves showed clustering depending on the specimen group. This indicated that part-to-part variability also occurred in the mechanical properties.
- The coefficient of variation of the yield stress and of the elastic modulus of H120 were higher than for H35.
- The coefficients of variation of the H120 parts exceeded those of conventionally processed materials, while those of H35 were on par with conventional materials.
- Variability in the mechanical properties of SLM-built NiTi transformation temperatures under stress free conditions appeared under the same processing conditions that caused stress-free transformation temperature variability.

6.1 Future work

Based on the main findings in this work, the following recommendations for future research into SLM-built NiTi and variability in SLM parts can be made:

- Future experimental design for research into the shape memory behavior and mechanical properties of NiTi should include a sufficiently large sample size with replication to allow for statistical reporting of results to ensure that variability does not does not negatively affect the results.
- The work presented here focused mainly on the low laser power regime. Further studies should be performed using newer equipment with higher laser powers to determine how the extended process parameter space affects the variability.

- Small, <4nm precipitates were observed; however, it was not possible to quantify the variation of the distribution of these precipitates. Experiments using very high resolution TEM should be performed to determine the chemical composition and structure of these precipitates.
- Due to the high energy densities of the process parameters used in the current work the compositions of the materials were Ti rich and did not affect the transformation temperatures. Future studies using materials with higher Ni contents and parameters with smaller energy density should be done to see how the addition of compositional gradients affects variability.
- While experimental evidence showing location dependence of precipitate distribution, dislocation density, and composition was presented here, computational models exploring how these occur would be a welcome addition to understanding the variability.

REFERENCES

[1] T. Wohlers, T. Gornet. History of additive manufacturing, Wohlers report 24 (2014) 118.

[2] W. Sames, F. List, S. Pannala, R. Dehoff, S. Babu. The metallurgy and processing science of metal additive manufacturing, International Materials Reviews (2016) 1-46.

[3] H. Bikas, P. Stavropoulos, G. Chryssolouris. Additive manufacturing methods and modelling approaches: a critical review, The International Journal of Advanced Manufacturing Technology 83 (2015) 389-405.

[4] W.E. Frazier. Metal Additive Manufacturing: A Review, J Mater Eng Perform 23 (2014) 1917-1928.

[5] M. Seifi, A. Salem, J. Beuth, O. Harrysson, J.J. Lewandowski. Overview of materials qualification needs for metal additive manufacturing, Jom-Us 68 (2016) 747-764.

[6] R.W. Appleton. Additive manufacturing overview for the united states marine corps, RW Appleton and Company Inc, Sterling Heights, MI, Tech. Rep (2014).

[7] T.T. Wohlers, T. Caffrey. Wohlers Report 2015: 3D Printing and Additive Manufacturing State of the Industry Annual Worldwide Progress Report, Wohlers Associates, 2015.

[8] I. Tolosa, F. Garciandia, F. Zubiri, F. Zapirain, A. Esnaola. Study of mechanical properties of AISI 316 stainless steel processed by "selective laser melting", following different manufacturing strategies, Int J Adv Manuf Tech 51 (2010) 639-647.

[9] K. Kempen, B. Vrancken, S. Buls, L. Thijs, J. Van Humbeeck, J.P. Kruth. Selective Laser Melting of Crack-Free High Density M2 High Speed Steel Parts by Baseplate Preheating, Journal of Manufacturing Science and Engineering-Transactions of the Asme 136 (2014).

[10] W.E. Luecke, J.A. Slotwinski. Mechanical properties of austenitic stainless steel made by additive manufacturing, Journal of research of the National Institute of Standards and Technology 119 (2014) 398.

[11] C.U. Brown, G. Jacob, M. Stoudt, S. Moylan, J. Slotwinski, A. Donmez. Interlaboratory Study for Nickel Alloy 625 Made by Laser Powder Bed Fusion to Quantify Mechanical Property Variability, J Mater Eng Perform 25 (2016) 3390-3397.

[12] S. Li, Q.S. Wei, Y.S. Shi, Z.C. Zhu, D.Q. Zhang. Microstructure Characteristics of Inconel 625 Superalloy Manufactured by Selective Laser Melting, Journal of Materials Science & Technology 31 (2015) 946-952.

[13] J. Strossner, M. Terock, U. Glatzel. Mechanical and Microstructural Investigation of Nickel-Based Superalloy IN718 Manufactured by Selective Laser Melting (SLM), Adv Eng Mater 17 (2015) 1099-1105.

[14] Q.B. Jia, D.D. Gu. Selective laser melting additive manufactured Inconel 718 superalloy parts: High-temperature oxidation property and its mechanisms, Optics and Laser Technology 62 (2014) 161-171.

[15] S. Lenders, M. Thone, A. Riemer, T. Niendorf, T. Troster, H.A. Richard, H.J. Maier. On the mechanical behaviour of titanium alloy TiAl6V4 manufactured by selective laser melting: Fatigue resistance and crack growth performance, International Journal of Fatigue 48 (2013) 300-307.

[16] H. Rafi, N. Karthik, H. Gong, T.L. Starr, B.E. Stucker. Microstructures and mechanical properties of Ti6Al4V parts fabricated by selective laser melting and electron beam melting, J Mater Eng Perform 22 (2013) 3872-3883.

[17] T.-T. Ikeshoji, K. Nakamura, M. Yonehara, K. Imai, H. Kyogoku. Selective laser melting of pure copper, Jom-Us 70 (2018) 396-400.

[18] Z. Mao, D.Z. Zhang, P. Wei, K. Zhang. Manufacturing feasibility and forming properties of Cu-4Sn in selective laser melting, Materials 10 (2017) 333.

[19] A. Popovich, V. Sufiiarov, I. Polozov, E. Borisov, D. Masaylo, A. Orlov. Microstructure and mechanical properties of additive manufactured copper alloy, Materials Letters 179 (2016) 38-41.

[20] S. Dadbakhsh, L. Hao. Effect of Layer Thickness in Selective Laser Melting on Microstructure of Al/5wt.%Fe2O3 Powder Consolidated Parts, Sci World J (2014).

[21] L.E. Loh, C.K. Chua, W.Y. Yeong, J. Song, M. Mapar, S.L. Sing, Z.H. Liu, D.Q. Zhang. Numerical investigation and an effective modelling on the Selective Laser Melting (SLM) process with aluminium alloy 6061, Int J Heat Mass Tran 80 (2015) 288-300.

[22] E.O. Olakanmi. Selective laser sintering/melting (SLS/SLM) of pure Al, Al-Mg, and Al-Si powders: Effect of processing conditions and powder properties, Journal of Materials Processing Technology 213 (2013) 1387-1405.

[23] T. Bormann, R. Schumacher, B. Muller, M. Mertmann, M. de Wild. Tailoring Selective Laser Melting Process Parameters for NiTi Implants, J Mater Eng Perform 21 (2012) 2519-2524.

[24] M.T. Andani, C. Haberland, J. Walker, M. Elahinia. An Investigation of Effective Process Parameters on Phase Transformation Temperature of Nitinol Manufactured by Selective Laser Melting, (2014) V001T001A026.

[25] C. Haberland, M. Elahinia, J.M. Walker, H. Meier, J. Frenzel. On the development of high quality NiTi shape memory and pseudoelastic parts by additive manufacturing, Smart Mater Struct 23 (2014).

[26] J. Walker, M. Elahinia, C. Haberland, Asme. AN INVESTIGATION OF PROCESS PARAMETERS ON SELECTIVE LASER MELTING OF NITINOL, Amer Soc Mechanical Engineers, New York, 2014.

[27] H. Meier, C. Haberland, J. Frenzel. Structural and functional properties of NiTi shape memory alloys produced by Selective Laser Melting, Innovative Developments on Virtual and Physical Prototyping (2012) 291-296.

[28] C. Haberland, M. Elahinia, J. Walker, H. Meier, J. Frenzel. Additive Manufacturing of Shape Memory Devices and Pseudoelastic Components, (2013) V001T001A005.

[29] C. Haberland, H. Meier, J. Frenzel. On the Properties of Ni-Rich Niti Shape Memory Parts Produced by Selective Laser Melting, Proceedings of the Asme Conference on Smart Materials, Adaptive Structures and Intelligent Systems, Vol 1 (2013) 97-104.

[30] S. Dadbakhsh, M. Speirs, J.P. Kruth, J. Schrooten, J. Luyten, J. Van Humbeeck. Effect of SLM Parameters on Transformation Temperatures of Shape Memory Nickel Titanium Parts, Adv Eng Mater 16 (2014) 1140-1146.

[31] Z.X. Khoo, C. Ong, Y. Liu, C.K. Chua, K.F. Leong, S.F. Yang. Selective Laser Melting Of Nickel Titanium Shape Memory Alloy, (2016).

[32] S. Soheil, T. Ali Sadi, A. Mohsen Taheri, H. Christoph, E. Mohammad, K. Haluk. Thermomechanical characterization of Ni-rich NiTi fabricated by selective laser melting, Smart Mater Struct 25 (2016) 035005.

[33] M. Speirs, X. Wang, S. Van Baelen, A. Ahadi, S. Dadbakhsh, J.-P. Kruth, J. Van Humbeeck. On the Transformation Behavior of NiTi Shape-Memory Alloy Produced by SLM, Shape Memory and Superelasticity 2 (2016) 310-316.

[34] T. Bormann, B. Muller, M. Schinhammer, A. Kessler, P. Thalmann, M. de Wild. Microstructure of selective laser melted nickel-titanium, Materials Characterization 94 (2014) 189-202.

[35] B.A. Bimber, R.F. Hamilton, J. Keist, T.A. Palmer. Anisotropic microstructure and superelasticity of additive manufactured NiTi alloy bulk builds using laser directed energy deposition, Mat Sci Eng a-Struct 674 (2016) 125-134.

[36] S. Dadbakhsh, B. Vrancken, J.P. Kruth, J. Luyten, J. Van Humbeeck. Texture and anisotropy in selective laser melting of NiTi alloy, Materials Science and Engineering: A 650 (2016) 225-232.

[37] N. Shayesteh Moghaddam, S.E. Saghaian, A. Amerinatanzi, H. Ibrahim, P. Li, G.P. Toker, H.E. Karaca, M. Elahinia. Anisotropic tensile and actuation properties of NiTi fabricated with selective laser melting, Materials Science and Engineering: A 724 (2018) 220-230.

[38] S. Saedi, A.S. Turabi, M. Taheri Andani, C. Haberland, H. Karaca, M. Elahinia. The influence of heat treatment on the thermomechanical response of Ni-rich NiTi alloys manufactured by selective laser melting, J Alloy Compd 677 (2016) 204-210.

[39] M. Taheri Andani, S. Saedi, A.S. Turabi, M.R. Karamooz, C. Haberland, H.E. Karaca, M. Elahinia. Mechanical and shape memory properties of porous Ni50.1Ti49.9 alloys manufactured by selective laser melting, J Mech Behav Biomed 68 (2017) 224-231.

[40] J. Sam, B. Franco, J. Ma, I. Karaman, A. Elwany, J. Mabe. Tensile actuation response of additively manufactured nickel-titanium shape memory alloys, Scripta Mater 146 (2018) 164-168.

[41] S. Saedi, A.S. Turabi, M.T. Andani, N.S. Moghaddam, M. Elahinia, H.E. Karaca. Texture, aging, and superelasticity of selective laser melting fabricated Ni-rich NiTi alloys, Materials Science and Engineering: A 686 (2017) 1-10.

[42] D. Gu, W. Meiners, K. Wissenbach, R. Poprawe. Laser additive manufacturing of metallic components: materials, processes and mechanisms, International materials reviews 57 (2012) 133-164.

[43] J. Frenzel, E.P. George, A. Dlouhy, C. Somsen, M.F.X. Wagner, G. Eggeler. Influence of Ni on martensitic phase transformations in NiTi shape memory alloys, Acta Materialia 58 (2010) 3444-3458.

[44] E.Y. Panchenko, Y.I. Chumlyakov, I.V. Kireeva, A.V. Ovsyannikov, H. Sehitoglu, I. Karaman, Y.H.J. Maier. Effect of disperse Ti3N4 particles on the martensitic transformations in titanium nickelide single crystals, Phys Met Metallogr+ 106 (2008) 577-589.

[45] E. Hornbogen. The Effect of Variables on Martensitic-Transformation Temperatures, Acta Metall Mater 33 (1985) 595-601.

[46] K. Gall, H. Sehitoglu, Y.I. Chumlyakov, I.V. Kireeva, H.J. Maier. The influence of aging on critical transformation stress levels and martensite start temperatures in NiTi: Part II - Discussion of experimental results, Journal of Engineering Materials and Technology-Transactions of the Asme 121 (1999) 28-37.

[47] D.A. Miller, D.C. Lagoudas. Influence of cold work and heat treatment on the shape memory effect and plastic strain development of NiTi, Materials Science and Engineering: A 308 (2001) 161-175.

[48] P. La Roca, L. Isola, P. Vermaut, J. Malarría. Relationship between grain size and thermal hysteresis of martensitic transformations in Cu-based shape memory alloys, Scripta Mater 135 (2017) 5-9.

[49] S. Gao, S. Yi. Experimental study on the anisotropic behavior of textured NiTi pseudoelastic shape memory alloys, Materials Science and Engineering: A 362 (2003) 107-111.

[50] S.A. Tofail, E.P. Koumoulos, A. Bandyopadhyay, S. Bose, L. O'Donoghue, C. Charitidis. Additive manufacturing: Scientific and technological challenges, market uptake and opportunities, Mater Today 21 (2018) 22-37.

[51] T. Caffrey, I. Campbell, T. Wohlers. REPORT: ADDITIVE MANUFACTURING INDUSTRY SURPASSED $5.1 BILLION, Appliance Design 64 (2016) 6-6.

[52] D. Thomas. Costs, benefits, and adoption of additive manufacturing: a supply chain perspective, The International Journal of Advanced Manufacturing Technology 85 (2016) 1857-1876.

[53] M. Speirs, B. Van Hooreweder, J. Van Humbeeck, J.P. Kruth. Fatigue behaviour of NiTi shape memory alloy scaffolds produced by SLM, a unit cell design comparison, J Mech Behav Biomed 70 (2017) 53-59.

[54] D. Hartl, J. Mingear, B. Bielefeldt, J. Rohmer, J. Zamarripa, A. Elwany. Towards High-Frequency Shape Memory Alloy Actuators Incorporating Liquid Metal Energy Circuits, Shape Memory and Superelasticity 3 (2017) 457-466.

[55] W. Hoffmann, T. Bormann, A. Rossi, B. Muller, R. Schumacher, I. Martin, M. de Wild, D. Wendt. Rapid prototyped porous nickel-titanium scaffolds as bone substitutes, Journal of tissue engineering 5 (2014) 2041731414540674.

[56] T. Bormann, M. de Wild, F. Beckmann, B. Muller. Assessing the morphology of selective laser melted NiTi-scaffolds for a three-dimensional quantification of the one-way shape memory effect, Behavior and Mechanics of Multifunctional Materials and Composites 2013 8689 (2013).

[57] T. Niendorf, F. Brenne, M. Schaper, A. Riemer, S. Leuders, W. Reimche, D. Schwarze, H.J. Maier, R.I. Campbell, R.I. Campbell. Labelling additively manufactured parts by microstructural gradation–advanced copy-proof design, Rapid Prototyping Journal 22 (2016).

[58] B. Franco, J. Ma, B. Loveall, G. Tapia, K. Karayagiz, J. Liu, A. Elwany, R. Arroyave, I. Karaman. A sensory material approach for reducing variability in additively manufactured metal parts, Scientific Reports 7 (2017) 3604.

[59] J. Ma, B. Franco, G. Tapia, K. Karayagiz, L. Johnson, J. Liu, R. Arroyave, I. Karaman, A. Elwany. Spatial control of functional response in 4D-printed active metallic structures, Scientific reports 7 (2017) 46707.

[60] S. Tibbits. 4D PRINTING: MULTI-MATERIAL SHAPE CHANGE, Archit. Des. 84 (2014) 116-121.

[61] D.S. Thomas. Economics of Additive Manufacturing. Laser-Based Additive Manufacturing of Metal Parts. CRC Press, 2017. pp. 299-334.

[62] R. Shah, P.T. Ward. Lean manufacturing: context, practice bundles, and performance, Journal of operations management 21 (2003) 129-149.

[63] J. Allen. An investigation into the comparative costs of additive manufacture vs. machine from solid for aero engine parts. DTIC Document, 2006.

[64] E. Kaya, İ. Kaya. A review on machining of NiTi shape memory alloys: The process and post process perspective, The International Journal of Advanced Manufacturing Technology 100 (2019) 2045-2087.

[65] F. Sczerzenie. Consideration of the ASTM Standards for Ni-Ti Alloys, (2004).

[66] L. Parry, I. Ashcroft, R.D. Wildman. Understanding the effect of laser scan strategy on residual stress in selective laser melting through thermo-mechanical simulation, Additive Manufacturing 12 (2016) 1-15.

[67] M.J. Xia, D.D. Gu, G.Q. Yu, D.H. Dai, H.Y. Chen, Q.M. Shi. Influence of hatch spacing on heat and mass transfer, thermodynamics and laser processability during additive manufacturing of Inconel 718 alloy, Int J Mach Tool Manu 109 (2016) 147-157.

[68] K. Zeng, D. Pal, B. Stucker. A review of thermal analysis methods in Laser Sintering and Selective Laser Melting. Proceedings of the Solid Freeform Fabrication Symposium, Austin, TX, 2012. p.796-814.

[69] K. Karayagiz, A. Elwany, G. Tapia, B. Franco, L. Johnson, J. Ma, I. Karaman, R. Arroyave. Numerical and experimental analysis of heat distribution in the laser powder bed fusion of Ti-6Al-4V, IISE Transactions (2018) 1-17.

[70] F. Verhaeghe, T. Craeghs, J. Heulens, L. Pandelaers. A pragmatic model for selective laser melting with evaporation, Acta Materialia 57 (2009) 6006-6012.

[71] A. Klassen, T. Scharowsky, C. Korner. Evaporation model for beam based additive manufacturing using free surface lattice Boltzmann methods, J Phys D Appl Phys 47 (2014) 12.

[72] I. Yadroitsev, A. Gusarov, I. Yadroitsava, I. Smurov. Single track formation in selective laser melting of metal powders, Journal of Materials Processing Technology 210 (2010) 1624-1631.

[73] X. Su, Y. Yang. Research on track overlapping during selective laser melting of powders, Journal of Materials Processing Technology 212 (2012) 2074-2079.

[74] J.-P. Kruth, X. Wang, T. Laoui, L. Froyen. Lasers and materials in selective laser sintering, Assembly Autom 23 (2003) 357-371.

[75] L.M. Sochalski-Kolbus, E.A. Payzant, P.A. Cornwell, T.R. Watkins, S.S. Babu, R.R. Dehoff, M. Lorenz, O. Ovchinnikova, C. Duty. Comparison of Residual Stresses in Inconel 718

Simple Parts Made by Electron Beam Melting and Direct Laser Metal Sintering, Metallurgical and Materials Transactions a-Physical Metallurgy and Materials Science 46A (2015) 1419-1432.

[76] P. Mercelis, J.P. Kruth. Residual stresses in selective laser sintering and selective laser melting, Rapid Prototyping Journal 12 (2006) 254-265.

[77] J.P. Kruth, J. Deckers, E. Yasa, R. Wauthle. Assessing and comparing influencing factors of residual stresses in selective laser melting using a novel analysis method, Proceedings of the Institution of Mechanical Engineers Part B-Journal of Engineering Manufacture 226 (2012) 980-991.

[78] Z.H. Liu, C.K. Chua, K.F. Leong, K. Kempen, L. Thijs, E. Yasa, J. Van-Humbeeck, J.P. Kruth. A preliminary investigation on Selective Laser Melting of M2 high speed steel, Crc Press-Taylor & Francis Group, Boca Raton, 2012.

[79] D. Buchbinder, W. Meiners, N. Pirch, K. Wissenbach, J. Schrage. Investigation on reducing distortion by preheating during manufacture of aluminum components using selective laser melting, Journal of Laser Applications 26 (2014) 10.

[80] S. Marimuthu, D. Clark, J. Allen, A.M. Kamara, P. Mativenga, L. Li, R. Scudamore. Finite element modelling of substrate thermal distortion in direct laser additive manufacture of an aero-engine component, Proceedings of the Institution of Mechanical Engineers Part C-Journal of Mechanical Engineering Science 227 (2013) 1987-1999.

[81] E.R. Denlinger, J.C. Heigel, P. Michaleris, T.A. Palmer. Effect of inter-layer dwell time on distortion and residual stress in additive manufacturing of titanium and nickel alloys, Journal of Materials Processing Technology 215 (2015) 123-131.

[82] A. Riemer, S. Leuders, M. Thone, H.A. Richard, T. Troster, T. Niendorf. On the fatigue crack growth behavior in 316L stainless steel manufactured by selective laser melting, Engineering Fracture Mechanics 120 (2014) 15-25.

[83] P. Edwards, M. Ramulu. Fatigue performance evaluation of selective laser melted Ti-6Al-4V, Mat Sci Eng a-Struct 598 (2014) 327-337.

[84] W.E. King, H.D. Barth, V.M. Castillo, G.F. Gallegos, J.W. Gibbs, D.E. Hahn, C. Kamath, A.M. Rubenchik. Observation of keyhole-mode laser melting in laser powder-bed fusion additive manufacturing, Journal of Materials Processing Technology 214 (2014) 2915-2925.

[85] T. Vilaro, C. Colin, J.D. Bartout. As-Fabricated and Heat-Treated Microstructures of the Ti-6Al-4V Alloy Processed by Selective Laser Melting, Metallurgical and Materials Transactions a-Physical Metallurgy and Materials Science 42A (2011) 3190-3199.

[86] C.L. Qiu, C. Panwisawas, M. Ward, H.C. Basoalto, J.W. Brooks, M.M. Attallah. On the role of melt flow into the surface structure and porosity development during selective laser melting, Acta Materialia 96 (2015) 72-79.

[87] K. Bhattacharya. Microstructure of martensite: why it forms and how it gives rise to the shape-memory effect, Oxford University Press, 2003.

[88] D.C. Lagoudas. Shape memory alloys: modeling and engineering applications, Springer, 2008.

[89] H. Funakubo, J. Kennedy. Shape memory alloys, Gordon and Breach, xii+ 275, 15 x 22 cm, Illustrated (1987).

[90] K. Otsuka, X. Ren. Physical metallurgy of Ti-Ni-based shape memory alloys, Progress in Materials Science 50 (2005) 511-678.

[91] J. Ortin, A. Planes. Thermodynamic Analysis of Thermal Measurements in Thermoelastic Martensitic Transformations .68. Overview, Acta Metall Mater 36 (1988) 1873-1889.

[92] B.E. Franco. Engineering the martensitic transformation hysteresis of Ni-rich NiTi alloys. 2014.

[93] P.R. Chalker, A. Clare, S. Davies, C.J. Sutcliffe, S. Tsopanos. Selective laser melting of high aspect ratio 3D nickel-titanium structures for MEMS applications. in: Bull SJ, Chalker PR, Chen SC, Meng WJ, Maboudian R, (Eds.). Surface Engineering for Manufacturing Applications, vol. 890. Materials Research Society, Warrendale, 2006. pp. 93-98.

[94] A.T. Clare, P.R. Chalker, S. Davies, C.J. Sutcliffe, S. Tsopanos. Selective laser melting of high aspect ratio 3D nickel–titanium structures two way trained for MEMS applications, International Journal of Mechanics and Materials in Design 4 (2008) 181-187.

[95] T. Bormann, R. Schumacher, B. Mueller, M. de Wild. Controlling Mechanical Properties of NiTi Scaffolds built by Selective Laser Melting, Biomedical Engineering-Biomedizinische Technik 57 (2012).

[96] G. Yablokova, M. Speirs, J. Van Humbeeck, J.P. Kruth, J. Schrooten, R. Cloots, F. Boschini, G. Lumay, J. Luyten. Rheological behavior of beta-Ti and NiTi powders produced by atomization for SLM production of open porous orthopedic implants, Powder Technol 283 (2015) 199-209.

[97] I.V. Shishkovsky, I.A. Yadroitsev, I.Y. Smurov. Selective Laser Sintering/Melting of Nitinol-Hydroxyapatite Composite for Medical Applications, Powder Metall Met C+ 50 (2011) 275-283.

[98] I.V. Shishkovsky, I.A. Yadroitsev, I.Y. Smurov. Manufacturing three-dimensional nickel titanium articles using layer-by-layer laser-melting technology, Tech Phys Lett+ 39 (2013) 1081-1084.

[99] M. de Wild, F. Meier, T. Bormann, C.B.C. Howald, B. Muller. Damping of Selective-Laser-Melted NiTi for Medical Implants, J Mater Eng Perform 23 (2014) 2614-2619.

[100] T. Habijan, C. Haberland, H. Meier, J. Frenzel, J. Wittsiepe, C. Wuwer, C. Greulich, T.A. Schildhauer, M. Koller. The biocompatibility of dense and porous Nickel-Titanium produced by selective laser melting, Mat Sci Eng C-Mater 33 (2013) 419-426.

[101] C. Haberland, M. Elahinia, J. Walker, H. Meier. Visions, concepts and strategies for smart Nitinol actuators and complex Nitinol structures produced by Additive Manufacturing. ASME 2013 Conference on Smart Materials, Adaptive Structures and Intelligent Systems: American Society of Mechanical Engineers, 2013. p.V001T001A006-V001T001A006.

[102] H. Meier, C. Haberland, J. Frenzel, R. Zarnetta. Selective Laser Melting of NiTi shape memory components, Innovative Developments in Design and Manufacturing (2010) 233-238.

[103] I. Shishkovsky, V. Sherbakoff, I. Yadroitsev, I. Smurov. Peculiar features of electrical resistivity and phase structure in 3-D porous nitinol after selective laser sintering/melting process, Proceedings of the Institution of Mechanical Engineers Part C-Journal of Mechanical Engineering Science 226 (2012) 2982-2989.

[104] J.M. Walker, C. Haberland, M.T. Andani, H.E. Karaca, D. Dean, M. Elahinia. Process development and characterization of additively manufactured nickel-titanium shape memory parts, J. Intell. Mater. Syst. Struct. 27 (2016) 2653-2660.

[105] D. Gu, C. Ma. In-situ formation of Ni4Ti3 precipitate and its effect on pseudoelasticity in selective laser melting additive manufactured NiTi-based composites, Appl Surf Sci 441 (2018) 862-870.

[106] S. Saedi, N.S. Moghaddam, A. Amerinatanzi, M. Elahinia, H.E. Karaca. On the effects of selective laser melting process parameters on microstructure and thermomechanical response of Ni-rich NiTi, Acta Materialia 144 (2018) 552-560.

[107] C. Haberland, M. Elahinia, J. Walker, H. Meier, J. Frenzel, Asme. ADDITIVE MANUFACTURING OF SHAPE MEMORY DEVICES AND PSEUDOELASTIC COMPONENTS, Amer Soc Mechanical Engineers, New York, 2014.

[108] N.S. Moghaddam, S. Saedi, A. Amerinatanzi, A. Hinojos, A. Ramazani, J. Kundin, M.J. Mills, H. Karaca, M. Elahinia. Achieving superelasticity in additively manufactured NiTi in compression without post-process heat treatment, Scientific reports 9 (2019) 41.

[109] N.S. Moghaddam, S.E. Saghaian, A. Amerinatanzi, H. Ibrahim, P. Li, G.P. Toker, H.E. Karaca, M. Elahinia. Anisotropic tensile and actuation properties of NiTi fabricated with selective laser melting, Materials Science and Engineering: A 724 (2018) 220-230.

[110] N. Gupta, C. Weber, S. Newsome. Additive Manufacturing: Status and Opportunities, Science and Technology Policy Institute, Washington (2012).

[111] S.S. Al-Bermani, M.L. Blackmore, W. Zhang, I. Todd. The Origin of Microstructural Diversity, Texture, and Mechanical Properties in Electron Beam Melted Ti-6Al-4V,

Metallurgical and Materials Transactions a-Physical Metallurgy and Materials Science 41A (2010) 3422-3434.

[112] M. Mahmoudi, G. Tapia, B. Franco, J. Ma, R. Arroyave, I. Karaman, A. Elwany. On the printability and transformation behavior of nickel-titanium shape memory alloys fabricated using laser powder-bed fusion additive manufacturing, Journal of Manufacturing Processes 35 (2018) 672-680.

[113] R.F. Hamilton, T.A. Palmer, B.A. Bimber. Spatial characterization of the thermal-induced phase transformation throughout as-deposited additive manufactured NiTi bulk builds, Scripta Mater 101 (2015) 56-59.

[114] Y. Shu, K. Bhattacharya. The influence of texture on the shape-memory effect in polycrystals, Acta Materialia 46 (1998) 5457-5473.

[115] P. Thamburaja, L. Anand. Polycrystalline shape-memory materials: effect of crystallographic texture, Journal of the Mechanics and Physics of Solids 49 (2001) 709-737.

[116] K. Otsuka, C.M. Wayman. Shape memory materials, Cambridge university press, 1999.

[117] T. Gnaupel-Herold, J. Slotwinski, S. Moylan. Neutron Measurements of Stresses in a Test Artifact Produced by Laser-based Additive Manufacturing. in: Chimenti DE, Bond LJ, Thompson DO, (Eds.). 40th Annual Review of Progress in Quantitative Nondestructive Evaluation: Incorporating the 10th International Conference on Barkhausen Noise and Micromagnetic Testing, Vols 33a & 33b, vol. 1581. Amer Inst Physics, Melville, 2014. pp. 1205-1212.

[118] Y. Ogasawara, T.S. Hadi, M. Maeda. Rates of evaporation in a vacuum in liquid Ni–Ti alloys, ISIJ international 38 (1998) 789-793.

[119] J.P. Oliveira, A.J. Cavaleiro, N. Schell, A. Stark, R.M. Miranda, J.L. Ocana, F.M. Braz Fernandes. Effects of laser processing on the transformation characteristics of NiTi: A contribute to additive manufacturing, Scripta Mater 152 (2018) 122-126.

[120] L. Johnson, K. Karayagiz, B. Franco, J. Ma, I. Karaman, A. Elwany, R. Arroyave. Predicting spatial variations of precipitates from a finite element thermal model, Manuscript submitted for publication (2018).

[121] J. Bernardini, C. Lexcellent, L. Daróczi, D. Beke. Ni diffusion in near-equiatomic Ni-Ti and Ni-Ti (-Cu) alloys, Philosophical Magazine 83 (2003) 329-338.